Angle-resolved photoemission and density functional theory studies of topological materials

by

Zhi-Huai Zhu

B.Sc., Nanjing University, 2007
M.Sc., The University of British Columbia, 2009

A THESIS SUBMITTED IN PARTIAL FULFILLMENT OF
THE REQUIREMENTS FOR THE DEGREE OF

DOCTOR OF PHILOSOPHY

in

The Faculty of Graduate and Postdoctoral Studies

(Physics)

THE UNIVERSITY OF BRITISH COLUMBIA

(Vancouver)

Septermber, 2013

Abstract

Topological insulators (TIs), with a gapless surface state located in a large bulk band gap, define a new class of materials with strong application potential in quantum electronic devices. However, real TI materials have many critical problems, such as bulk conductivity and surface instability, which hinder us from utilizing their exotic topological states. Another fundamental question in the TI field is what the realistic spin texture of the topological surface states (TSSs) is; no conclusive answer has yet been reached, despite extensive studies.

We present two studies of doping the prototypical TI materials via in situ potassium deposition at the surface of Bi_2Se_3 and by adding magnetic impurities into the bulk Bi_2Te_3 during crystal growth. We show that potassium deposition can overcome the instability of the surface electronic properties. In addition to accurately setting the carrier concentration, new Rashba-like spin-polarized states are induced, with tunable, reversible, and highly stable spin splitting. Our density functional theory (DFT) calculations reveal that these Rashba states are derived from quantum well states associated with a K-induced 5 nm confinement potential. The Mn impurities in Bi_2Te_3 have a dramatic effect on tailoring the spin-orbit coupling of the system, manifested by decreasing the size of the bulk band gap even at low concentrations (2%-5%). This result suggests an efficient way to induce a quantum phase transition from TIs to trivial insulators.

We also explicitly unveil the TSS spin texture in TI materials. By a combination of polarization-dependent angle-resolved photoemission spectroscopy (ARPES) and DFT slab calculations, we find that the surface states are characterized by a layer-dependent entangled spin-orbital texture, which becomes apparent through quantum interference effects. We predict a way

to probe the intrinsic spin texture of TSS, and to continuously manipulate the spin polarization of photoelectrons all the way from 0 to ±100% by an appropriate choice of photon energy and linear polarization. Our spin-resolved ARPES experiment confirms these predictions and establishes a generic rule for the manipulation of photoelectron spin polarization. This work paves a new pathway towards the long-term goal of utilizing TIs for opto-spintronics.

Preface

The work described in this thesis was conducted over the past four years during my Ph.D. program at the University of British Columbia (UBC). I did not include all the work that I have accomplished, selecting only the topological insulator related portions. A full list of my publications is provided in the Appendix, including my other work contributed to group publications. All the work presented here has been or will be published with me as the first author. This is not to say that I produced this work alone; details of my contributions are below.

Chapter 3 – Ab initio tight-binding model

This chapter is the supplementary work for Chapter 5. Under the direction of I. S. Elfimov and M. W. Haverkort, I developed the ab initio tight-binding (TB) model for Bi_2Se_3. M. W. Haverkort provided me with several Mathematica packages that are particularly useful for figure plotting, which also helped me learn how to program in Mathematica. I wrote all the source codes for the TB model calculations and produced all relevant data.

Chapter 4, Section 4.1 – Rashba spin-splitting control at the surface of Bi_2Se_3

This work has been published in *Physical Review Letters* 107, 186405 (2011) [1]. I performed the experiments by using the in-house angle-resolved photoemission spectroscopy (ARPES) system at UBC, a system I have played a role in helping to maintain and characterize over the past five years. All the data presented in this chapter was physically taken by myself, with help from other ARPES group members, in particular G. Levy and B. Ludbrook.

The Bi_2Se_3 samples were grown by P. Syers, N. P. Butch and J. Paglione at the University of Maryland, and A. Ubaldini at the University of Geneva. I also performed all the data analysis and wrote the manuscript. My supervisor, A. Damascelli, guided me regarding the direction of the work and edited the final version of the manuscript. A. Damascelli, I. S. Elfimov, and I contributed theoretical ideas to explain the ARPES data. I performed the density functional theory (DFT) calculations together with I. S. Elfimov.

Chapter 4, Section 4.2 – Tailoring spin-orbit coupling in Mn-doped $Bi_{2-x}Mn_xTe_3$

The work in this chapter has not been published yet. I performed the ARPES experiments at UBC with assistance from Ivana Vobornik, a beamline scientist at ELETTRA who also brought the samples to me for ARPES measurements. The samples were origionally grown by R. Cava's group at Princeton University. I performed all the data analysis and wrote the manuscript. A. Damascelli supervised the development of my scientific ideas for this work.

Chapter 5 – Layer-by-layer entangled spin-orbital texture in Bi_2Se_3

This chapter has been published in *Physical Review Letters* 110, 216401 (2013) [2]. I performed ARPES experiments with assistance from G. Levy. The single crystals were grown by P. Syers, N. P. Butch, J. Paglione and A. Ubaldini. I performed the theoretical calculations and data analysis, under the supervision of M. W. Haverkort and I. S. Elfimov. A. Damascelli supervised the overall project direction and planning. C. N. Veenstra helped me in writing the code; he was also very helpful on editing my manuscript. I wrote the manuscript together with M. W. Haverkort and A. Damascelli.

Chapter 6 – Photoelectron spin polarization control in Bi_2Se_3

This chapter has been submitted for publication. The spin-resolved ARPES data was taken at Hiroshima Synchrotron Radiation Center by the group of

C.N. Veenstra, S. Zhdanovich, and I. I designed the experiments and led the data acquisition during the beamtime. C. N. Veenstra was extremely helpful for discussions and planning. Together with S. Zhdanovich, he also prepared the high-quality samples for this experiment. T. Okuda and K. Miyamoto, two beamline scientists, also constantly provided assistance with instrument operations and experiment planning. I performed the data analysis and wrote the manuscript together with A. Damascelli. A. Damascelli supervised the overall project direction and planning.

Table of Contents

List of Figures

List of Abbreviations

2D two-dimensional

3D three-dimensional

ARPES angle-resolved photoemission spectroscopy

a.u. arbitrary units

BZ Brillouin zone

CEC constant energy contour

DC Dirac cone

DFT density functional theory

DP Dirac point

EDC energy distribution curve

ESPRESSO Efficient SPin REsolved Spectroscopy

FS Fermi surface

FWHM full width at half maximum

LMTO linear muffin-tin orbital

MDC momentum distribution curve

NMTO order-N muffin-tin orbital

QL quintuple layer

QW quantum well

RB Rashba band

SARPES spin- and angle-resolved photoemission spectroscopy

SOC spin-orbit coupling

SPECS SPECS Surface Nano Analysis GmbH

STM scanning tunneling microscope

TB tight-binding

TI topological insulator

TRS time-reversal symmetry

TSS topological surface state

UBC University of British Columbia

List of Symbols

Γ the origin in momentum space of the bulk Brillouin zone.

$\bar{\Gamma}$ the origin in momentum space of the surface Brillouin zone.

I photoemission intensity

λ strength of atomic spin-orbit coupling

$\mathbf{k}$ electron momentum

$\mathbf{k}_{||}$ electron momentum parallel to the sample surface

k_x electron momentum projected along $\hat{x}$

k_y electron momentum projected along $\hat{y}$

k_z electron momentum projected along $\hat{z}$

M matrix element

p_x atomic p_x orbital

p_y atomic p_y orbital

p_z atomic p_z orbital

P_x spin polarization of photoelectrons along the x quantization axis

P_y spin polarization of photoelectrons along the y quantization axis

P_z spin polarization of photoelectrons along the z quantization axis

Ψ_{TSS} wave function of topological surface state

$\boldsymbol{\sigma}$ Pauli spin matrices

τ index of the basis set of atomic orbitals

Acknowledgements

I would not have been able to accomplish the work presented in this thesis without the help of many people. First and foremost, I would like to thank my advisor, Prof. Andrea Damascelli, for his mentorship and consistent support. Andrea has provided me with strict scientific training that will guide me through all future work. He also gave me endless encouragement and professional advice for my graduate career. Working with Andrea enabled me to believe that I could always find the best resources to solve problems, either provided directly by him or through new opportunities that he created for me to work with other experts.

I would like to give a special thank you to Dr. Ilya Elfimov, who taught me how to do theoretical calculations. As a theoretical supervisor, Ilya has consistently supported and actively contributed to all my work. I appreciated how Ilya always gave me priority to use clusters for super-large calculations, and his tremendous effort in providing me with computational resources. I would definitely like to continue collaborating with him in my future academic work.

I also received great support from all my lab mates: Dr. Giorgio Levy, Christian Veenstra, Bart Ludbrook, Riccardo Comin, Sergey Zhdanovich, Ryan Wicks, Jonathan Rosen, and Michael Schneider. Thank you all. I would like to underscore my thanks to Giorgio again; when I first arrived at UBC, he taught me the XAS, XPS, and ARPES techniques, and has given me consistent support in my ARPES experiments. I also would like to especially thank Christian, who helped me with professional English editing and also gave me great advice on programming. I was happy to conduct two successful SARPES beamtime work with him, and his precise working style was very helpful.

Discussion with Prof. George Sawatzky was always a valuable opportunity for me to learn new physics. The richness of his knowledge in physics always inspired new ideas for my research projects. It has been a wonderful experience to have George involved in most of my scientific discussions. I would really like to thank him for all his time and ideas.

I have enjoyed working with Dr. Maurits Haverkort, and would like to thank him for leading me into the field of tight-binding related models. His expertise in theoretical modeling and insights into fundamental physical problems always greatly inspired me. I look forward to more collaborations with him.

Prof. Marcel Franz helped me with understanding the fundamental physics of topological insulators, the central topic of this thesis. I learned a lot during our discussions. I would like to thank Marcel for his patience in answering my questions, even when I brought up underdeveloped ideas.

I would like to thank all my sample providers: Paul Syers, Dr. Nicholas Butch, Prof. Johnpierre Paglione at the University of Maryland, and Albert Ubaldini at the University of Geneva. I also would like to thank Ivana Vobornik and Giancarlo Panaccione at ELETTRA for collaborating with me on the Mn-doped topological insulators project.

I would like to thank Prof. Taichi Okuda for his warmest hospitality and all his help during my spin-resolved ARPES beamtime in Japan. I thank Dr. K. Miyamoto and Siyuan Zhu for their help as well.

Finally, I would like to thank my fiancée, Vicky Li. She has been a tremendous support throughout my entire Ph.D. career. She has endured the grueling aspects of my physics life and always gave me her support whenever things did not seem to be progressing as expected. She was also the first person to read all my drafts and helped me with the first round of editing.

Chapter 1

Introduction

In atomic physics, electrons always move in an environment with an electric field $-e\boldsymbol{E} = -\boldsymbol{\nabla}V$, due to the strong Coulomb potential of the atomic core regions. Classically, the magnetic moment of electrons μ_s does not couple to the electric field. However, taking into account relativistic effects, the electron sees in its rest frame a magnetic field, whose value is given by $\boldsymbol{B} = -\boldsymbol{v} \times \boldsymbol{E}/c\ (v/c)^2$, with v being the velocity of the electron and c the speed of light [3]. The interaction of the magnetic moment μ_s with this magnetic field leads to a potential energy term, called spin-orbit coupling (SOC). A more rigorous, albeit less physically transparent, derivation of the SOC term can be obtained from the Pauli equation by taking the nonrelativistic approximation of the Dirac equation [4]. This approach gives rise to the Pauli SOC term:

$$H_{\mathrm{SOC}} = -\frac{\hbar}{4m_0^2c^2}\boldsymbol{\sigma} \cdot \boldsymbol{p} \times (\nabla V), \tag{1.1}$$

where $\hbar$ is Planck's constant, m_0 is the mass of a free electron, c is the velocity of light, $\boldsymbol{p}$ is the momentum operator, V is the Coulomb potential of the atomic core, and $\boldsymbol{\sigma} = (\sigma_x, \sigma_y, \sigma_z)$ is the vector of Pauli spin matrices. It is clear that the strength of SOC depends on the potential gradient near the core of atoms, therefore heavier elements usually have stronger SOC.

SOC makes the spin degree of freedom respond to its orbital environment. In solids this yields such intriguing phenomena as a spin splitting of electron states in inversion-asymmetric systems even at zero magnetic field [5, 6], a Zeeman splitting that is significantly enhanced in magnitude over that for free electrons, and the newly discovered topological insulator (TI) [7, 8]. This exotic physics has led SOC to become central to many inter-

esting and technologically important phenomena, including ferromagnetism, spintronics, non-centrosymmetric superconductivity, and the quantum Hall effect.

1.1 SOC in systems with inversion symmetry

In systems with space inversion and time-reversal symmetry (TRS), the space inversion symmetry gives rise to the same energy state at two opposite momenta for both spin up and spin down: $E_{+/-}(\mathbf{k}) = E_{+/-}(-\mathbf{k})$; but TRS flips the spin and results in a Kramers degeneracy: $E_{+}(\mathbf{k}) = E_{-}(-\mathbf{k})$. The consequence of the combined effect of inversion symmetry in space and time is the spin degeneracy: $E_{+}(\mathbf{k}) = E_{-}(\mathbf{k})$. Although SOC will not induce spin-polarized states in systems with inversion symmetry, it can change the orbital and spin characteristics of the electronic states, which are generally described by energy band structures. For example, in a tight-binding picture without spin, these electron states can be characterized by atomic orbitals, such as p-like states with orbital angular momentum $l = 1$. With SOC taken into account, electronic states become mixed and will be characterized by the total angular momentum $j = 3/2$ and $j = 1/2$. The energy splitting of $j = 3/2$ and $j = 1/2$ states results in a gap equal to the strength of SOC and consequently lifts the hybridization degeneracy existing at the band edges.

It has been reported that the interplay between SOC and details of the band structure close to the Fermi energy is essential for understanding the microscopic physics in transition-metal oxides, such as the mott-insulator Sr_2IrO_4 [9, 10], the p-wave superconductor Sr_2RuO_4 [11], and the paramagnetic Fermi liquid Sr_2RhO_4 [11, 12]. Here we take Sr_2RuO_4 as an example to show the importance of the SOC effect in a system with inversion symmetry [13, 14], which is the work in which I have been involved and to which I have contributed, although details are not shown in the main body of this thesis.[1]

In Sr_2RuO_4, the calculated effective SOC is comparatively small ($\zeta_{eff} \sim 90\,\mathrm{meV}$ at the Γ point) with respect to the bandwidth ($\sim 3\,\mathrm{eV}$) of the Ru-t_{2g}

[1] Details of the experimental results and calculation methods can been found in Ref. [13].

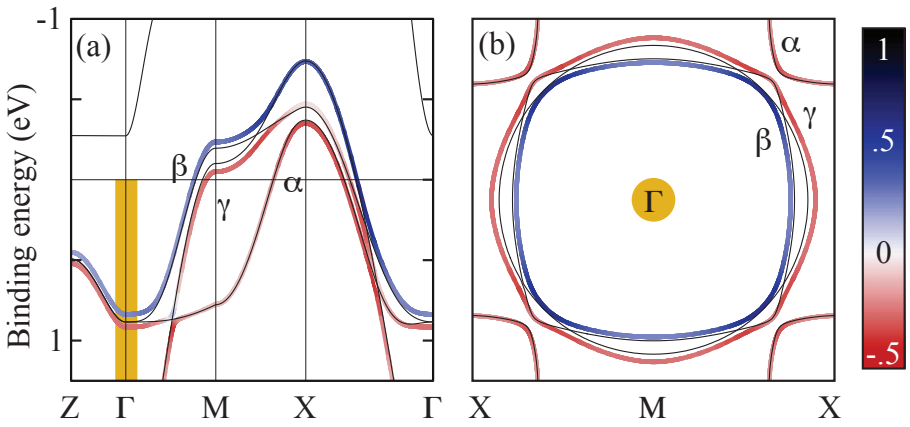

Figure 1.1: Effect of SOC on the band dispersion and Fermi surface of Sr_2RuO_4. (a) Band structure along the high-symmetry directions. (b) $k_z = 0$ Fermi surface, calculated both without (thin black) and with (thick, color-coded to show $\langle \boldsymbol{l} \cdot \boldsymbol{s} \rangle$) the inclusion of SOC. At the Γ point, the latter gives rise to a $\zeta_{eff} \sim 90\,\text{meV}$ splitting.

orbitals, which define the α, β and γ conduction bands. Nevertheless, its influence always becomes important whenever bands would be degenerate in the absence of SOC, either by symmetry or accidentally. This happens in the three-dimensional Brillouin zone (BZ), as demonstrated in Fig. 1.1, where we show a comparison of the ab initio tight-binding band structure and Fermi surface calculated with (color) and without (black) SOC included. In the absence of SOC, by symmetry the d_{xz} and d_{yz} bands would be degenerate along the entire k_z momentum path from Γ to Z. Additionally, there are accidental degeneracies along the $k_z = 0$ path from Γ to X, where the bands of $d_{xz,yz}$ and d_{xy} character all cross each other. At all these locations SOC naturally leads to a splitting and mixing of orbital character from all three bands.

The predicted importance of SOC can be directly visualized via the expectation value of $\boldsymbol{l} \cdot \boldsymbol{s}$, with $\boldsymbol{l}$ and $\boldsymbol{s}$ being the orbital and spin angular momentum operators. A non-zero value of $\langle \boldsymbol{l} \cdot \boldsymbol{s} \rangle$ indicates complex orbital eigenstates that can be entangled with the spin, seen in Fig. 1.1. Using

circularly polarized light-combined spin- and angle-resolved photoemission spectroscopy, we directly measured the value of the effective SOC to be 130±30 meV. This was even larger than theoretically predicted and comparable to the energy splitting of the d_{xy} and $d_{xz,yz}$ orbitals around the Fermi surface, resulting in a strongly momentum-dependent entanglement of spin and orbital character.

The consequence of a strong spin-orbital entanglement may offer a resolution to conflicting experiments regarding the nature of the superconducting pairing in Sr_2RuO_4, which has been an unsolved question for decades. A fundamental assumption of classifying superconductors as a realization of singlet or triplet paired states is that one can write the wave function of each electron as a simple product of spatial and spin parts, which is not possible in the case of a strong entanglement between spin and orbital. Thus, the classification of the Cooper pairs in terms of singlets or triplets fundamentally breaks down, necessitating a description of the unconventional superconducting state of Sr_2RuO_4 beyond these pure spin eigenstates.

1.2 SOC in systems without inversion symmetry

As described in the previous section, spin degeneracy is a combined effect of inversion symmetry in space and time. However, if the system has no inversion centre, which is the usual case at the surface of solids due to a shape termination or in bulk systems with a zinc blende structure,[2] SOC can lift the spin degeneracy and lead to spin-split states.

In semiconductors with a zinc blende structure, the asymmetry of the underlying crystal structure (usually called bulk inversion asymmetry), together with SOC, gives rise to a Dresselhaus term in the Hamiltonian of the system [5]:

$$H_D = \beta(k_x\sigma_x - k_y\sigma_y). \tag{1.2}$$

Note only the linear k term is kept here, but there is also a cubic term that can be important with a large k. Together with the kinetic energy term

[2] For example, GaAs, InSb, and $Hg_xCd_{1-x}Te$ have a zinc blende structure.

$p^2/2m$, we obtain a pair of parabolic-like bands with an equal and opposite momentum shift away from the high-symmetry point (such as at Γ with $k = 0$), for example as shown in Fig. 1.2(d).

In semiconductor heterostructures, although the system has an inversion centre, the confinement potential near the surface region (usually called structure inversion asymmetry) breaks the inversion symmetry and can lead to a spin-split Rashba term [15]:

$$H_R = \alpha(k_x\sigma_y - k_y\sigma_x), \tag{1.3}$$

with α being the Rashba parameter proportional to the SOC strength λ and the potential gradient along the z direction dV/dz (i.e., $\alpha \propto \lambda dV/dz$). The energy dispersion of Rashba band is similar to that of the Dresselhaus state, making it a challenge to determine the absolute value of both contributions in a single sample. However, there is a substantial difference in the spin texture in momentum space, which can be simply checked by calculating the expectation value of spin operators for both Hamiltonians (Eq. 1.2 and Eq. 1.3). For Rashba spin splitting, the spin is perpendicularly locked with momentum and forms two chiral spin textures that have an axial symmetry about the (001) axis along k_z. On the other hand, Dresselhaus spin splitting has a spin texture only with a reflection symmetry to the (100) or (010) axis. The symmetry difference between the spin orientations allows an experimental way to distinguish them by measuring the electron's spin precession [16].

Rashba spin splitting has been extensively studied due to the wide availability of materials, such as the surface Shockley states in Au(111) [17], the two-dimensional electron gas state in noble-metal-based surface alloys [18], and heterostructures [19]. Since spin splitting would provide great opportunities for practical spintronic applications, high-energy-scale Rashba spin splitting is highly desirable for enhancing the coupling between electron spins and electricity relevant for spintronic functions. Efforts to achieve giant Rashba spin splitting ($\geq 100\,\mathrm{meV}$) have been conducted mainly in two-dimensional (2D) systems [17, 18, 20]. Recent discoveries in three-

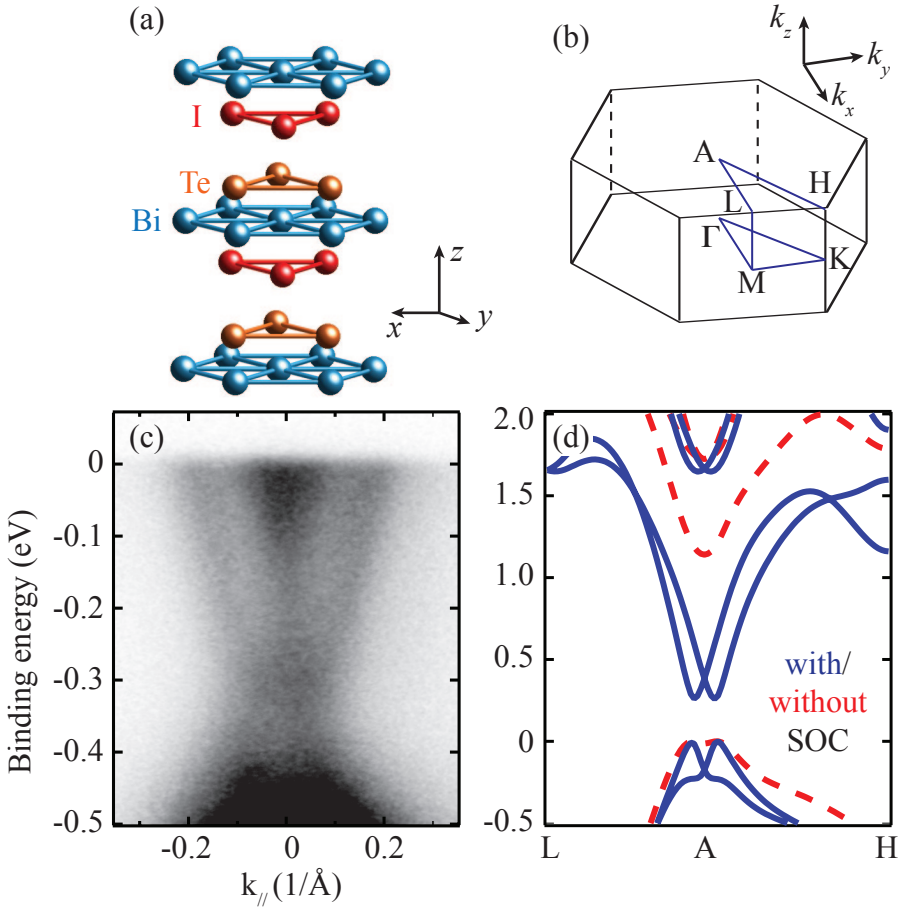

Figure 1.2: Rashba-type spin split bands of BiTeI. (a) Crystal structure of BiTeI. (b) Bulk Brillouin zone. (c) Band dispersion with Rashba-split conduction band measured by ARPES. (d) Bulk band structure calculated by DFT with (blue lines) and without (red dashed lines) SOC included.

dimensional (3D) TIs [7, 8] have fueled further exploration of materials with strong SOC. In Chapter 4, we will show that beside their exotic topological surface states, TIs also provide a new platform to achieve large-energy-scale Rashba spin splitting. Another good example of a 3D material with giant Rashba spin splitting is BiTeI [21–23], which we have also measured (Fig. 1.2). The huge spin splitting in BiTeI is derived from the large SOC of all the elements (Bi, Te, and I) and the material's layered structure with

its lack of natural termination [Fig. 1.2(a)], which leads to a polar surface. Our angle-resolved photoemission spectroscopy (ARPES) measured band dispersions show a pair of spin-splitting bands near the Fermi level and are supported by DFT calcualtions, as shown in Figs. 1.2(c) and (d). The DFT calculation shows that only the inclusion of SOC will produce the spin splitting state, indicating a SOC-driven Rashba-type spin splitting system.

1.3 Topological insulators

Recently, it has been discovered that band insulators with strong SOC can have a conducting spin-polarized surface state located inside the large bulk band gap. These materials, characterized by subtle topological invariants of band structure, rather than broken symmetries, define a new quantum phase of matter called topological insulators (TIs) [7, 8, 24–28]. The topological invariant is usually expressed as an integral involving the electron's wave function in momentum space, and is a unique index characterizing the electronic band structure of the material [26, 32]. Topological insulators have a non-trivial topological invariant that is different from the one of ordinary insulators (e.g. vacuum is a ordinary insulator). The discontinuity of these invariants in crossing the interface between topological and ordinary (e.g. vacuum) insulators demands an emergence of a new metalic state existing at the interface, in order to enable a transformation between the topological and ordinary insulating states. This exotic phase of matter, and associated topological surface state (TSS), have become a subject of intensive research in the past five years, because they have been predicted to have strong application potential in quantum electronic devices [29, 30] and to give rise to platforms for detecting new particles, such as majorana fermions [31].

Generally, most insulators thus far known are ordinary insulators, such as those classified as Mott insulators or band insulators. To find TIs in real materials, we need to develop criteria for recognizing them from their fundamental physical properties, such as bulk band structures. It is clear that the existence of a bulk energy gap is a necessary condition to host a gapless surface state. Another condition to be a TI is to have non-trival

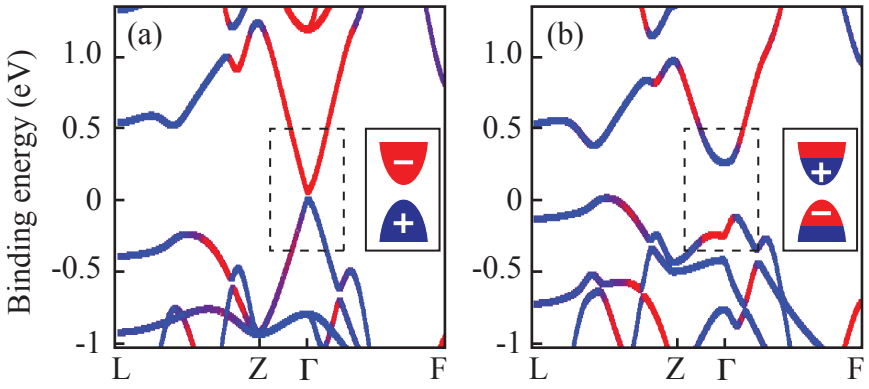

Figure 1.3: Band inversion of bulk bands in Bi_2Se_3. (a), (b) Bulk band structures of Bi_2Se_3 without (a) and with (b) SOC included, colored according to the parity of the bands. Red represents a bonding state with "+" parity, and blue represents an anti-bonding state with "−" parity. Insets are visual guides to the parities of the conduction and valence states at the Γ point. A band inversion can been seen at the time-invariant Γ point in (b) after SOC was included in the calculations.

Z_2 invariants. Based on the Z_2 invariant theory, we can identify systems with inversion symmetry as TIs, from knowledge of the parity eigenvalues of band states at time-reversal invariant points [32]. Therefore, the guiding principle to search for TI materials is that the material should have opposite parity at valence and conduction bands, and a band inversion should occur when the strength of some parameters, such as SOC, is tuned.

By using this method, we did analysis on the bulk band structure of Bi_2Se_3, which is the central material studied in this thesis. As shown in Fig. 1.3, the bulk bands are colored according to their parity, here defined by bonding and anti-bonding states. Without SOC included, the parities of valence and conduction bands at Γ point have opposite signs. However, their signs are inverted after the inclusion of SOC, indicating the occurrence of band inversion. In the DFT slab model, a spin-polarized surface state also appears simultaneously after the band inversion is induced by SOC[3], shown

[3] A series of slab band structures with different SOC values can be seen in Section 3.2, Fig. 3.8, and spin polarization of the surface state is discussed in Chapter 5 and 6.

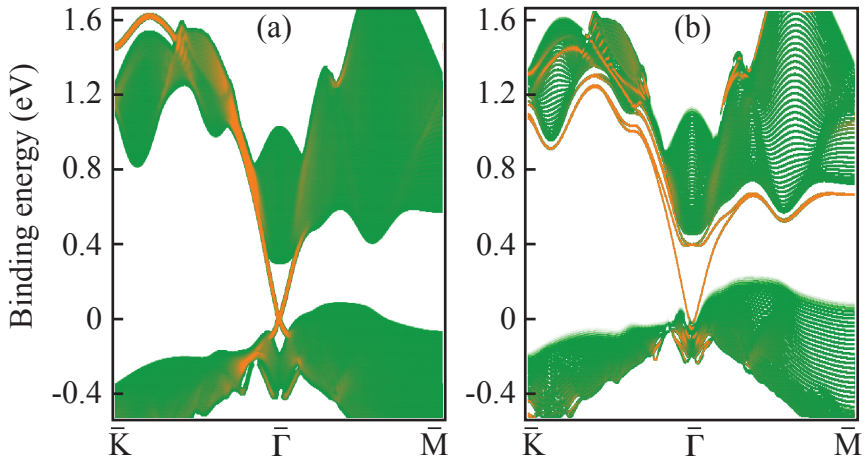

Figure 1.4: Topological surface states and Rashba-split bands of Bi_2Se_3. (a) Topological band structure with surface states shown in orange. (b) Coexistence of TSS and Rashba-split bands, both shown in orange. The Rashba-split band appears only after a downward band bending was introduced by adding a potential profile near the surface region, e.g., $V = -0.3e^{-z/19.1}$ eV.

in Fig. 1.4. By doing this analysis, we can deduce that Bi_2Se_3 is a strong topological insulator material. In fact, Bi_2X_3 (X = Bi, Te) has become the most promising 3D TI, attracting a great deal of interest in the past four years [33–35].

A fully spin-polarized topological surface state, an exotic quantum state of matter, is determined only by the non-trivial topological invariant of the bulk system. This means that no specific surface potential environment is required to obtain the TSS, and also that the TSS is topologically protected. These features substantially contradict the Rashba spin splitting state as described in the previous section. There, a confined potential is required near the surface region, and the size of Rashba spin splitting is proportional to the potential gradient. We can demonstrate the distinction between the TSS and the Rashba state by tuning the surface potential in Bi_2Se_3. In Fig. 1.4(a), when the atomic onsite potentials are the same, both in the bulk and at the surface, we obtain a TSS band standing alone inside of the bulk gap. In Fig. 1.4(b), when an additional potential profile is added

near the surface region, a pair of new bands with Rashba-like spin splitting appears, and the TSS band still remains. On the other hand, because of the robustness of the TSS, TIs have triggered extensive research activities and become one of the most interesting and active current topics in material physics.

In this thesis, we provide a systematic study of the band structure and wave function of the realistic TSS in Bi_2Se_3 by using ARPES and DFT. We address material issues regarding the surface instability and the impurity effects in Chapter 4. Our light-polarization-dependent study on the ARPES intensity maps reveals the full complexity of the wave function of TSS in real materials, which has a layer-by-layer entangled spin-orbital texture, as to be presented in Chapter 5. Based on the knowledge of the existence of a layer-by-layer entangled spin-orbital texture, we theoretically predicted and experimentally demonstrated the manipulation of photoelectron spin-polarization for the TSS in Chapter 6.

Although my Ph.D. research involved various SOC-related systems, including transition-metal oxides ruthenates and the kondo insulator SmB_6, this thesis will be devoted only to presenting our work on topological materials, so consistency can be maintained across the thesis.

Chapter 2

Angle-resolved photoemission spectroscopy

2.1 General principles

Angle-resolved photoemission spectroscopy (ARPES) is a momentum determined, low-energy electron excitation measurement technique that has been widely used to investigate complex systems, yielding especially notable success in high-T_c superconductors [36] and topological insulators [7]. During an experiment, a low-energy beam of monochromatized radiation – generated by a gas-discharged lamp, a laser, or a synchrotron beamline – is used to illuminate the sample to emit electrons by the photoelectric effect. The emitted electrons, named photoelectrons, travel to the sample surface in the solid and eventually escape into a vacuum, as described by the one-step or three-step model in Ref.[37]. In the vacuum, the emitted photoelectrons are detected by an electron-energy analyzer, and both their kinetic energy and emission angles are measured. Thus, the momentum of a photoelectron $\mathbf{p}$ in the vacuum can be determined by $p = \sqrt{2mE_{kin}}$ together with its polar (θ) and azimuthal (φ) emission angles. In the solid, the total energy and momentum conservation laws can be applied to the system of crystal and photoelectron during the photoexcitation process. The fact that there is a very short electron escape length ($\sim$ 5–10 Å) allows us to reasonably assume that there are no interactions between the photoelectron and the remaining electrons. When the photoelectron arrives at the surface, it has to consume a portion of the kinetic energy to overcome the perpendicular surface potential before escaping into the vacuum. Thus, the perpendicular component of

momentum is not conserved, but the parallel component is still conserved:

$$\mathbf{p}_{||} = \hbar\mathbf{K}_{||} = \sqrt{2mE_{kin}} \cdot \sin\theta, \tag{2.1}$$

where $\mathbf{K}$ is the momentum of the photoelectron inside the solid, with the sample surface assumed to be in the xy plane. By scanning the energy and momentum distribution of photoelectrons in real space, ARPES data provides a vivid picture to directly observe the Fermi contours and band structure in the solid. To associate the measured parameters with band structure, we would first write down the general expression of momentum in both angular space and k-space:

$$\begin{aligned}\mathbf{K} &= \frac{1}{\hbar}\sqrt{2mE_{kin}}(\cos\varphi\sin\theta\hat{i} + \sin\varphi\sin\theta\hat{j} + \cos\theta\hat{k}) \\ &= \mathbf{K}_x + \mathbf{K}_y + \mathbf{K}_z \\ &= \mathbf{k}_x + \mathbf{k}_y + \mathbf{k}_z + \mathbf{G},\end{aligned} \tag{2.2}$$

where the small $\mathbf{k}$ is the wave vector of a Bloch state in the Brillouin zone (BZ) and $\mathbf{G}$ is a reciprocal lattice vector. The polar angle θ and azimuthal angle φ are the normal spherical coordinates. Therefore, the band structure can be obtained by plotting the intensity distribution of electrons in a binding energy and momentum plane. Considering that only the momentum component parallel to the sample surface is conserved, a general ARPES measurement is not available to provide a 3D band structure, although some experimental methods have been developed to obtain 3D band mapping [38–40]. We note that the relationship in Eq. 2.2 is correct only in the plane of the sample surface.

In ARPES one needs low-energy incoming photons to obtain high-energy and high-momentum resolution, which is easy to achieve by looking at the momentum differential $\Delta\mathbf{K}$ from Eq. 2.1:

$$\Delta\mathbf{K}_{||} \simeq \sqrt{2mE_{kin}/\hbar^2} \cdot \cos\theta \cdot \Delta\theta. \tag{2.3}$$

In Eq. 2.3, any contribution from a fine energy resolution ΔE_{kin} is neglected.

Eq. 2.3 clearly shows that either using low photon energy (i.e. low E_{kin}) or detecting electrons with a large emission angle (i.e. large θ) would improve the momentum resolution, meaning a smaller $\Delta\mathbf{K}_{||}$. The lower photon energy also brings another benefit: easier achievement of a higher energy resolution. However, the drawback of working at low photon energies is the extreme surface sensitivity due to the associated short mean free path for the unscattered photoelectrons ($\sim$ 5–10 Å for 20–100 eV kinetic energy). The high surface sensitivity thus limits the application of ARPES for bulk properties investigation and requires an atomically clear sample surface and an ultra-high vacuum condition (usually lower than 5×10^{-11} torr).

The technical details of the in-house ARPES system at the University of British Columbia (UBC) can been found in our previous group members' Ph.D. theses [41, 42]. The establishment of a theoretical expression for the ARPES spectra is described in Damascelli's review papers [36, 37] and references therein. Here, we would rather focus on the calculation of ARPES intensity, which is used to produce all the results in Chapter 5.

2.2 ARPES intensity calculation

2.2.1 General formulae

The photoemission intensity measured at a momentum $\mathbf{k}$ is proportional to the transition probability for an optical excitation between the ground state $\Psi_{inital}(\mathbf{k})$ and one of the possible final states $\Psi_{final}(\mathbf{k})$, which can be written using Fermi's golden rule:

$$I(\mathbf{k}) = \frac{2\pi}{\hbar}|\langle\Psi_{final}|H_{int}|\Psi_{initial}\rangle|^2\delta(E_{final} - E_{initial} - h\nu), \tag{2.4}$$

where E_{inital} and E_{final} are the initial- and final-state energies of the system, and $h\nu$ is the photon energy used to excite photoelectrons. The interaction between electrons and photons is treated as a perturbation given by:

$$H_{int} = -\frac{e}{2mc}(\mathbf{A}\cdot\mathbf{p} + \mathbf{p}\cdot\mathbf{A}) = -\frac{e}{mc}\mathbf{A}\cdot\mathbf{p}, \tag{2.5}$$

where $\mathbf{p}$ is the electronic momentum operator and $\mathbf{A}$ is the electromagnetic vector potential. Note that here we did not include the relativistic term in H_{int}, which is $-\frac{\hbar e}{4m^2c^2}(\nabla V \times \mathbf{s}) \cdot \mathbf{A}$. In the dipole approximation and by using the commutation relation $\hbar\mathbf{p}/m = -i[\mathbf{r}, H]$, we can write:

$$I(\mathbf{k}) \propto |\langle \Psi_{final} | \hat{\epsilon} \cdot \mathbf{r} | \Psi_{initial} \rangle|^2, \tag{2.6}$$

where $\hat{\epsilon}$ is the unit vector along the polarization direction of the vector potential $\mathbf{A}$. We call the term inside the square modulus the matrix element:

$$M(\mathbf{k}) = \langle \Psi_{final}(\mathbf{k}) | \hat{\epsilon} \cdot \mathbf{r} | \Psi_{initial}(\mathbf{k}) \rangle. \tag{2.7}$$

Then we can rewrite the photoemission intensity as $I(\mathbf{k}) \propto |M(\mathbf{k})|^2$.

2.2.2 Initial states

Here we describe the wave function of the initial state $\Psi_{initial}$ based on a tight-binding (TB) model. In this model, $\Psi_{initial}$ can be written as a linear combination of the wave functions at each basis set.

$$\Psi_{initial} = \sum_i \psi_i, \tag{2.8}$$

where i is the index of the basis set, which usually presents atomic orbitals, atom sites, and spin. Since the ARPES intensity is momentum $\mathbf{k}$ dependent, we separate the $\mathbf{k}$ part of the wave function from the spatial part in $\Psi_{initial}$ to explicitly show the momentum information:

$$\Psi_{initial} = \sum_i C_i^{\uparrow}(\mathbf{k})\phi_i |\uparrow\rangle + C_i^{\downarrow}(\mathbf{k})\phi_i |\downarrow\rangle. \tag{2.9}$$

$C_i^{\uparrow,\downarrow}$ is the $\mathbf{k}$-dependent expansion coefficients obtained by diagonalizing the TB Hamiltonian in $\mathbf{k}$ space; $|\uparrow\rangle$ and $|\downarrow\rangle$ are the eigenstates of the Pauli matrix σ_z, representing the spin basis; and ϕ_i is the local spatial wave

function of the atomic orbitals:

$$\phi = R_{n,l}(r)Y_{l,m}, \tag{2.10}$$

where l, m is the angular momentum, $R_{n,l}(r)$ is the radial part of the Bloch wave function, and $Y_{l,m}$ are the real spherical harmonics. Taking Bi_2Se_3 as an example, the wave function of the initial state near the Fermi level has only p orbital characters ($4p$ for Se and $6p$ for Bi atoms), therefore $l = 1$ and the spatial wave functions for the p_x, p_y, and p_z orbitals are:

$$\begin{aligned}
\phi_{p_x} &= \sqrt{\frac{1}{2}}(Y_{1,-1} - Y_{1,1})R_{n,l}(r); \\
\phi_{p_y} &= i\sqrt{\frac{1}{2}}(Y_{1,-1} + Y_{1,1})R_{n,l}(r); \\
\phi_{p_z} &= Y_{1,0}R_{n,l}(r).
\end{aligned} \tag{2.11}$$

2.2.3 Final states and selection rules

In our model, the final states are treated as free electrons whose wave function can be described by a plane wave $\Psi_{final} = e^{i\mathbf{k}\cdot\mathbf{r}}$, which can be expressed as a superposition of spherical waves:

$$e^{i\mathbf{k}\cdot\mathbf{r}} = 4\pi \sum_{l'=0}^{\infty} i^{l'} j_{l'}(\mathbf{k}\cdot\mathbf{r}) \sum_{m'=-l'}^{m'=l'} Y^*_{l',m'}(\theta_\mathrm{k}, \varphi_\mathrm{k}) Y_{l',m'}(\theta, \varphi), \tag{2.12}$$

where $j_{l'}(\mathbf{k}\cdot\mathbf{r})$ is the spherical bessel function.

Plugging Eq. 2.9, 2.10, and 2.12 into Eq. 5.3, we obtain:

$$M(\mathbf{k}) = \sum_i (C_i^{\uparrow}(\mathbf{k})|\uparrow\rangle + C_i^{\downarrow}(\mathbf{k})|\downarrow\rangle)\mathcal{G}^i_{l',l}(\theta_\mathrm{k}, \varphi_\mathrm{k})\mathcal{B}^i_{n,l,l'}, \tag{2.13}$$

where $\mathcal{G}^i_{l',l}$ is the integral of the angular wave function and $\mathcal{B}^i_{n,l}$ is the integral of the radial wave funciton. $\mathcal{G}^i_{l',l}$ contains the information of the light polarization and photoemission channels, which determines the selection rules:

$$\mathcal{G}^{i}_{l',l}(\theta_{\mathrm{k}},\varphi_{\mathrm{k}}) = \int \sum_{m'=-l'}^{m'=l'} Y^{*}_{l',m'}(\theta_{\mathrm{k}},\varphi_{\mathrm{k}}) Y_{l',m'}(\theta,\varphi)\hat{\epsilon}\cdot\hat{r}Y_{l,m}(\theta,\varphi)d\Omega, \quad (2.14)$$

We further expand the interaction term $\hat{\epsilon}\cdot\hat{r}$ in Eq. 2.14 into spherical harmonics:

$$\hat{\epsilon}\cdot\hat{r} = \sqrt{\frac{4\pi}{3}}(\epsilon_z Y_{1,0} + \frac{-\epsilon_x + i\epsilon_y}{\sqrt{2}}Y_{1,1} + \frac{\epsilon_x + i\epsilon_y}{\sqrt{2}}Y_{1,-1}), \quad (2.15)$$

Based on Eq. 2.14 and 2.15 we derive the explicit expression of the angular integral:

$$\begin{aligned}\mathcal{G}^{i}_{l',l}(\theta_{\mathrm{k}},\varphi_{\mathrm{k}}) = \sum_{\mu=-1}^{\mu=1} (&\frac{\epsilon_x + i\epsilon_y}{\sqrt{2}}\delta_{\mu,-1} + \epsilon_z\delta_{\mu,0} + \frac{-\epsilon_x + i\epsilon_y}{\sqrt{2}}\delta_{\mu,1}) \\ &\cdot Y_{l',m+\mu}(\theta_{\mathrm{k}},\varphi_{\mathrm{k}})C^{1,l,l'}_{\mu,m,m+\mu},\end{aligned} \quad (2.16)$$

where δ is the delta function, and $C^{1,l,l'}_{\mu,m,m+\mu}$ is the Clebsch-Gordan coefficient, an integral product of three spherical harmonics, as defined by $\langle 1,\mu;l,m|l',m+\mu\rangle$. Eq. 2.16 has a non-zero value only at $l' = l \pm 1$, and this is how we obtain the optical selection rule: $l' = l \pm 1$.

For the case of Bi_2Se_3, we have $l = 1$ because of the p orbitals and therefore we will have two possible photoemission channels: p-to-s excitation for $l' = 0$ and p-to-d excitation for $l' = 2$. The probability of exiting photoelectrons from each channel depends on the magnitude of the radial integral $\mathcal{B}^{i}_{n,l,l'}$, which has the form:

$$\mathcal{B}^{i}_{n,l,l'} = \int i^{l'} j_{l'}(\mathbf{k}\cdot\mathbf{r})R_{n,l}(r)r^3 dr. \quad (2.17)$$

For the surface state of Bi_2Se_3, we focus on electronic states near the $\bar{\Gamma}$ point with $\theta_k \leq 4^\circ$, which corresponds to a nearly normal photoemission. The selection rule for p-to-s and p-to-d excitations basically has the same function in terms of the in-plane angle φ_{k} for normal photoemission. There-

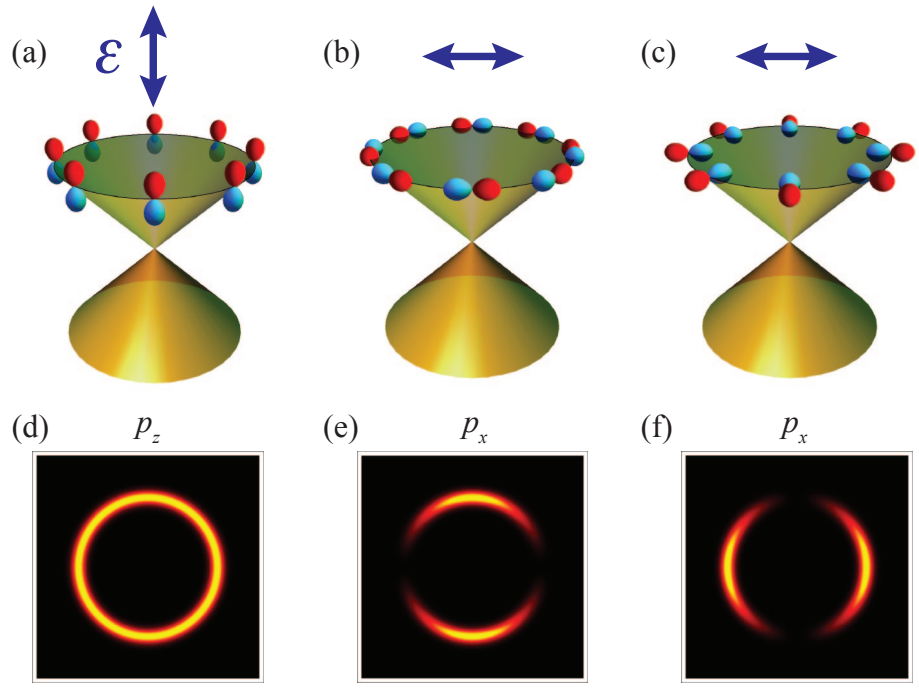

Figure 2.1: Sketch of selection-rule-determined ARPES intensity maps. (a)–(c) Topological Dirac states with p_z orbital character (a), with in-plane orbitals tangential to the momentum (b), and with in-plane orbitals radial to the momentum (c). The incident light is polarized along the z direction for (a), and along the x direction for (b) and (c). (d-f) Expected ARPES intensity maps according to the optical selection rule for cases shown in (a) to (c), respectively.

fore, the selection rule for linearly polarized light can be simplified into this description: the linearly polarized light only excites photoelectrons from orbitals that orient along the same direction of the light polarization. For example: $x/y/z$-polarized light only excites photoelectrons from $p_x/p_y/p_z$ orbitals, respectively, as represented in Fig. 2.1.

2.2.4 Measured spin polarization

So far, we have shown general formulae used in our photoemission intensity calculations. In this subsection, we will focus on the spin-resolved

photoemission intensity and show how to calculate the spin polarization of photoelectrons measured by spin- and angle-resolved photoemission spectroscopy (SARPES). For simplicity, we define:

$$M_i \equiv \mathcal{G}^i_{l',l}(\theta_{\rm k}, \varphi_{\rm k})\mathcal{B}^i_{n,l,l}, \tag{2.18}$$

with M_i representing the matrix element, which is constant for a certain light polarization and experimental geometry when $\theta_k \approx 0$. Therefore, we can write the photoemission intensity as the sum of intensities from spin up and spin down channels:

$$I(\mathbf{k}) \propto I^{\uparrow}(\mathbf{k}) + I^{\downarrow}(\mathbf{k}), \tag{2.19}$$

with

$$\begin{aligned} I^{\uparrow}(\mathbf{k}) &= |\sum_i C_i^{\uparrow}(\mathbf{k}) M_i|^2 \\ I^{\downarrow}(\mathbf{k}) &= |\sum_i C_i^{\downarrow}(\mathbf{k}) M_i|^2. \end{aligned} \tag{2.20}$$

The measured spin polarization vector (P) for SARPES is defined by $P = [P_x, P_y, P_z]$:

$$P_{x,y,z} = \frac{I^{\uparrow}_{x,y,z} - I^{\downarrow}_{x,y,z}}{I^{\uparrow}_{x,y,z} + I^{\downarrow}_{x,y,z}}. \tag{2.21}$$

In Chapter 5, Section 5.6, we use the above formulae to further demonstrate quantum interference effects in ARPES, and show a manipulation of photoelectron spin polarization in SARPES, which is a substantial aspect of this thesis.

Chapter 3

Ab initio tight-binding model

Besides using angle-resolved photoemission spectroscopy (ARPES) to conduct my Ph.D. research projects, I also spent a substantial amount of time on density functional theory (DFT) calculations, the quantitative technique for computing ground-state properties of materials [43]. These two techniques are a good combination, because ARPES is the most direct experimental method to probe electronic structures, and DFT is the most accurate theoretical method to calculate the electronic structures of complex systems.

In this chapter, we describe the methodology behind the ab initio tight-binding (TB) model which was used for the work presented in Chapters 5 and 6. The purpose of developing an ab initio TB approach is to allow us to quantitatively understand the experimental results using a minimal model to describe the electron wavefunction, i.e. in terms of the smallest possible basis set. The key ingredients to construct this ab initio TB model are the lattice onsite energies and the coupling strength between lattice sites, which are obtained by performing a bulk band calculation by DFT. A minimal basis set, i.e. only involving p orbitals, is chosen during the extraction of those onsite and coupling parameters. The atomic spin-orbit coupling (SOC) term is added as a free parameter in our TB model. The SOC effect in the ab initio TB model is checked by comparing the results to those from a DFT calculation inclusive of SOC. A detailed description for constructing ab initio bulk and slab TB models is given in Sections 3.1 and 3.2, respectively. Here, we start by discussing in details the advantages and disadvantages of the ab initio TB model as compared to a standard DFT approach.

Today DFT has already become a standard method for ab initio calculations in chemistry and solid state physics. DFT calculation gained popular-

ity over the past decades because it yields very accurate results for complex materials at low cost. Several packages are available to use for DFT calculations in solid state physics, such as WIEN2k [44, 45], which I have used most of the time, VASP [46–49], LMTO [50], SIESTA [51], ABINIT [52], PWScf [53], and CRYSTAL [54]. However, there are some limitations to using standard DFT packages. One well-known disadvantage is the lack of proper treatment for many body interactions in strongly correlated systems. Although improved treatments of electron correlations have been developed, including the dynamical mean-field theory [55] and quantum Monte Carlo approaches [56], the application of these advanced methods is at present too computationally demanding to be generally applied to complex systems. Another limitation is the complexity of the method, which is unadjustable and involves many built-in parameters. Since our materials of interest here are weakly correlated systems, the latter problem is more relevant to our study. In this chapter, we will discuss and show how to overcome the limitations on computational size and unadjustable parameters by developing an ab initio TB model.

This ab initio TB model becomes particularly useful in a way that allows us to study materials by using a minimal model but with ab initio accuracy. Because the implementation of this method is highly determined by the particular problem or application, at present no standard packages are available. Nevertheless, we can follow some routines to construct the ab initio TB model, as will be described in this chapter. The method of this model has several advantages compared to regular DFT calculations. First, the ab initio TB model can handle calculations of large-scale systems (≥ 200 atoms) without reaching computational limits. Second, and most important, we can gain full access to the Hamiltonian of the system, and all the parameters are adjustable. Of course, there are also some drawbacks to this model. For example, it is not appropriate for studying problems with low symmetries, such as electronic reconstructions induced by continuous transition of potential environments from the bulk to the surface. It does, however, have great advantages for symmetry-related problems, such as surface states in topological insulators (TIs). Since the surface and bulk

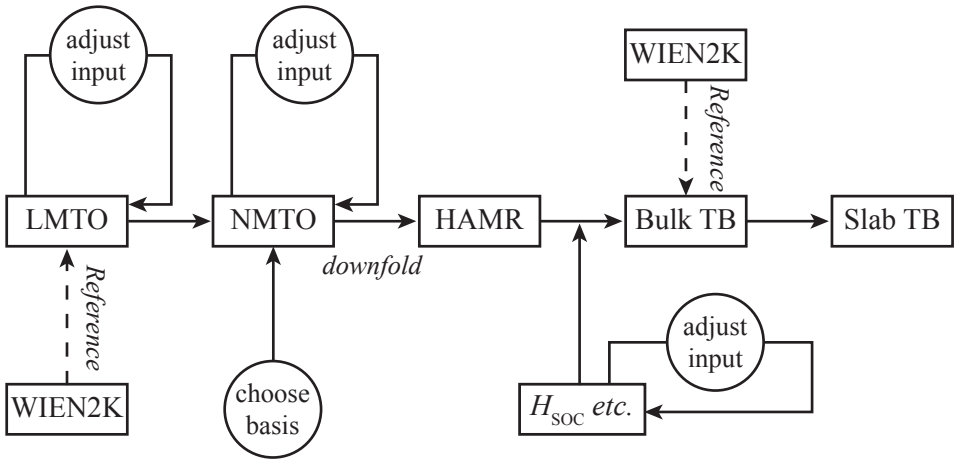

Figure 3.1: Procedural flow for constructing a tight-binding (TB) model. Note that HAMR is the real space Hamiltonian containing the hopping integrals; H_{SOC} is the local spin-orbit coupling Hamiltonian.

potential environments are similar in TI materials, we can construct an ab initio TB model for a finite system, such as a slab model to mimic surface problems, based on the hopping parameters (representing the coupling strength between lattice sites) obtained from a bulk DFT calculation. In this way, we can easily break the computational limit encountered in standard DFT slab calculations. Here, I will take Bi_2Se_3 as an example to explicitly show this method step by step.

3.1 Ab initio bulk tight-binding model

Our goal is to build a minimal model to describe the topological surface state (TSS) in Bi_2Se_3. Our approach should be generic and adaptable for other similar studies. We start with introducing how to construct an ab initio TB model for the bulk. In the next section, we will show how to build a slab model based on the bulk model without involving additional DFT calculations.

Now we give a short summary of the steps to construct an ab initio

TB Hamiltonian, as shown in Fig. 3.1. *Step I*, we perform a bulk DFT calculation by using the linear muffin-tin orbital (LMTO) method [50]. The input parameters of the LMTO, such as muffin-tin radius and basis set, are adjusted according to the degree of agreement between the LMTO and the WIEN2k band structures. Note that we use the band structure calculated by using the WIEN2k package as a reference. *Step II*, we use the optimized input file from the LMTO to perform the same calculation but employing the order-N muffin-tin orbital (NMTO) method [57]. A minimal basis set is decided at this step, and the corresponding parameters are adjusted until we obtain good agreement between the band structures calculated with a full basis set and with a minimal basis set. *Step III*, we use the NMTO built-in function to downfold the bulk band structures into a minimal basis set formed by selected atomic orbitals. The downfold procedure gives us the hopping integrals and stores them in the HAMR file. *Step IV*, we use the hopping integrals in real space to construct a TB Hamiltonian in the momentum **k**-space for the bulk system. At this stage, we can add extra local Hamiltonians, such as those coming from spin-orbit coupling (SOC), electric or magnetic fields, etc. *Step V*, based on the bulk TB Hamiltonian, we can construct a Hamiltonian for a freestanding TB slab system with sufficient thickness by a simple truncation. We obtain the energy eigenvalues and eigenstates of the system by using the matrix diagonalization as a function of the wave vector $\mathbf{k}_{||}$ in the surface Brillouin zone (BZ). Since the basis set of the TB Hamiltonian is Wannier functions [58], the wave function of the electronic states of the system is the linear combination of these Wannier functions. When the Wannier orbitals retain the same symmetry of the atomic orbitals, we can approximate the Wannier function by the atomic wave function.

In Fig. 3.2, we show good agreement between the WIEN2k and optimized LMTO band structures from the bulk Bi_2Se_3. In particular, the occupied valence bands are in excellent agreement. But there is a visible offset for the unoccupied conduction bands that is difficult to further improve in this case and can contribute to the different potential approximations used in LMTO (which uses sphere potential) and WIEN2k (which uses full potential).

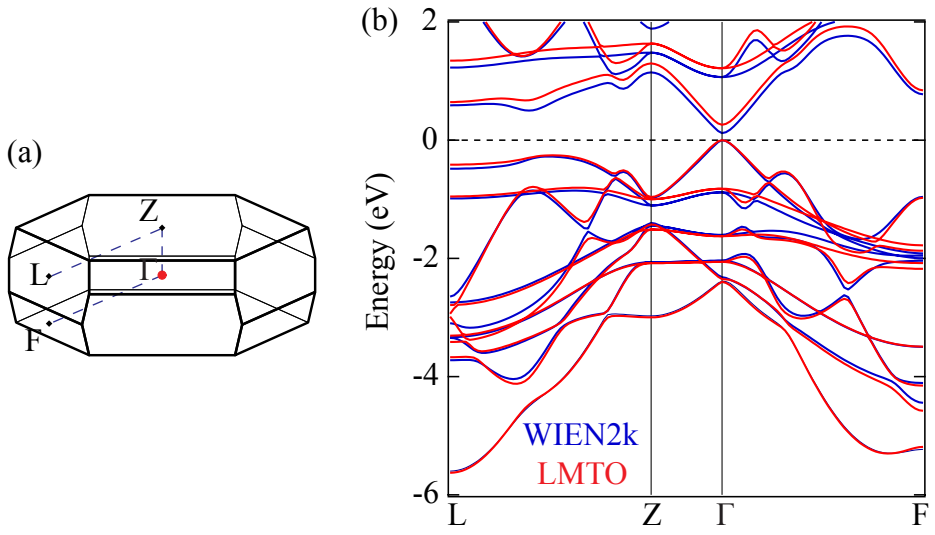

Figure 3.2: Comparison between the linear muffin-tin orbital (LMTO) and WIEN2k band structures. (a) Brillouin zone of bulk Bi_2Se_3, with dashed lines connecting high symmetric momentum points. (b) Bulk band structures calculated by using WIEN2k and optimized LMTO, respectively.

Since the valence and conduction bands of Bi_2Se_3 mainly have p orbital characters, we are able to downfold the band structures near the Fermi level with a minimal basis set $\{p_x, p_y, p_z\}$ from two Bi and three Se atoms, which gives us a minimal TB model with 15 bands. The real space parameters for the TB model contain the hopping integral $t_{i,j,\tau,\tau'}$ between different atom sites and connecting vectors $R_{i,j}$, as illustrated in Fig. 3.3. We use the notations i, j to represent atom positions and τ to represent atomic orbitals. The Hamiltonian in $\mathbf{k}$-space can be constructed by applying Fourier transformation, written as:

$$H_0(\mathbf{k}) = \sum_{i,j,\tau,\tau'} t_{i,j,\tau,\tau'} e^{i\mathbf{k}\cdot\mathbf{R_{i,j}}} a^\dagger_{i,\tau} a_{j,\tau'}. \tag{3.1}$$

The eigenstates of the Hamiltonian (Eq. 3.1) are a linear combination of

```
  ====================================
  Real Space hamiltonian (eV)
  ====================================


INT=    1
|Int.bet. Se1 0001 / Se1 0001                    |
|Dist= 0.000000  Trans. vecs. :  0  0  0         |
|Connecting vector:   0.00000  0.00000  0.00000  |

                  py          pz          px
py               -4.51207     0.00000     0.00000
pz                0.00000    -4.29555     0.00000
px                0.00000     0.00000    -4.51207

-----------------------------------------------
INT=    2
|Int.bet. Bi  0004 / Se1 0001                    |
|Dist= 1.272415  Trans. vecs. : -1  0  0         |
|Connecting vector:  -1.00000  0.00000  0.78679  |

                  py          pz          px
py               -0.42425     0.00000     0.00000
pz                0.00000     0.40199    -1.05214
px                0.00000    -1.09768     1.00482

-----------------------------------------------
INT=    3
|Int.bet. Bi  0004 / Se1 0001                    |
|Dist= 1.272415  Trans. vecs. :  0 -1  0         |
|Connecting vector:   0.50000 -0.86603  0.78679  |

                  py          pz          px
py                0.64755    -0.95062    -0.61881
pz               -0.91118     0.40199     0.52607
```

Figure 3.3: Illustration of the partial content of the Bi_2Se_3 HAMR file, which is obtained by using a minimal basis set $\{p_x, p_y, p_z\}$.

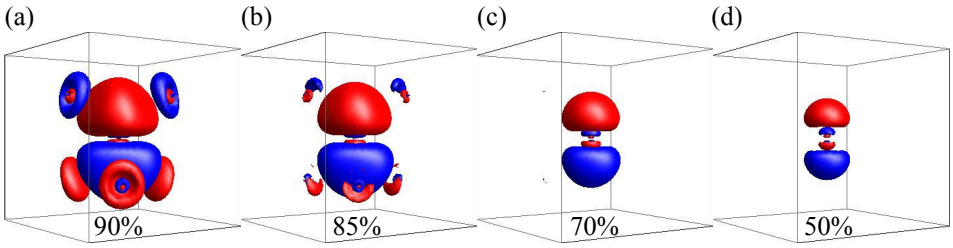

Figure 3.4: Isosurface of charge density from the Wannier orbitals p_z, with four isovalues (a)–(d): 0.9, 0.85, 0.7, and 0.5, respectively. Red and blue indicate the phase of the orbital.

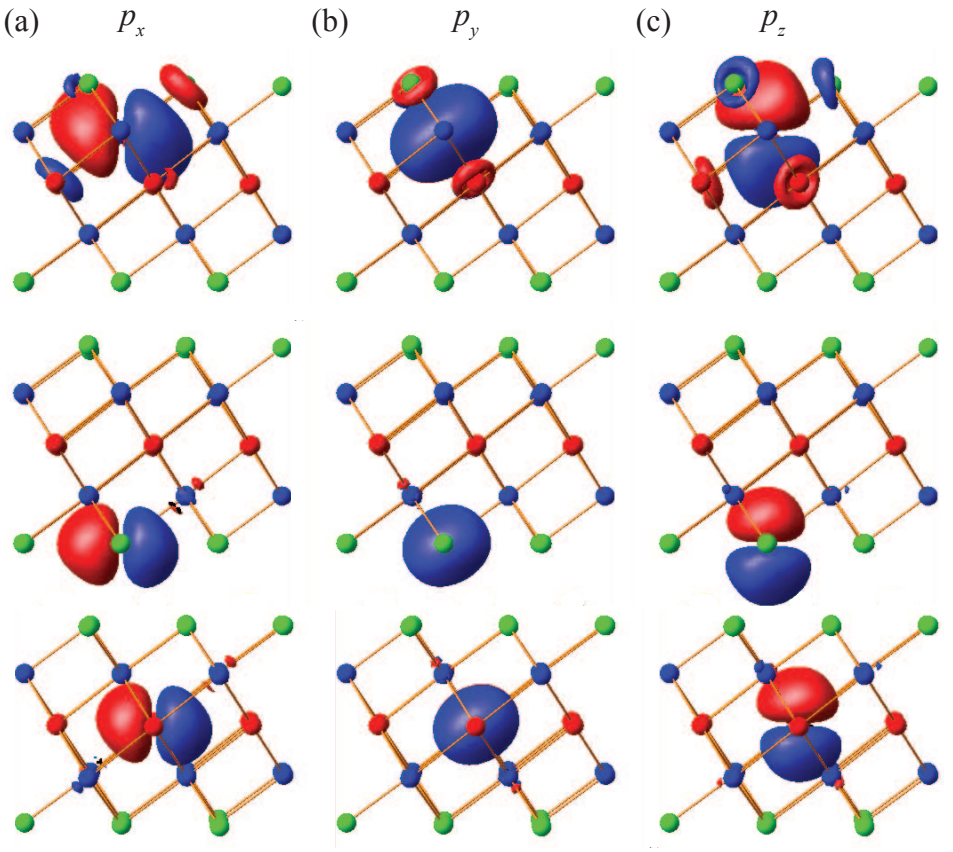

Figure 3.5: (a)–(c) Wannier orbitals of p_x, p_y, and p_z with an isovalue of 90%, plotted in the crystal lattice of Bi_2Se_3.

Wannier functions [58]:

$$\Psi(\mathbf{k}) = \sum_{i,\tau} C_{i,\tau}(\mathbf{k}) w_{i,\tau}. \tag{3.2}$$

One of the most important advantages of ab initio TB model is that it allows us to expand the Hamiltonian by adding other local terms, such as the SOC term, without involving intensive computational resources. The simplest SOC expression is the atomic SOC, which is derived based on the symmetry of atomic wave functions and is written as:

$$H_{\mathrm{SOC}} = \lambda \mathbf{L} \cdot \mathbf{S}, \tag{3.3}$$

where λ is the SOC parameter, $\mathbf{L}$ is the orbital angular momentum, and $\mathbf{S}$ is the spin angular momentum. Before we add this local term H_{SOC} into the Hamiltonian of Eq. 3.1, we need to check the spatial charge distribution of the Wannier orbitals and make sure that we can approximate them with a picture of the atomic orbitals. As shown in Fig. 3.4, the isosurface of charge density from p_z, shown by a Wannier orbital, indeed remains in the atomic p_z orbital shape, particularly when the isovalue that defines the percentage of charge density contained inside an isosurface is below 80%. Plotting Wannier orbitals in the crystal lattice, as in Fig. 3.5, shows a quite extended spatial charge distribution around each atom site, which is important for forming bonding and anti-bonding states in the Bi_2Se_3 system.

To add the SOC effect into the bulk TB Hamiltonian, we have to double the basis set by considering spin up ($\uparrow$) and spin down ($\downarrow$) for each electron. Now the basis set at each atom site is:

$$|p_x,\uparrow\rangle, |p_y,\uparrow\rangle, |p_z,\uparrow\rangle, |p_x,\downarrow\rangle, |p_y,\downarrow\rangle, |p_z,\downarrow\rangle. \tag{3.4}$$

By writing the SOC Hamiltonian (Eq. 3.3) in the basis set of atomic p or-

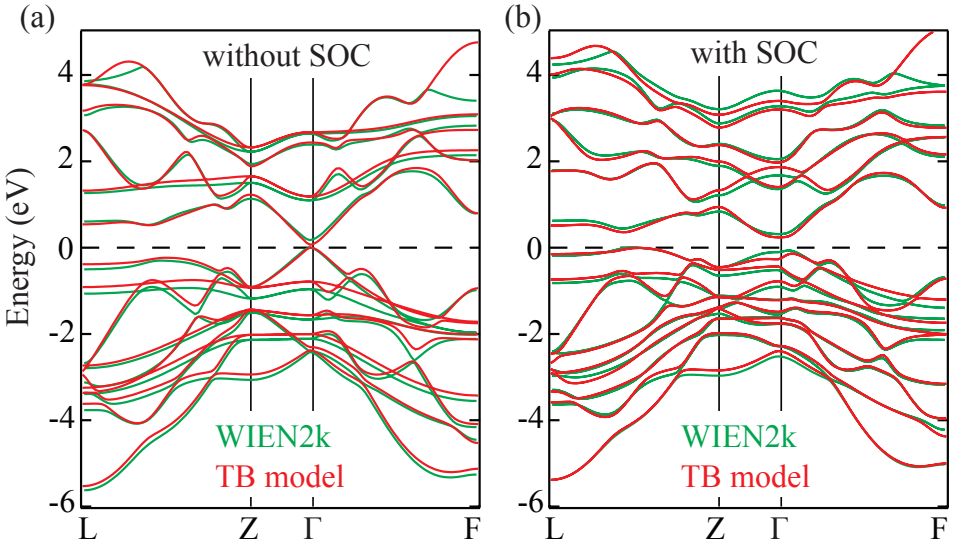

Figure 3.6: Comparison between the TB model and WIEN2k band structures. Bulk band structures of Bi_2Se_3 obtained from WIEN2k and from a TB model with (a) and without (b) spin-orbit coupling (SOC) included.

bitals and real spins, we obtain:

$$H_{\mathrm{SOC}} = \frac{\lambda}{2} \begin{bmatrix} 0 & -\mathrm{i} & 0 & 0 & 0 & 1 \\ \mathrm{i} & 0 & 0 & 0 & 0 & -\mathrm{i} \\ 0 & 0 & 0 & -1 & \mathrm{i} & 0 \\ 0 & 0 & -1 & 0 & \mathrm{i} & 0 \\ 0 & 0 & -\mathrm{i} & -\mathrm{i} & 0 & 0 \\ 1 & \mathrm{i} & 0 & 0 & 0 & 0 \end{bmatrix} \tag{3.5}$$

This is the SOC Hamiltonian we added as a local term into Eq. 3.1. The SOC parameters for Bi and Se atoms are taken from Wittel's spectral data: $\lambda_{\mathrm{Bi}} = 1.25\,\mathrm{eV}$ and $\lambda_{\mathrm{Se}} = 0.22\,\mathrm{eV}$ [59]. In Fig. 3.6, we compare the bulk band structures calculated by WIEN2k and by the ab initio TB model with and without SOC included, respectively. In both cases, the overall agreement between the two methods is good, which means that the atomic SOC approximation is sufficient to capture the realistic SOC effects in the Bi_2Se_3

system. By combining Eq. 3.1 and Eq. 3.3, the TB Hamiltonian for the bulk system becomes:

$$H_{\text{bulk}} = H_0 + \sum_i H_{\text{SOC}}. \tag{3.6}$$

3.2 Ab initio slab tight-binding model

Now that we have a TB Hamiltonian with SOC included for the bulk system, the slab TB Hamiltonian used to study surface states can be created by following three steps: (1) we set k_z in the bulk Hamiltonian to zero; (2) using the bulk unit cell as a unit block, which is one quintuple layer (QL) for Bi_2Se_3, as shown in Fig. 3.7, we repeatedly duplicate the unit block along the z direction and make a supercell with a finite thickness, such as 50 QLs; and (3) we simply truncate the supercell Hamiltonian by discarding the hopping integrals that are coming from any atom sites above(below) the top(bottom) surface layer, i.e., outside of the supercell.

The simple truncation of the effective TB model means that this approach contains no surface-specific information, being based exclusively on the bulk Wannier functions. The accuracy of this approach might be questionable, due to the fact that TB parameters near the surface might be slightly different from those in the bulk because of the possible surface potential. Instead of applying the naive truncation, one can refine the procedure so as to incorporate the changes to the TB parameters near the surface. To do so, we can perform the bulk calculation and a thin slab calculation together. Upon aligning the on-site energies in the interior of this slab with the bulk values, the changes to the TB parameters near the surface can be inferred. However, it has been found that the topological surface states are essentially the same with and without the surface potential corrections [60]. On the other hand, the truncation method is very useful as an appraisal for illustrating the"topologically protected" surface states that arise as a manifestation of the bulk electronic structure [7]. An alternative strategy for calculating the surface bands is to use Green's function for the semi-infinite crystal as a function of the atomic plane, which can be obtained via iterative methods [61–63]. For simplicity, here we use a truncated-slab approach to

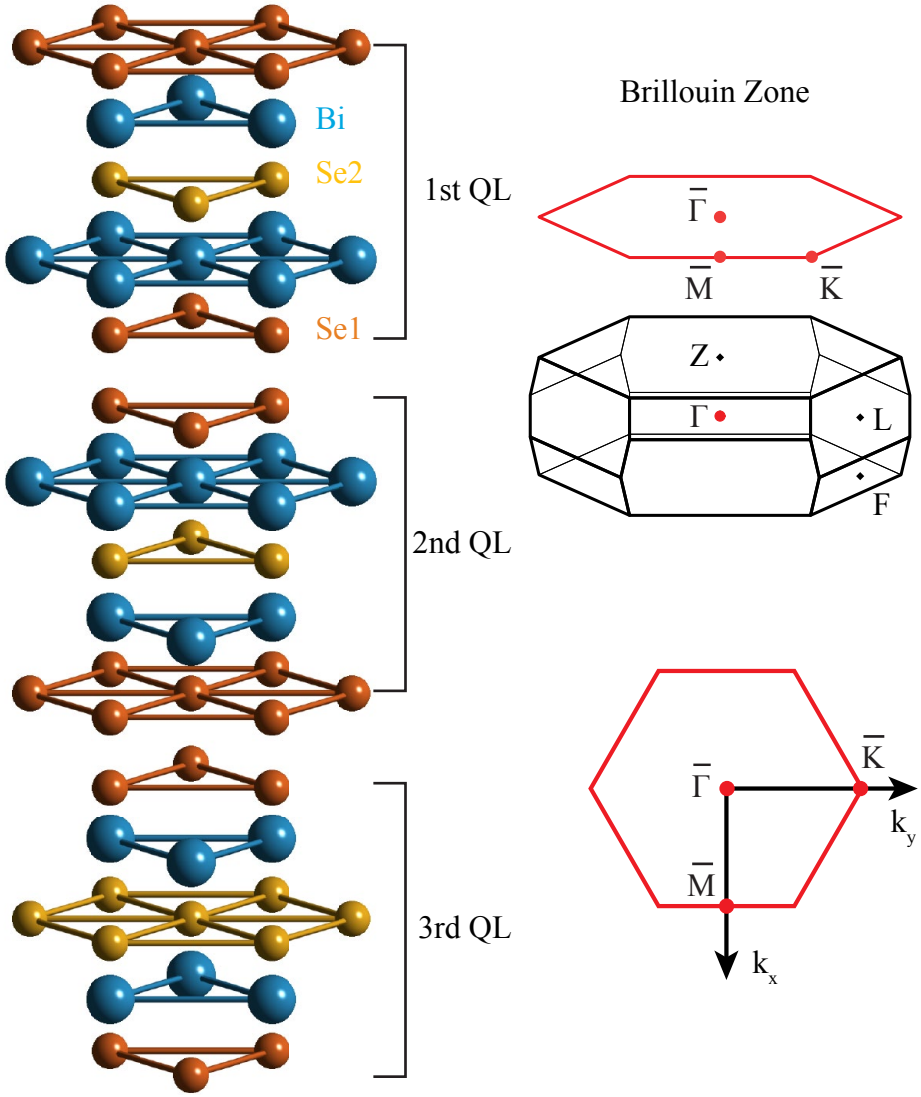

Figure 3.7: Left: Crystal structure of Bi_2Se_3 with a unit cell formed by five atomic layers, called one quintuple layer (QL). A structure of three QLs is shown here. Right: Bulk Brillouin zone (black) and surface Brillouin zone (red) in momentum space.

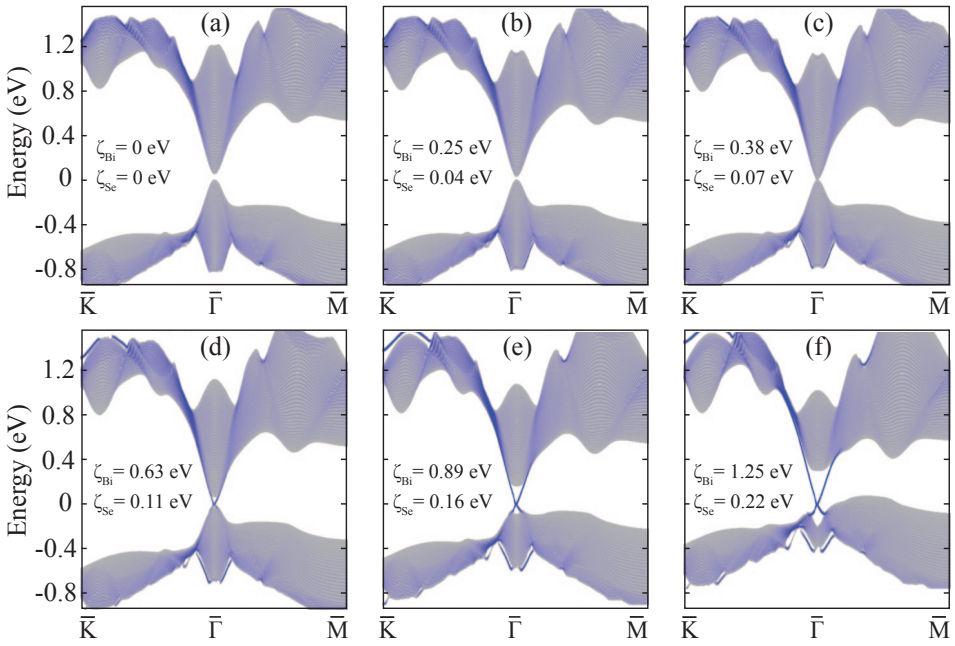

Figure 3.8: Band inversion and topological surface states in Bi_2Se_3. (a)–(f) Band dispersions obtained from a 250-atomic-layers slab for Bi_2Se_3 with several SOC values. As the SOC strength increases, the gap between the bulk bands (grey) first closes [(a)–(c)] and then reopens [(d)–(f)], indicating a band inversion induced by tuning the SOC. A gapless surface state (blue) appears simultaneously when the band inversion occurs.

study the topological surface properties of topological insulators.

Since the SOC value λ is a free parameter in the TB Hamiltonian, and in order to exhibit how SOC induces topological surface states, we calculate the band dispersions as a function of SOC strength. In Fig. 3.8, we plot the band dispersions obtained with a 250-atomic-layer slab TB model. By varying the SOC value, we can see that the gap between the bulk bands first closes with increasing SOC [Figs. 3.8(a)–(c)], then reopens once the SOC is large enough [Figs. 3.8(d)–(f)]. As expected from the bulk electronic structure of topological insulators, a band inversion occurs after the gap reopens from zero. Meanwhile, a gapless surface state simultaneously appears when the band inversion occurs. The topological surface state becomes more evident

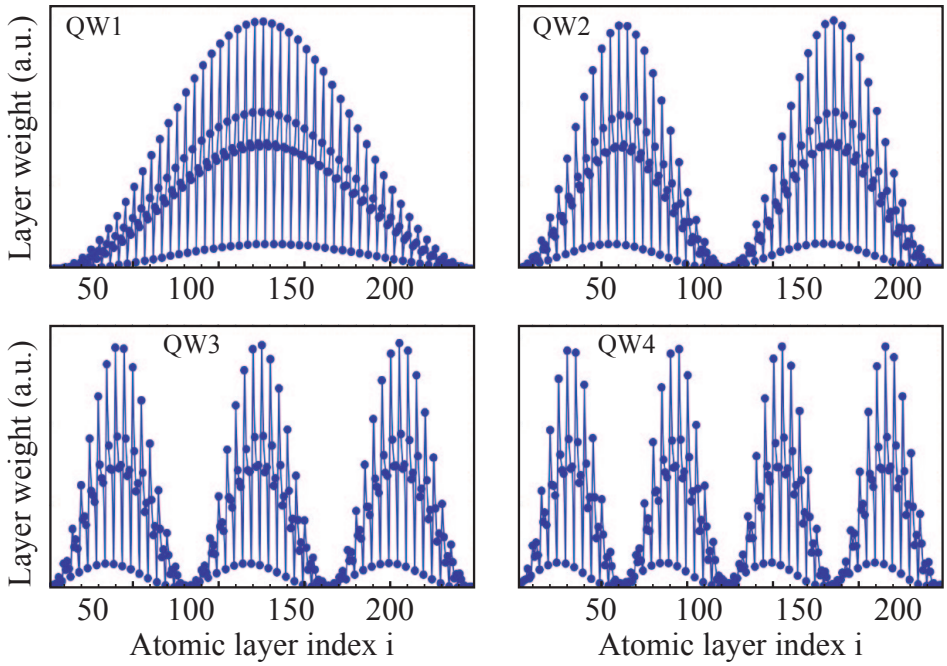

Figure 3.9: Real space distribution of quantum well (QW) states obtained from a 250-atomic-layer slab model. These four QW states shown here are from the first four conduction bands.

as the band inversion becomes stronger by further increasing the SOC values. The mechanism of the SOC-driven band inversion can be understood by analyzing the energy levels at Γ point in the bulk band structure of Bi_2Se_3 [33, 64]: SOC results in new eigenstates expressed by the total angular momentum and induces energy repulsion between these energy states. The lowest-energy conduction band is pushed down to a lower energy level with increasing SOC values, while the highest-energy valence band is pushed up to a higher energy level. Consequently, in a small SOC range, these two bands get closer and eventually touch at the Γ point with increasing SOC. If we keep increasing the value of SOC, these two bands will cross each other and reopen a gap because of the strong hybridization between them. After the bulk gap reopens, the characteristic of the bands sitting right above and

below the Fermi level, here referring to parity as described by Z_2 invariant theory [32], are inverted as compared to the zero SOC system. Now the system has also been translated from a trivial insulator to a topological insulator after the band inversion is induced by a large enough SOC.

Quantum well (QW) states also always exist for the slab model of Bi_2Se_3, as shown in Fig. 3.9. These states are characterized by the bulk electronic structure, but they have spatial distribution profiles consistent with the confined potential of a finite slab model. As will be discussed in Chapter 4, these QW states can evolve into Rashba-like states with spin splitting when an additional potential is added into the surface region.

Chapter 4

Impurities in 3D topological insulators

4.1 Rashba spin-splitting control at the surface of Bi_2Se_3

The electronic structure of Bi_2Se_3 is studied by angle-resolved photoemission and density functional theory. We show that the instability of the surface electronic properties, observed even in ultrahigh-vacuum conditions, can be overcome via in situ potassium deposition. In addition to accurately setting the carrier concentration, new Rashba-like spin-polarized states are induced, with a tunable, reversible, and highly stable spin splitting. Ab initio slab calculations reveal that these Rashba states are derived from 5-quintuple-layer quantum-well states. While the K-induced potential gradient enhances the spin splitting, this may be present on pristine surfaces due to the symmetry breaking of the vacuum-solid interface.

4.1.1 Introduction

Topological insulators, with a gapless topological surface state (TSS) located in a large bulk bandgap, define a new quantum phase of matter [7, 26, 28, 65]. Their uniqueness, and their strong application potential in quantum electronic devices, stem from the TSS combination of spin polarization and protection from backscattering [66, 67]. Bi_2Se_3 is a three dimensional topological insulator, as theoretically proposed [33] and experimentally verified by angle-resolved photoemission spectroscopy (ARPES) and other surface sensitive techniques [34, 35, 68]. Unfortunately, despite great effort in con-

trolling the Se stoichiometry and with it the bulk carrier concentration [69], unintentional and uncontrolled doping seems to lead to a bulk conductivity that masks the surface electronic properties [70].

ARPES studies also have shown that cleaved sample surfaces and subsurfaces become progressively more electron doped over time – even in ultra-high vacuum conditions – by either gas adsorption, or formation/migration of defects and vacancies [71, 72]. Lastly, the TSS might become inaccessible and/or be completely deformed through a hybridization with trivial states induced by gas molecule adsorption when exposed to air, hindering most attempts of material processing and characterization, as well as device fabrication.

Developing new approaches to stabilize and control the surface of these systems is arguably the most critical step towards the exploitation of their topological properties. Some success has been obtained in inducing electron and hole surface doping by a combination of in situ processing, such as material evaporation and radiation exposure [73, 74]. The same TSS has also been fabricated on nanoribbons, which have large surface-to-volume ratio [75]. From a different perspective, carefully doped topological insulators can provide a platform to study the interplay between TSS and bulk electron dynamics, which has important implications for TSS control and exploring topological superconductivity [76].

In this section, we present a systematic ARPES study of the evolution of the surface electronic structure of Bi_2Se_3 as a function of time and in situ potassium evaporation. The deposition of submonolayers of potassium allows us to stabilize the otherwise continually evolving surface carrier concentration. It also leads to a more uniform surface electronic structure, in which well-defined Rashba-like states emerge from the continuum of parabolic-like states that characterizes the as-cleaved, disordered surfaces. This approach provides a precise handle on the surface doping, and also allows tuning the spin splitting of the Rashba-like states. Our density functional theory (DFT) slab calculations reveal that the new spin-split states originate from the bulk-like quantum-well (QW) states of a 5-quintuple-layer (5QL) slab, as a consequence of the K-enhanced inversion symmetry breaking already

present for the pristine surface of Bi_2Se_3.

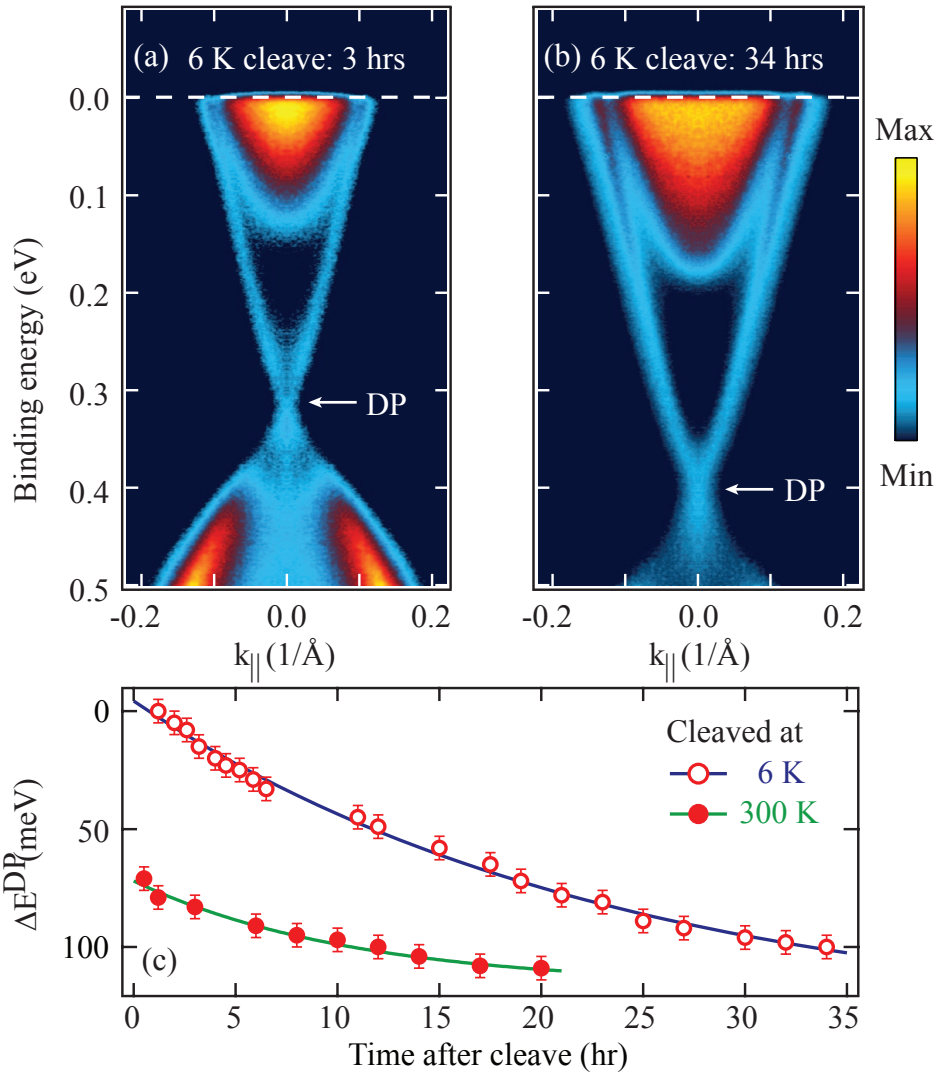

Figure 4.1: (a),(b) Time evolution of the ARPES dispersion of Bi_2Se_3 at $5{\times}10^{-11}$ torr and $T = 6\,\mathrm{K}$: (a) 3 hours after cleaving; (b) 34 hours after cleaving. (c) Exponential fit of the shift of the Dirac point (DP) binding energy position versus time for 6 and 300 K cleaves (both measured at 6 K); the fit result, $\Delta E^{DP} \propto e^{-t/\tau}$, gives a mean lifetime with $\tau = 23$ hours and $\tau = 11$ hours for the 6 and 300 K cleaves, respectively.

4.1.2 Experimental and calculation methods

ARPES measurements were performed at UBC with 21.2 eV linearly polarized photons on an ARPES spectrometer equipped with a SPECS Phoibos 150 hemispherical analyzer and UVS300 monochromatized gas discharge lamp. Energy and angular resolution were set to 10 meV and $\pm 0.1^\circ$. Bi_2Se_3 single crystals, grown from the melt (with carrier density $n \simeq 1.24 \times 10^{19}$ cm^{-3} [69]) and by floating zone, were aligned by Laue diffraction then cleaved and measured at pressures better than 5×10^{-11} torr and 6 K, unless otherwise specified. No difference was observed for samples grown with different methods. Potassium was evaporated at the sample temperature of 6 K, with a 6.2 A evaporation current for 30 second intervals [77, 78]. DFT calculations were performed using the linearized augmented-plane-wave method in the WIEN2k package [44], with structural parameters from Ref. [33]. We considered stoichiometric slabs terminated by a Se layer on both sides, representing natural cleavage planes within this material. Spin-orbit coupling (SOC) is included as a second variational step using scalar-relativistic eigenfunctions as a basis [44]; exchange and correlation effects are treated within the generalized gradient approximation [79].

4.1.3 In situ K deposition-induced Rashba-like states

The time evolution of the as-cleaved Bi_2Se_3 surface is shown in Fig.4.1. As typically observed by ARPES, and contrary to what is predicted by DFT for fully stoichiometric Bi_2Se_3 (Fig. 4.6), even immediately after a 6 K cleave the Fermi level is not in the bulk gap; instead it crosses both TSS and parabolic continuum of bulk-like states. The pronounced time dependence of the data is exemplified by the variation of the Dirac point (DP) binding energy (ΔE^{DP}), which increases from ~ 300 to 400 meV over 34 hours at 5×10^{-11} torr and 6 K [Fig. 4.1(c)]. An exponential fit of ΔE^{DP} versus time indicates that the lifetime value is 23 hours, e.g., $E^{DP} \simeq 433$ meV would be reached 46 hours after cleaving. At variance with the time dependence of the TSS, the bottom of the parabolic continuum shifts down by only 30 meV in 34 hours, which provides evidence against the pure surface nature

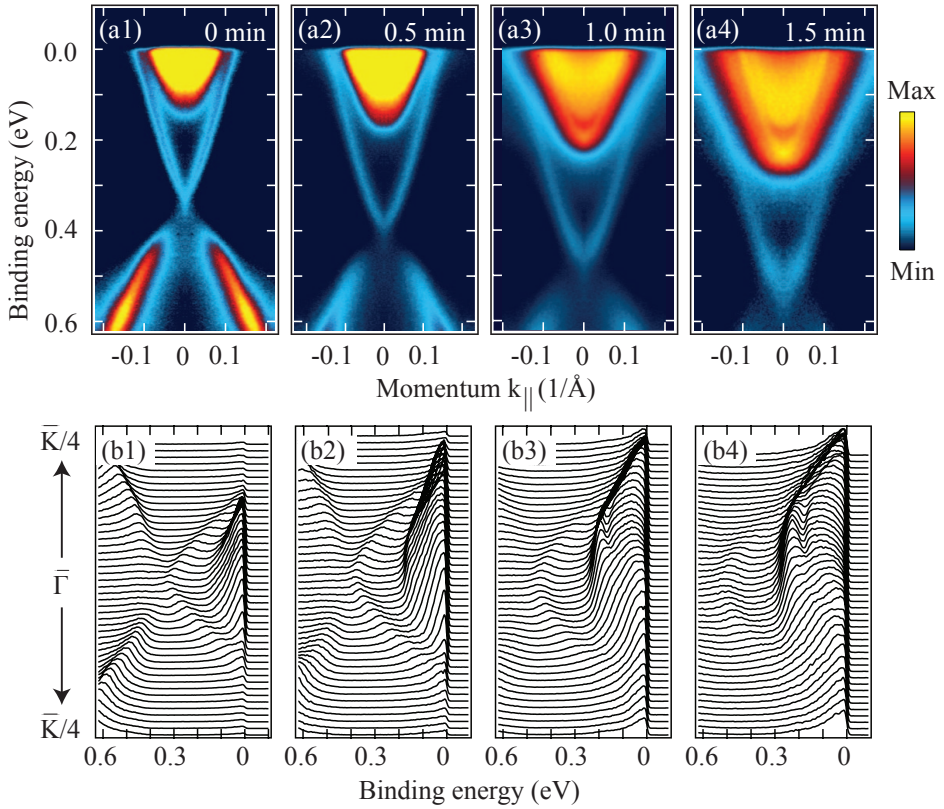

Figure 4.2: Evolution of the Bi_2Se_3 $\bar{\Gamma}-\bar{K}$ electronic dispersion with low K deposition, upon subsequent 0.5 min K-evaporation steps: (a1)–(a4) ARPES image plots, (b1)–(b4) corresponding energy distribution curves (EDCs). The sample was kept at 5×10^{-11} torr and 6 K.

of the continuum. One should note that the pristine position of DP depends also on the cleave temperature: on a sample cleaved at 300 K we found a 70 meV deeper starting position for the DP, although the saturation value is approximately the same as that of the 6 K cleave [Fig. 4.1(c)].

In our ARPES study, the surface time evolution resulted only in the deepening of Dirac cone (DC) and bulk continuum, as a consequence of the sample gaining electrons. Other effects, such as the reported appearance of a 2-dimensional electron gas, were not observed [80]. More substantial changes are induced by the in situ evaporation of potassium on the cleaved surfaces,

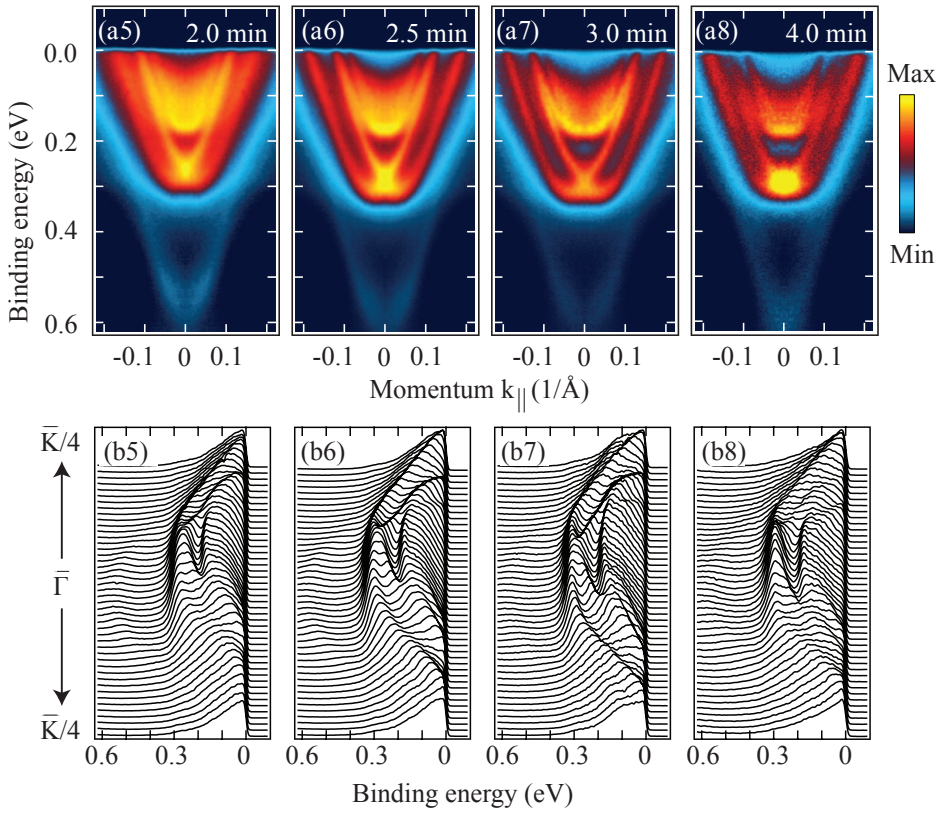

Figure 4.3: Evolution of the Bi_2Se_3 $\bar{\Gamma}$–$\bar{K}$ electronic dispersion with heavy K deposition, upon subsequent 0.5 min K-evaporation steps: (a5)–(a8) ARPES image plots, (b5)–(b8) corresponding energy distribution curves (EDCs). The sample was kept at 5×10^{-11} torr and 6 K.

also performed at 6 K to guarantee the highest stability. As a function of K-deposition time, three stages can be identified: *Stage I* – for moderate K deposition [up to 1 minute, Figs. 4.2(ab1)–(ab3)], the DP moves to higher binding energy by electron doping and a sharper parabolic state appears at the edge of the bulk continuum, reminiscent of the proposed 2DEG [80]. *Stage II*: for intermediate K deposition [from 1 to 3 minutes, Figs. 4.3(ab4)–(ab7)], the electron doping further increases and two pairs of sharp parabolic states appear, with an equal and opposite momentum-shift away from the $\bar{\Gamma}$ point, as in a Rashba type [15] splitting [these states are labelled RB1

and RB2 in Fig. 4.4(a)]. First RB1 develops from the newly formed sharp parabolic state identified in stage I, followed by RB2 which develops closer to the Fermi energy. Interestingly, the appearance of the sharp RB1 and RB2 features is accompanied by a suppression of the bulk-like continuum. This emergence of a coherent quasiparticle dispersion from a continuum of incoherent spectral weight indicates that the evaporation of potassium leads to a progressively more uniform surface and subsurface structure. *Stage III*: for heavy K deposition [beyond 3 minutes, Fig. 4.3(ab8)], the bottom of RB1 and RB2 as well as E^{DP} are not changing, indicating that the sample cannot be doped any further. The only noticeable effect is a small decrease of spin splitting for RB1 (by $0.015\,\text{Å}^{-1}$) and conversely an increase for RB2 (by $0.01\,\text{Å}^{-1}$), perhaps stemming from a change in hybridization between the two Rashba pairs. As a last remark, during the entire K-deposition process the band velocity of the TSS close to the DP is $3.2 \pm 0.3\,\text{eVÅ}$, consistent with previous reports [81].

Before analyzing quantitatively the evolution of the various states upon K deposition, we address the question of the stability of this new surface versus time and temperature cycling. In Figs. 4.4(a)–(c) we compare the ARPES data from a 3 minutes K-evaporated surface, as measured right after deposition and 30 hours later (during which the sample was kept at 6 K). Other than a smaller than 10 meV shift of the bottom of RB1 [Fig. 4.4(c)], all spectral features including the TSS have remained exactly the same over the 30 hours interval. This is a remarkable stability, especially when compared to the 365 meV shift induced by the initial K deposition [Fig. 4.4(e)], and to the more than 100 meV shift observed versus time without any active surface processing [Fig. 4.1(c)]. This approach might provide a new path to overcome the general instability and self-doping problem of the surface of Bi_2Se_3, which represents one of the major shortcomings towards the fabrication of topological devices. Temperature effects were studied by slowly warming up the sample, in which case K atoms diffuse and eventually leave the surface, reverting the material back to an earlier stage with lower K coverage. Indeed, as one can see by comparing Fig. 4.4(d) to Fig. 4.2(a4), a sample initially K evaporated for 4 minutes at 6 K, and then measured at

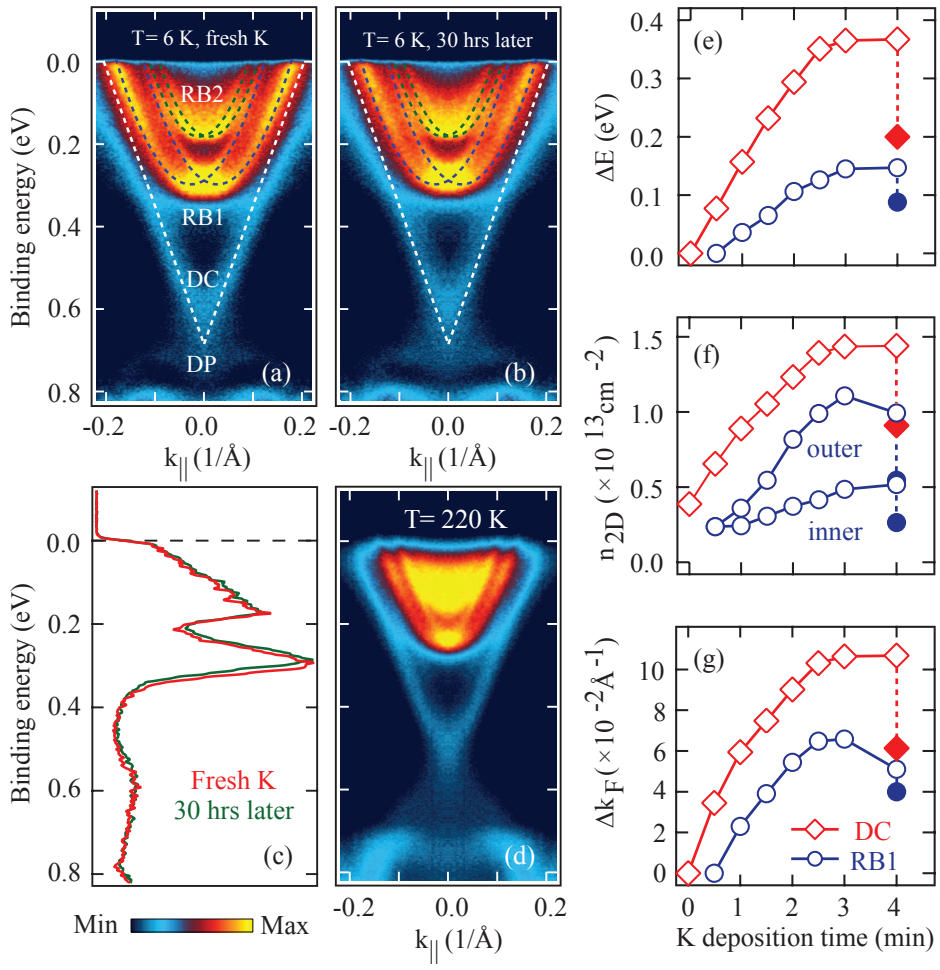

Figure 4.4: Stable and reversible band dispersions. ARPES $\bar{\Gamma}-\bar{K}$ band dispersion from Bi_2Se_3 taken (a) immediately after a 3 min K evaporation, and (b) 30 hours later (the sample was kept at 5×10^{-11} torr and 6 K the whole time). As also emphasized by the comparison of the corresponding $\bar{\Gamma}$ point EDCs in (c), the evaporated surface is highly stable. (d) Band dispersion measured at 220 K after a slow 36 hours warming up on a sample initially K evaporated for 4 min at 6 K; the comparison with the data in Fig. 4.3(a8) reveals the suppression of the K-induced carrier doping. (e-g) Evolution vs. K-evaporation time of: (e) binding energy variation for DP (ΔE^{DP}) and bottom of RB1 (ΔE^{RB1}), as defined in (a); (f) sheet carrier density for DC (n_{2D}^{DC}) and RB1 (n_{2D}^{RB1}); (g) variation of the DC Fermi wavevector (Δk_F^{DC}) and of the Rashba band splitting at E_F (Δk_F^{RB1}). Empty symbols in (e)–(g) are for $T = 6$ K and filled ones for $T = 220$ K.

220 K after a gradual 36 hours warming up, exhibits ARPES features similar to those obtained directly after a 1.5 minutes K deposition at 6 K. This implies that K deposition on Bi_2Se_3 is also reversible, making it possible to fine tune surface doping, position of the DP, and Rashba spin splitting.

We summarize in Figs. 4.4(e)–(g) the K-evaporation evolution of various parameters characterizing the $\bar{\Gamma}-\bar{K}$ dispersion of DC and Rashba states (empty symbols identify 6 K data, and the filled ones 220 K data). As evident in Fig. 4.4(e) from the variation of E^{DP} and bottom of RB1, the highest possible doping level is achieved ∼3 minutes into the K deposition, corresponding to $\Delta E^{DP} \simeq 365\,\text{meV}$ and $\Delta E^{RB1} \simeq 150\,\text{meV}$ (note that RB2 is not plotted due to its later appearance and fewer data points; after ∼3 minutes K deposition $\Delta E^{RB2} \simeq 65\,\text{meV}$). The K-induced change in surface electron density for the various states can be estimated from the relation $n_{2D} = A_{FS}/A_{BZ}\,A_{UC}$ between the area of Fermi surface, Brillouin zone, and unit cell, without accounting for spin degeneracy given that all relevant states are spin split. Because at these electron fillings all FS's are hexagonal, this reduces to $n_{2D} = k_F^2/2\sqrt{3}\pi^2$, where k_F is the Fermi wavevector along the $\bar{\Gamma}-\bar{K}$ direction of the BZ (as in Fig. 4.2 and Fig. 4.3).

After 3 minutes K evaporation the total sheet carrier density is $n_{2D}^{tot} \simeq 3.64 \times 10^{13}\,\text{cm}^{-2}$ (0.162 electron/BZ), corresponding to the sum of the contributions from DC, and inner-and-outer RB1 and RB2 (1.43, 1.60, and $0.61 \times 10^{13}\,\text{cm}^{-2}$ respectively). This value is to be compared to $n_{2D}^{tot} \simeq 3.87 \times 10^{12}\,\text{cm}^{-2}$ before K deposition (0.017 electron/BZ), which however only accounts for the DC, given the impossibility of estimating the contribution from the parabolic continuum.

As a last point, from the Δk_F data presented in Fig. 4.4(g), and the dispersion of spin-split Rashba bands:

$$E^{\pm}(k_\parallel) = E_{\bar{\Gamma}} + \frac{\hbar^2 k_\parallel^2}{2m^\star} \pm \alpha_R k_\parallel, \tag{4.1}$$

we can estimate the Rashba parameter $\alpha_R = \hbar^2 \Delta k_\parallel^{\pm}/2m^\star$ for RB1 and RB2. The latter, which depends both on the value of spin-orbit coupling (SOC) and the gradient of the potential $\partial V/\partial z$ [82], reflects the size of the spin

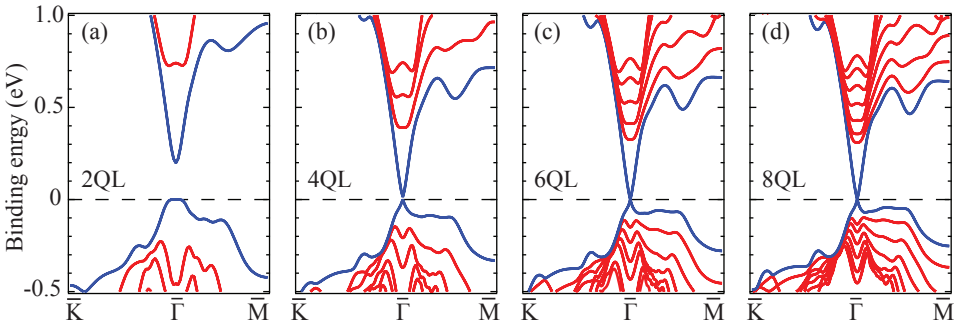

Figure 4.5: (a)–(d) Quantum well (QW) and surface slab states calculated with various thicknesses: 2QL, 4QL, 6QL, and 8QL, respectively. The QW number (shown in red) plus one surface state (shown in bule) equals to the QL number of the slab thickness.

splitting in momentum space and is here controlled directly by the amount of K deposited on the as-cleaved surfaces. The largest RB1 splitting is observed after 2.5-3 minutes K evaporation and is anisotropic: $\Delta k_F \simeq 0.066\text{Å}^{-1}$ along $\bar{\Gamma}$-$\bar{K}$, and 0.080Å^{-1} along $\bar{\Gamma}$-$\bar{M}$. The spin splitting of RB2 increases slowly during the whole K evaporation process and has an isotropic $\Delta k_F \simeq 0.02\text{Å}^{-1}$ for 3 minutes K evaporation. Fitting the Rashba-like band dispersions along $\bar{\Gamma}$-$\bar{K}$ to Eq. 4.1, for RB1 (RB2) we obtain $E_{\bar{\Gamma}} = 295 \pm 10\,\text{meV}$ (172 meV), $m^\star = 0.28 \pm 0.02 m_e$ ($0.19\,m_e$), and $\alpha_R = 0.79 \pm 0.03\,\text{eVÅ}$ (0.35 eVÅ). The value of α_R for RB1 is more than twice the Rashba splitting of the Au(111) surface state ($\alpha_R \simeq 0.33\,\text{eVÅ}$), and also larger than the one of the Bi(111) surface state ($\alpha_R \simeq 0.56\,\text{eVÅ}$) [18].

4.1.4 Quantum well states and conclusion

DFT calculations for bulk Bi_2Se_3, as well as slabs with varying number of QL's (Fig. 4.5 and Fig. 4.6), provide a detailed explanation for our observations and some interesting insights. Each QL consists of 2 Bi and 3 Se layers alternating along the c axis, with one Se layer in the middle of the QL and the other two on either side. This forms a non-polar structure with a natural cleavage plane between two adjacent Se layers belonging to dif-

ferent QL's. As shown in Fig. 4.6(b) for the particular case of a 5QL slab in addition to the TSS-DC there are 4 QW states, for a total of 5 states matching the number of QL's. As evidenced by the comparison with the fully k_z-projected bulk results in Fig. 4.6(a), where the TSS is missing due to the absence of the surface, the slab QW states exhibit the same character and energy as the Bi-Se conduction band. However, they are discrete in nature due to quantum confinement, and span a narrower energy range than the corresponding bulk bandwidth $W_B = 520\,\text{meV}$. The effective slab bandwidth W_{QL}, defined as the energy difference between top and bottom QW states, is asymptotically approaching the bulk W_B value [Fig. 4.6(c)]; for a proper correspondence with the bulk electronic structure a rather large number of QL's is needed (i.e., more than 10 QL). Interestingly, the splitting between the DP and the different QW states is extremely sensitive to the number of QL's. For 5QL we obtain 346 meV QW1-DP and 126 meV QW2-QW1 splittings [Fig. 4.6(c)], which closely match the 3 minutes K-deposition values 380±50 meV and 123±6 meV for RB1-DP and RB2-RB1, respectively [as defined from the EDC's at the $\bar{\Gamma}$ point in Fig. 4.4(a)].

This analysis leads to several important conclusions: *(i)* The RB1 and RB2 states that emerge from the parabolic continuum are of the same Bi and Se character as those obtained from bulk Bi_2Se_3 calculations in the same energy range. However, because of the observed lack of k_z dispersion [80] and the almost perfect match comparing the energy of RB1-RB2 with QW1-QW2 from 5QL slab calculations [as seen in Fig. 4.6(c)], these states should be more appropriately thought of as the quantum-confined analog of those bulk states associated with a band-bending over a 5QL subsurface region (47.7 Å). While this subsurface region is disordered on the as-cleaved surfaces (either in its depth and/or carrier concentration), which causes a continuum of states, the disorder is suppressed upon K evaporation as evidenced by the appearance of the well defined RB1 and RB2 features. *(ii)* Potassium, in addition to doping carriers, also induces a change in $\partial V/\partial z$, which in turn provides a very direct control knob on both band-bending depth and spin splitting of the Rashba states. *(iii)* In light of the extent of the subsurface band-bending region, these quantum-confined states should

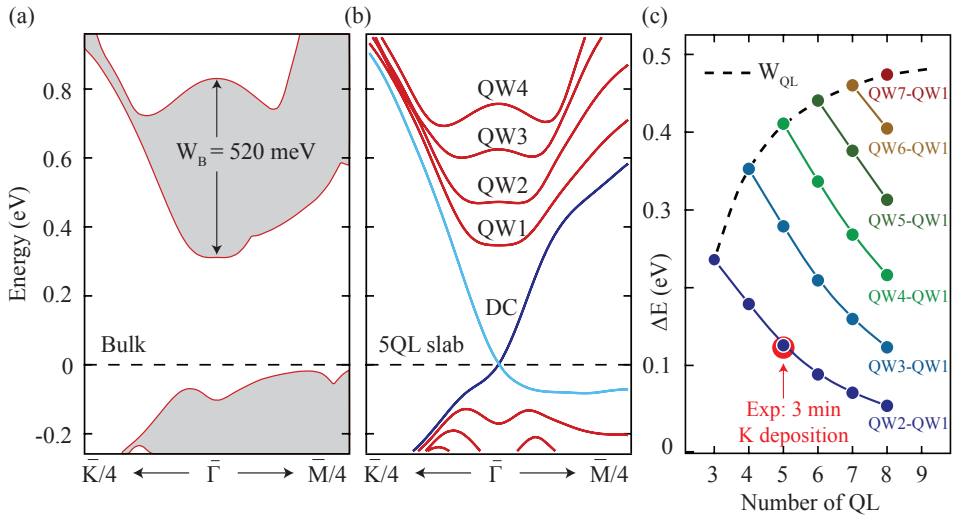

Figure 4.6: Energy splitting of quantum well (QW) states. DFT results for (a) k_z-projected bulk and (b) 5QL slab of Bi_2Se_3 (E_F is at energy 0). (c) Energy difference of the QW slab states with respect to QW1, calculated for various thicknesses. The QW number increases with QL number, defining a bandwidth W_{QL} that asymptotically approaches be fully k_z-projected bulk $W_B = 520\,\text{meV}$. The 3 minutes K-deposition RB2-RB1 splitting of $123 \pm 6\,\text{meV}$ is accurately reproduced by the 5QL results.

affect more than just surface sensitive experiments. For instance, Rashba spin-split states might have to be accounted for in the interpretation of transport data even from pristine surfaces, although with a much smaller splitting induced solely by the symmetry breaking vacuum-solid interface.

4.2 Tailoring spin-orbit coupling in Mn-doped $Bi_{2-x}Mn_xTe_3$

4.2.1 Introduction

Since topological surface states are chiral and spin-polarized, they should be immune to localization as long as the disorder potential does not violate time reversal symmetry (TRS). Breaking the TRS of the topological surface state (TSS) can lead to a gap opening at the Dirac point. More importantly, breaking the TRS is key to realizing novel physics phenomena such as the axion electrodynamics and the spin-galvanic effect [30]. In the two-dimensional topological insulator (TI) HgTe, it has been shown that a magnetic field can break the TRS and open a gap in the surface state [83]. In three-dimensional TIs, an efficient way to break TRS is to develop a long-range magnetic order by doping the system with magnetic impurities.

In the previous section, we demonstrated that one way to study impurity effects is through in situ surface doping via adsorption of impurities on pristine TI materials. Extensive studies have been conducted along this line by evaporating magnetic impurities on the surface of topological insulators [84–87]. However, none of these studies showed any indication of an opening gap at the Dirac point, which we would expect from a broken TRS induced by magnetic impurities. Success has instead been achieved using another experimental method, which is to add magnetic impurities into the sample during crystal growth, i.e., bulk doping. It has been reported that magnetic dopants break the TRS and open a gap at the Dirac point in Bi_2Se_3 [35]. Besides their relevance for controlling the TRS in the system, a dilution of the system's SOC by impurities with small SOC can give rise to new quantum phases that could be essentially important for applications of the system, such as tuning the system through a quantum phase transition from the topological to the non-topological phase [88, 89].

In this section, we focus on the doping evolution of the electronic states of $Bi_{2-x}Mn_xTe_3$ (with $x = 0$, 0.04, and 0.1, respectively). The motivation of the study is to examine how the ferromagnetic phase affects the topological

surface states, such as opening a gap at the Dirac point by breaking the TRS. Unfortunately, the Dirac point of Bi_2Te_3 is buried inside the valence band [33], resulting in an invisible Dirac point. This characteristic of the material makes it impossible to study the broken TRS by examining the presence of a gap in Bi_2Te_3. Nevertheless, we can study other effects caused by the ferromagnetic ordering and the almost zero SOC of Mn impurities. We will show that the Mn impurities can decrease the bulk band gap by diluting the effective SOC of the system. Furthermore, we show that the temperature effect on the width of momentum distribution curves (MDCs) indicates the possibility of ferromagnetic domain formation, albeit with a short range at temperatures below 12 K.

4.2.2 Material properties

The Mn-doped Bi_2Te_3 samples used in our study were grown by R.J. Cava's group at Princeton University. The Mn concentration was analytically determined by doing elemental analysis, and samples with $x = 0$, 0.04, and 0.1 were used for our ARPES study. The temperature-dependent magnetic susceptibilities measured in an applied field of 1 kOe showed a ferromagnetic transition for $x \geq 0.04$ at $T \leq 12\,\mathrm{K}$. The ordered ferromagnetic moment can reach a magnitude of $\sim 4\mu_B$ per mol-Mn, with the c axis as an easy axis of magnetization. STM topographic images of the in situ cleaved surface of $Bi_{1.91}Mn_{0.09}Te_3$ did not show Mn clusters and indicated that the system as a true dilute ferromagnetic semiconductor [90]. X-ray absorption spectra (XAS) on the Mn $L_{2,3}$ edge suggested a 2+ valence state for the Mn impurities, in contrast to the 3+ of Bi atoms in Bi_2Te_3 [91]. This means that Mn impurities will lead to holes in the crystal and make the system hole-doped. The local density of states measured by STM showed a 150 meV upward shift in chemical potential that is consistent with the p-type character of the Mn dopants [90].

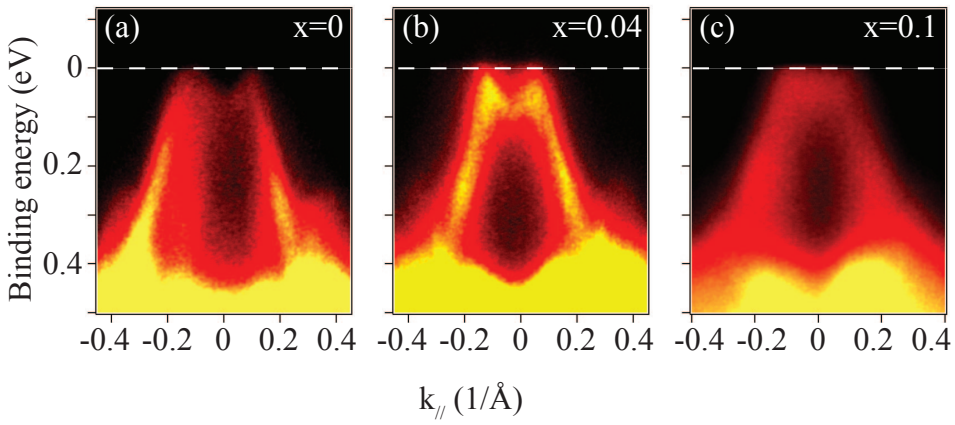

Figure 4.7: (a)–(c) ARPES dispersions measured at 6 K with freshly cleaved samples of $Bi_{2-x}Mn_xTe_3$: $x = 0$ (a), 0.04 (b), and 0.1 (c).

4.2.3 Doping-level-dependent ARPES spectra

We performed ARPES measurements on $Bi_{2-x}Mn_xTe_3$ crystals with $x = 0$, 0.04, and 0.1, respectively. The samples were cleaved at low temperature, $T = 6$ K, with a pressure lower than 5×10^{-11} torr. The orientations of the samples were checked by Laue diffraction peaks and were aligned in the Γ to K direction parallel to the entrance slit of the electronic analyzer.

In Fig. 4.7, we show ARPES dispersions measured with in situ freshly cleaved samples. The Fermi levels of all three samples (indicated by white dashed lines) cross the valence band below the Dirac point. This p-type character of Bi_2Te_3 samples is in contrast to the n-type Bi_2Se_3 samples, which always have a Fermi level crossing the bulk conduction bands, as shown in Fig. 4.1. However, the as-cleaved surface of both systems, Bi_2Te_3 and Bi_2Se_3, has the same instabilities from becoming progressively electron-doped, as seen from the dynamics of the electronic states for Bi_2Te_3 in Ref.[72] and for Bi_2Se_3 in Fig. 4.1. Because of the surface instability, it is difficult to identify the Mn impurities as hole dopants simply by comparing the Fermi level positions.

After about 18 hours of sample cleavage and with the assistance of a small amount of potassium deposition on the sample surface, we were able

to lower the topological surface state to cross the Fermi level, as shown in Fig. 4.8. The surface state remained in both the pure and the Mn-doped Bi_2Te_3. No noticeable changes were observed by comparing the ARPES spectra Figs. 4.8 (a) to (c) and (d) to (f). First-principles model calculations suggested that the dispersion of the surface state should depend considerably on the Mn magnetization. With magnetization of Mn either along the *c*-axis or in the *ab*-plane, the dispersion will become more linear, as shown by DFT calculations in Ref. [92]. We attempted to fit the ARPES spectra by using the surface band dispersion, taking into account the hexagonal warping effect as proposed by Fu [93]. The fitting results may suggest that the warping term was indeed suppressed by increasing the Mn concentrations, meaning a better linear dispersion at a higher Mn doping level (results are not shown here). However, the fitting results are extremely sensitive to the fitting procedures, such as the choice of fitting energy window and the estimation of the Dirac point position. All these parameters can bring large uncertainty to the fitting results and thus lead to an inconclusive outcome.

By comparing Figs. 4.8 (a) to (c) or (d) to (f), we learned that a visible change in the electronic dispersion induced by Mn impurities is the doping level dependence of the bulk energy gap size. Based on the EDC profile at $\bar{\Gamma}$ point, we define the bulk energy gap size by measuring the energy distance between the Dirac point[4] and the bottom of the bulk conduction band. For pure Bi_2Te_3, we obtained a gap of $\Delta = 300\pm5$ meV. For Mn-doped samples, $\Delta = 260\pm10$ meV for $x = 0.04$ and $\Delta = 200\pm20$ meV for $x = 0.1$. The decrease in the bulk gap in Mn-doped Bi_2Te_3 can be also seen through the constant energy contours (CECs). In Fig. 4.9, we plot CECs cutting through four different energy levels with reference to the Dirac point. It is clear that up to 0.25 eV above the Dirac point, the bulk conduction band still did not appear in the CECs for pure samples; however, it appeared in the CECs of the Mn-doped samples as a nondispersive feature with high-intensity around the Γ point.

In TIs, the bulk energy gap size is directly related to the strength of the

[4]The Dirac point position is estimated by assuming that the surface bands are linearly dispersed near the maxima valence band and will cross each other at the Dirac point.

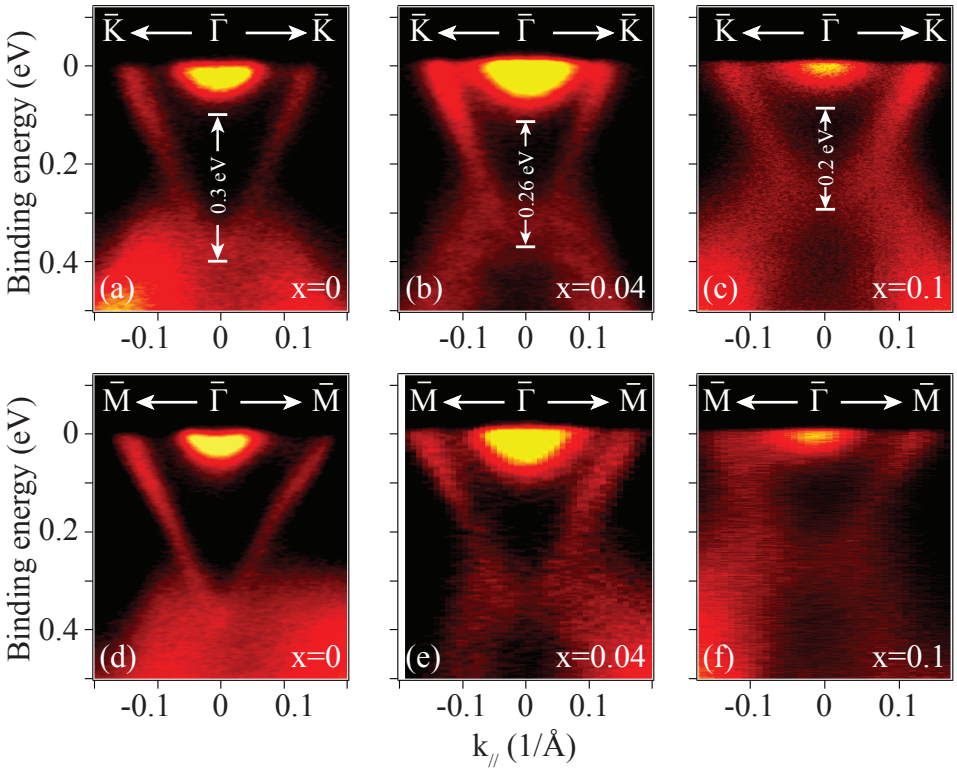

Figure 4.8: (a)–(c) Doping-level-dependent ARPES spectra of $Bi_{2-x}Mn_xTe_3$, measured along $\bar{\Gamma} \rightarrow \bar{K}$ with $x = 0$, 0.04, and 0.1, respectively. (d)–(f) Similar data but measured along $\bar{\Gamma} \rightarrow \bar{M}$. The bulk energy gap size of Mn-doped Bi_2Te_3 is labeled in (a)–(c) and has a value 0.3 eV ($x = 0$), 0.26 eV ($x = 0.04$), and 0.2 eV ($x = 0.1$), respectively.

SOC of the systems. As shown in Fig. 3.8 in Section 3.2, band inversion leads first to closing the gap and then to reopening it as the SOC of the system increases. We quantitatively tracked the gap size as a function of the SOC strength from our ab initio tight-binding model described in Chapter 3, and obtained a relationship between the bulk energy gap size Δ and the strength of the SOC λ after the surface state appears, written as:

$$\Delta = 0.33\lambda - 0.18 \text{ (Unit: eV)}. \tag{4.2}$$

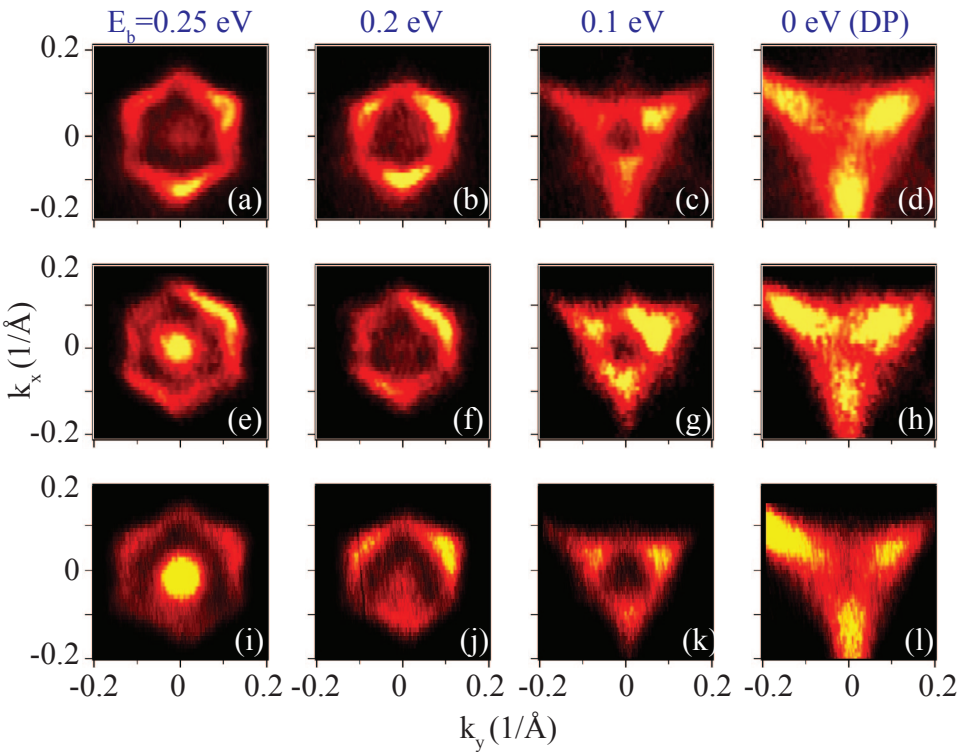

Figure 4.9: (a)–(c) Constant energy contours of $Bi_{2-x}Mn_xTe_3$ with $x = 0$ (a)–(d), $x = 0.04$ (e)–(h), and $x = 0.1$ (i)–(l). Here the zero binding energy is set at the Dirac point (DP) for convenience.

Note that this relationship is obtained from the Bi_2Se_3 model. Bi_2Te_3 differs from Bi_2Se_3 mainly due to the higher SOC in Te atoms (0.49 eV) compared to Se atoms (0.22 eV). However, Bi atoms have much larger SOC at 1.25 eV, so the total SOC of the system will mainly depend on the Bi atoms [59]. Therefore, it is still useful to compare the experimental data to this linear relationship with a ratio of 0.33 between between the gap size and the strength of the SOC. Taking the sample with $x = 0.1$ as an example, we can approximate the SOC of Mn to be zero, and thus a 5% Mn substitution of Bi could result in a 62.5 meV reduction in SOC. Naively, the bulk energy gap size would decrease only by 21 meV if we made the estimate based on Eq. 4.2. However, we obtained a 100 meV reduction from ARPES data. Therefore,

the disparity between theoretical prediction and experimental observation indicates that although the Mn concentration is low (only 2–5%), the effective content of the impurity can be at least four times higher, which is actually similar to what has been reported for Bi-induced large relativistic correction in $GaAs_{1-x}Bi_x$ semiconductors [94]. More importantly, when the SOC of the system is diluted, the impurities can turn the topological system into a trivial insulator even at low concentrations.

4.2.4 Temperature effects on ARPES spectra

Magnetic susceptibility measurements showed a development of ferromagnetism in Mn-doped Bi_2Te_3 at temperatures below 12 K [90]. Therefore, Mn-doped Bi_2Te_3 is expected to have broken TRS at T $\leq$12 K. The broken TRS may affect the topological protection and could potentially open a gap at the Dirac point of the topological surface band. Extensive studies have been carried out to look for an open gap in topological surface bands using magnetic impurities through either bulk magnetic doping in crystals and thin films [35, 95, 96] or in situ surface doping adsorption of impurities on pristine TI materials [84–86]. Most of these efforts focused on Bi_2Se_3 crystals, because there is a well-defined Dirac point in the surface bands. However, for Bi_2Te_3 the low-energy region of the surface band is buried inside the bulk valence bands, making it difficult to identify a clear Dirac point. Nevertheless, Mn impurities will always introduce disorder into the system, which could enhance the scattering rate of the TSS. How magnetic impurities affect the scattering channels for the TSS has so far only been studied through the adsorption of various magnetic impurities on the surface of topological insulators [85]. For bulk magnetic impurities-doped systems, this question has not been studied yet. Here we study the scattering rate of the TSS of Mn-doped Bi_2Te_3 by looking at the width change in the momentum distribution curve (MDC) above and below the ferromagnetic transition temperature $T_c = 12$ K.

As we discussed in Section 4.2.3, the as-cleaved sample has a Dirac surface state above the Fermi level. The instability of the sample surface

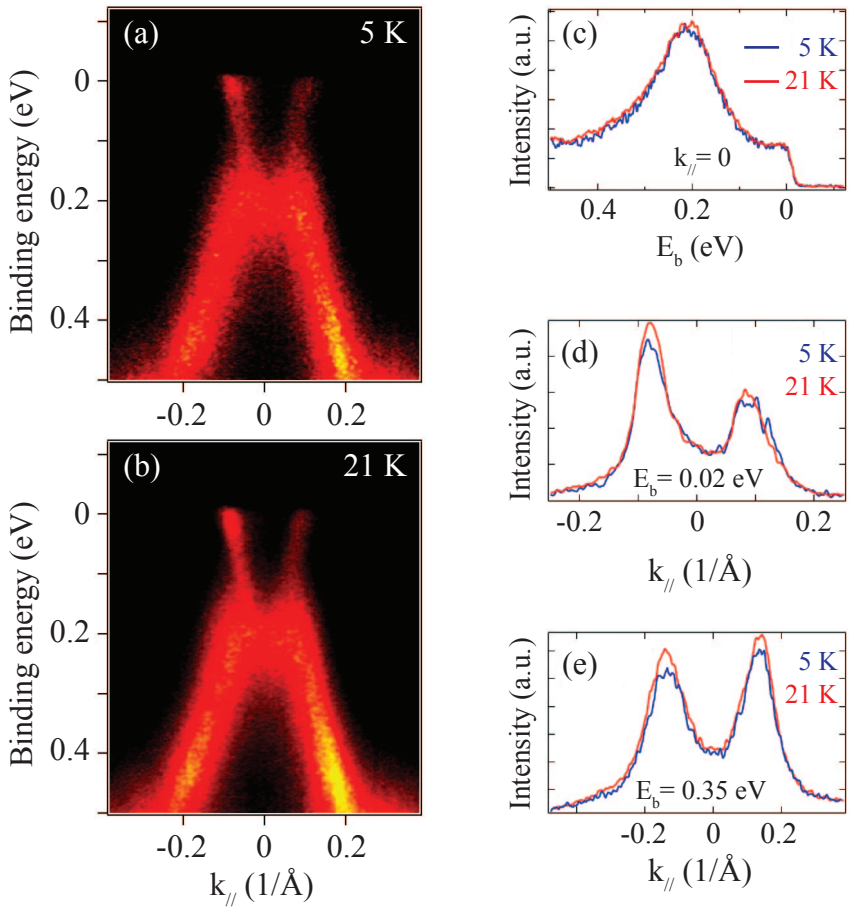

Figure 4.10: (a), (b) ARPES dispersions of $Bi_{1.96}Mn_{0.04}Te_3$, measured below (5 K) and above (21 K) T_c. The ferromagnetic transition temperature T_c is 12 K [90]. (c) EDCs at the $\bar{\Gamma}$ point, measured at 5 K and 21 K. (d), (e) MDCs above and below the Dirac point, measured at 5 K and 21 K.

can progressively electron dope the system either by absorbing residual gas molecules or by diffusing Te vacancies. The uncontrolled electron doping moves the Fermi level towards the bulk conduction band, and allows us to access the TSS in ARPES after keeping the cleaved sample in an ultra-high vacuum for a certain period without degradation. Fig. 4.10 and Fig. 4.11 show the ARPES spectra obtained 38 hours later after the sample cleavage

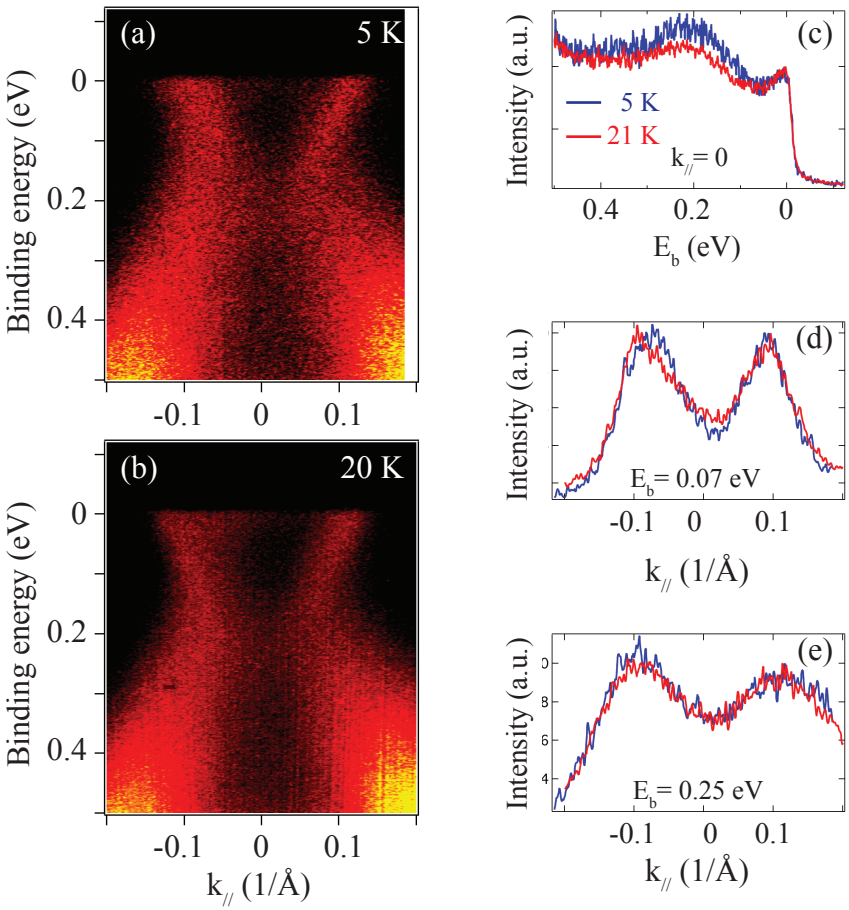

Figure 4.11: (a), (b) ARPES dispersions of $Bi_{1.9}Mn_{0.1}Te_3$, measured below and above T_c. The ferromagnetic transition temperature T_c is 12 K [90]. (c) EDCs at the Γ point, measured at 5 K and 21 K. (d), (e) MDCs above and below the Dirac point, measured at 5 K and 21 K.

of $Bi_{2-x}Mn_xTe_3$ with $x = 0.04$ and 0.1, respectively. The Fermi level has been shifted upwards by about 200 meV, and the linearly dispersed TSS can be clearly observed (comparing Figs. 4.10 and 4.11 to Fig. 4.7). To examine the response of electronic structures to the ferromagnetic transition, we compare the ARPES spectra in terms of dispersion maps, EDC and MDC profiles that were measured at $T = 5$ K (below T_c) and $T =$ 21 K (above

T_c). The comparisons indicated subtle changes at temperatures below and above T_c, in particular for the MDC profiles. To quantitatively identify the changes, we will show the temperature dependence of the MDC width by fitting the MDCs with a Voigt profile, which is a convolution of Lorentz and Gaussian profiles.

Generally, there are three scenarios that we would expect for the temperature dependence of MDC width: *case I*, if the scattering is mainly due to the electron-phonon interaction, the MDC width should become narrower with lower temperatures; *case II*, since the Mn-doped Bi_2Te_3 has a ferromagnetic ordering formed below T_c, if this ferromagnetic ordering is of long range, the scattering between electrons and disordered impurities could be suppressed and the MDC width would also become smaller at temperatures below T_c; and *case III*, if the ferromagnetic ordering is a local ordering with short range, then perturbation of impurities to the system could become stronger due to the development of disordered ferromagnetic domains, similar to the local antiferromagnetic ordering induced by Mn impurities in $Sr_3Ru_2O_7$ [97]. In this case, the disorder of local domains would enhance the scattering rate and result in a wider MDC width. In addition, if the local magnetic field broke the TRS, the ferromagnetic transition would open new scattering channels by destroying the chiral spin texture of the TSS; then we would expect broader MDCs at $T \leq T_c$, and the scattering rate could monotonically increase with increasing Mn concentration.

Firstly, we look at the doping level dependence of MDC widths for freshly cleaved samples. As shown in Fig. 4.12. the MDC width of the bulk valence band is plotted as a function of binding energy for $x = 0$, 0.04, and 0.1. We see that the MDC width becomes larger as the Mn doping level increases, indicating a more disordered system for a higher Mn concentration. By fitting the dispersions near the Fermi level that were shown in Figs. 4.10(a), (b) and Figs. 4.11 (a), (b), we obtained the MDC width of the TSS for 2% and 5% Mn-doped Bi_2Te_3, respectively. The fitting results from the right-hand-side branch of the TSS are plotted in Fig. 4.13. For $x = 0.04$, the MDC width at $T = 5\,\mathrm{K}$ is clearly larger than at 22 K and 32 K. However, if we compare the MDC width at two temperatures (22 K and 32 K) that

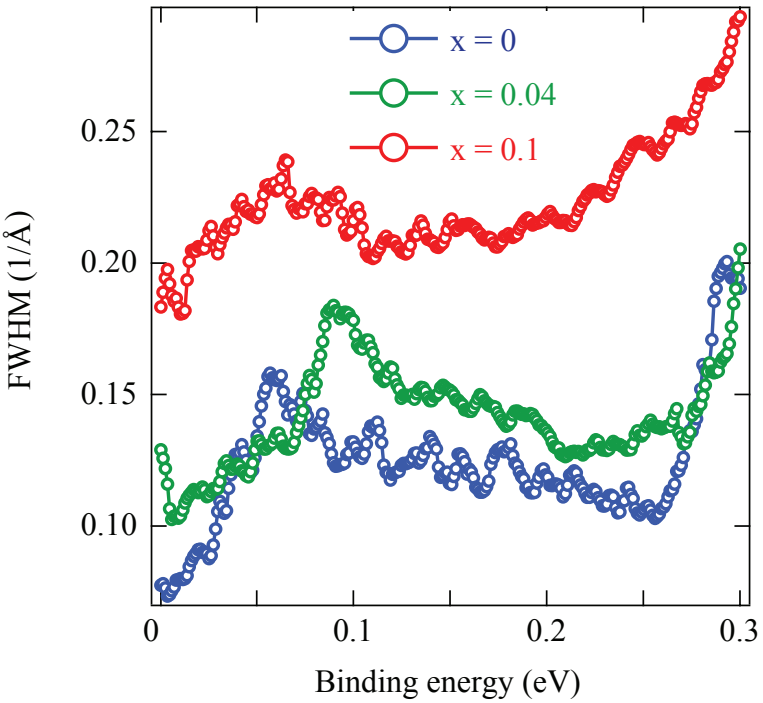

Figure 4.12: Doping-level-dependent MDC width of $Bi_{2-x}Mn_xTe_3$, measured at 6 K. The MDC width was obtained by fitting the data shown in Fig. 4.7.

are both higher than T_c, the difference is rather small. These results were replicable and were independent of the temperature history. A temperature cycle was performed by cooling down and then warming up the crystals; as shown in Fig. 4.13(a), we obtained almost overlapping data points for the same temperatures (5 K or 22 K) but measured during different temperature cycles.

The increase of MDC width at temperatures below T_c can be attributed to either the development of local ferromagnetic ordering or the broken TRS. As described earlier, if the enhancement of scattering rate at temperatures below T_c was predominantly due to the broken TRS, we would expect to observe a monotonic increase in MDC width with increasing Mn concentration at $T \leq T_c$. However, the difference in MDC width for $x = 0.1$ above

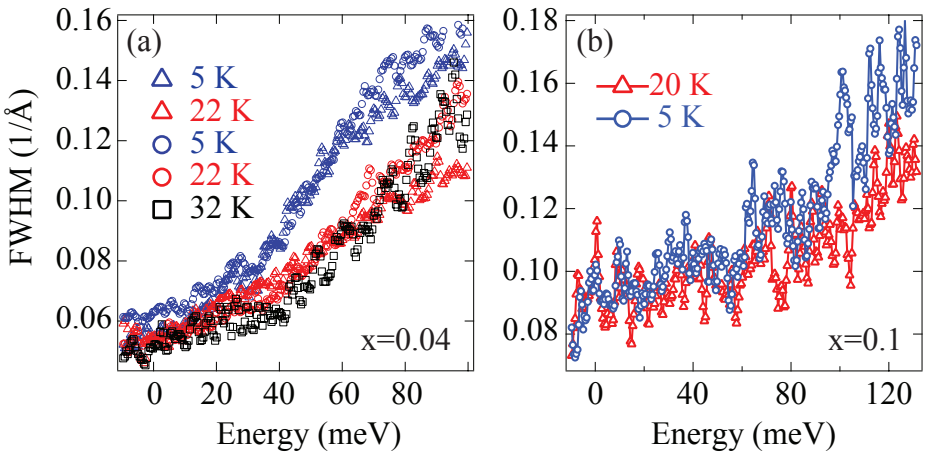

Figure 4.13: (a, b) Temperature-dependent MDC width of $Bi_{2-x}Mn_xTe_3$ with $x = 0.04$ (a) and 0.1 (b). The width of the MDC is obtained by fitting the data shown in Fig. 4.10 and Fig. 4.11. For the $x = 0.04$ sample, a temperature cycle measurement was performed, shown by two data sets in the same color.

and below T_c [Fig. 4.13(b)] is rather small compared to that for $x = 0.04$ [Fig. 4.13(a)], meaning that there is a weakly broken TRS effect on the scattering rate; on the other hand, if the enhanced scattering rate is mainly due to the onset of local ferromagnetic ordering, then the smaller change in MDC width at higher Mn doping levels can be understood by considering that with increasing Mn concentration, the system will start to form long-range ferromagnetic ordering, and therefore the effect of disordered domains with short-range ordering will be suppressed. In conclusion, (i) the subtle temperature- and doping-level-dependence of MDC width might suggest that the ferromagnetic phase induced by Mn impurities enhanced the scattering of the TSS by forming disordered domains and (ii) the evidence for broken TRS is not clear in Mn-doped Bi_2Te_3.

4.2.5 K deposition at the surface of $Bi_{1.96}Mn_{0.04}Te_3$

In Section 4.1, we described work involving in situ K deposition on Bi_2Se_3. Here we use the same experimental method but apply it to 2% Mn-doped

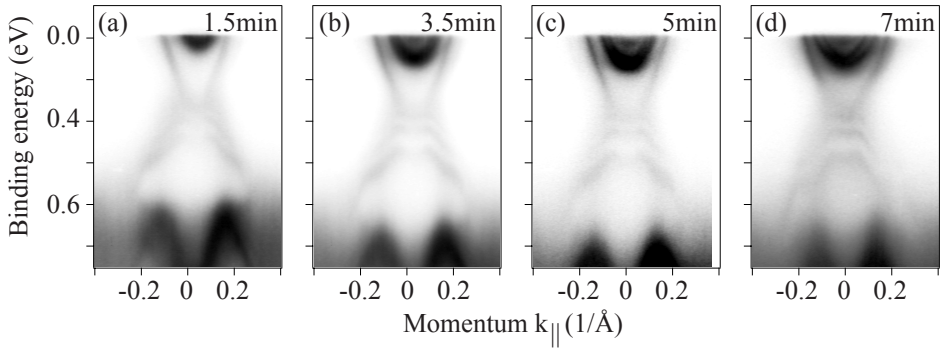

Figure 4.14: (a)–(d) Evolution of ARPES dispersions of $Bi_{1.96}Mn_{0.04}Te_3$ along $\bar{\Gamma}-\bar{K}$ as a function of K deposition time. Potassium was deposited on the sample at 21 K.

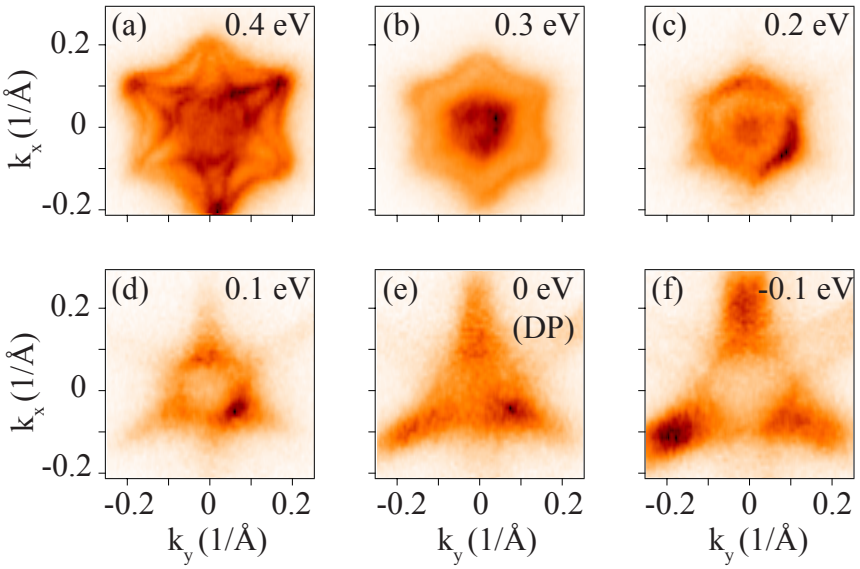

Figure 4.15: (a)–(f) ARPES constant energy contours of $Bi_{1.96}Mn_{0.04}Te_3$ after seven minutes of K deposition. The cutting energies refer to the Dirac point.

Bi_2Te_3. The purpose of this section is to demonstrate that potassium deposition on Bi_2Te_3 can also induce Rashba-like QW states with spin splitting.

Fig. 4.14 shows the ARPES dispersions measured after varying the K de-

position time. The modification of the surface electronic structure is similar to what we have discussed in Section 4.1.3. Quantizations of both the bulk conduction band and the valence band states are observable after 1.5 minutes of K deposition. The valence band evolves into QW states, presenting a set of bands with an M shape. The bulk conduction band lacked dispersion and now becomes quantized by forming pairs of parabolic bands with spin splitting, which are QW states with Rashba-like spin splitting.

Previous DFT calculations and a photon-energy-dependent ARPES study of Bi_2Te_3 [98] have indicated that the bulk states showed triangular CECs because of the crystal lattice symmetry, and the surface states gave hexagonal CECs due to the warping effect [93]. In Fig. 4.15, we show the evolution of CECs as they move away from the Dirac point and reveal the binding-energy-dependent bulk and surface character of the bands. Near the Dirac point, the surface states are degenerate with the bulk valence band states and therefore we observe triangular CECs. The surface states appear alone at 0.1 eV above the DP, with hexagonal CECs. The CECs at high energy (i.e., 0.4 eV above DP) again show the coexistence of surface states (outside contour) and bulk featured states (inner contour), which are spin-splitting QW states here. The last point to emphasize is that since the Rashba-like spin-split states are from QW states with bulk features, the CECs of these states have a triangular star shape rather than a hexagonal or circular shape, although their band dispersion looks like a two-dimensional (2D) electron gas with parabolic dispersions, as shown in Fig. 4.14(d) and Fig. 4.15(a).

4.2.6 Conclusion

In this section, we used ARPES to study the electronic structures of Mn-doped Bi_2Te_3 with different doping levels, as well as below and above the ferromagnetic transition temperature $T_c = 12$ K. A notable effect of Mn impurities is the dilution of the system's SOC, evidenced by the decrease in the bulk energy gap size with increasing Mn concentrations. Our analysis showed that the effective doping level can be four times higher than the physical Mn concentrations in the crystals. This suggested that a quantum

phase transition from non-trivial topological to trivial topological insulators can be induced by impurities even at low concentrations ($\leq 5\%$); similar phenomena have also been observed in $(Bi_{1-x}In_x)_2Se_3$ [99]. A further theoretical investigation about impurity-induced topological phase transition is required and would have a fundamental impact on topologically tunable physics and devices. The wider MDC width at lower temperatures may suggest an onset of local ferromagnetic ordering at $T \leq 12\,\mathrm{K}$. The evidence of broken TRS due to ferromagnetic ordering is not conclusive from this study, and could be further investigated by performing fine temperature-dependent ARPES and SARPES.

Chapter 5

Layer-by-layer entangled spin-orbital texture in Bi_2Se_3

With their spin-helical metallic surface state, topological insulators define a new class of materials with strong application potential in spintronics. Technological exploitation depends on the degree of spin polarization of the topological surface state (TSS), assumed to be 100% in phenomenological models. Yet in Bi_2Se_3, an archetypical topological insulator material, spin- and angle-resolved photoemission spectroscopy (SARPES) detects a spin polarization ranging from 20 to 85%, a striking discrepancy which undermines the applicability of real topological insulators. Here we show – studying Bi_2Se_3 by polarization-dependent ARPES and density-functional theory slab calculations – that the TSS Dirac fermions are characterized by a layer-dependent entangled spin-orbital texture, which becomes apparent through quantum interference effects. This explicitly solves the puzzle of the TSS spin polarization in SARPES, and suggests how 100% spin polarization of photoelectrons and photocurrents can be achieved and manipulated in topological-insulator-based devices by using linearly polarized light.

5.1 Introduction

Topological insulators (TIs) define a new state of matter in which strong spin-orbit coupling (SOC) leads to the emergence of a metallic topological surface state (TSS) formed by spin-nondegenerate Dirac fermions [7, 24–28]. To capture the physics of TIs, a spin-momentum locking with 100% spin polarization is usually assumed for the TSS in time-reversal invariant models [26–28]. A fully spin-polarized TSS has tantalizing properties, such

as robust edge modes and exotic quasiparticle excitations, making TIs good candidates for spintronic applications [30]; and also a playground for engineering Majorana fermions, and exploiting their non-Abelian statistics in topological quantum computation [31]. The successful realization of topological insulating behavior in quantum wells [66, 83] and crystalline materials [33–35] brings us closer to the practical implementation of theoretical concepts built upon novel topological properties.

To this end, the fundamental question is that of the effective spin-polarization of the TSS Dirac fermions in real materials and devices, i.e., how realistic is the hypothesis of a 100% spin polarization. The large discrepancy in the degree of TSS spin polarization determined for Bi_2Se_3 by SARPES – ranging from 20 to 85% [73, 88, 100–102] – highlights the complexity of real TIs. First principle density-functional theory (DFT) calculations indicate that the TSS spin polarization in members of the Bi_2X_3 material family ($X =$ Se, Te) can be substantially reduced from 100% [103, 104]. In addition, based on general symmetry arguments, it was shown that the spin polarization direction of photoelectrons in SARPES can be very different from that of the TSS wave function [105]. However, the role played by the intrinsic properties of the TSS wave function in defining the highest spin polarization that could be achieved, for instance in d.c. and photoinduced electrical currents, has remained elusive.

We report here that the TSS many-layer-deep extension into the material's bulk – in concert with strong SOC – gives rise to a layer-dependent, entangled spin-orbital texture of the Dirac fermions at the surface of Bi_2Se_3. This enables the precise control of both in- and out-of-plane spin polarization of the photocurrent in SARPES – all the way from 0 to $\pm 100\%$ – by varying energy, polarization, and angle of incidence of the incoming photons. More generally, the layer-by-layer variation in spin-orbital entanglement is of fundamental importance to spintronic studies and applications, whose outcome will depend critically on how one couples to the TSS. A remarkable consequence, which we will specifically exploit in this study, is that one can gain exquisite sensitivity to the internal structure of the TSS wave function, Ψ_{TSS}, via quantum interference effects using ARPES. In partic-

ular, the spin-orbital texture is captured directly in the linear-polarization dependence of the ARPES intensity maps in momentum space, and can be fully resolved with the aid of ab initio DFT slab-calculations.

5.2 Polarization-dependent ARPES intensity pattern

Let us start our discussion from the Bi_2Se_3 ARPES results in Fig. 5.1, measured with σ and π linearly-polarized 21.2 eV photons. Based on our experimental geometry [Fig. 5.1(a)] and the photoemission selection rules, σ-polarized light probes mainly the in-plane p_x and p_y orbitals, whereas π-polarized light a combination of both in-plane and out-of plane (p_z) orbitals: the observed 80% reduction in overall intensity by switching from π- to σ-polarization indicates that the TSS has a dominant p_z orbital character. As for the evolution of the ARPES intensity around the Dirac cone, in σ-polarization [Figs. 5.2(a)–(c)] we observe a twofold pattern at both 0.1 and 0.2 eV above the Dirac point (DP), consistent with a previous report [106], although somewhat asymmetric with respect to the $k_y = 0$ plane [see in particular Fig. 5.2(c)]; this suggests a tangential alignment of the in-plane $p_{x,y}$ orbitals with respect to the Dirac constant-energy contours. Conversely in π-polarization [Figs. 5.2(d)–(f)] we observe a strongly asymmetric pattern at 0.1 eV above the DP, which evolves into a triangular pattern while still retaining some asymmetry at 0.2 eV; this is in stark contrast with the uniform distribution of intensity along the Dirac contour expected for the dominant out-of-plane p_z orbitals. Finally, at -0.1 eV below the DP, a triangular pattern is observed for both polarizations [see insets of Figs. 5.2(a) and (d)].

The asymmetry in ARPES intensity between $\pm\mathbf{k}_{\parallel}$ is particularly evident in π-polarization at 0.1 eV in Fig. 5.2(d) and in the band dispersion of Fig. 5.1(b). This finding, which might seem in conflict with the time-reversal invariance of the TSS, provides fundamental clues on the structure of Ψ_{TSS}. Time-reversal invariance requires the state at $+\mathbf{k}$ with (pseudo)

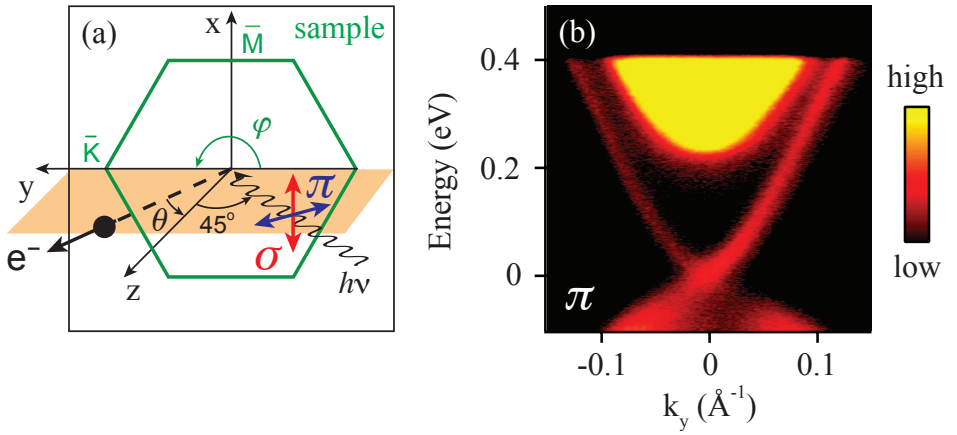

Figure 5.1: ARPES experimental geometry with linearly polarized light. (a) Schematics of the experimental geometry, with π (horizontal) and σ (vertical) linear polarizations, and horizontal photoelectron emission plane. (b) ARPES dispersion measured along $\bar{K}-\bar{\Gamma}-\bar{K}$ with π polarization; the zero of energy has been set at the Dirac point (DP) for convenience.

spin up to be degenerate with the state at $-\mathbf{k}$ with (pseudo) spin down, i.e., to have the same real-orbital occupation numbers. This so-called Kramers degeneracy, together with the ARPES selection rules for linearly polarized light, forbids intensity patterns which are different at $\pm\mathbf{k}$. We emphasize here that this restriction can be rephrased in terms of purely in-plane momentum coordinates, i.e., $\pm\mathbf{k}_{\parallel}$, only for a perfect 2-dimensional TSS with a delta-function-like density, for which k_z plays no role. Thus the observation of an imbalance in ARPES intensity at $\pm\mathbf{k}_{\parallel}$, together with the established time-reversal invariance of TIs, necessarily implies that Ψ_{TSS} must have a finite extent – albeit not a dispersion [80] – along the third dimension. While details will become clear when discussing our DFT results in Fig. 5.4 and Fig. 5.5, we anticipate that this – together with the strong SOC – leads to a complex layer-dependent spin-orbital entanglement in Bi_2Se_3, which becomes apparent in ARPES through photoelectron interference effects.

By performing ARPES intensity calculations [107][5] for TSS and bulk

[5]Details of the ARPES calculations can be found in Section 5.6.2.

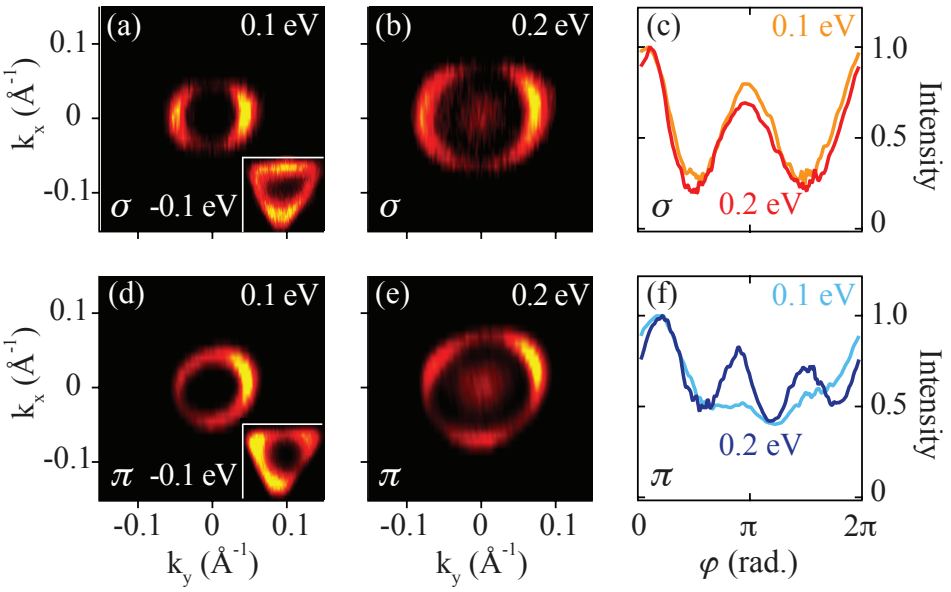

Figure 5.2: Linear polarization dependence of the measured ARPES intensity in momentum space. (a), (b) Constant energy ARPES maps from above (0.1 and 0.2 eV) and below (-0.1 eV, inset) the DP, measured with σ polarization; (d), (e) same for π polarization. (c), (f) Normalized variation of the σ- (c) and π-polarization (f) ARPES intensity, along the Dirac contours, plotted as a function of the in-plane angle φ.

wave functions from our DFT slab-calculations, we accurately reproduce the data[6]. As shown in Figs. 5.3(a)–(f), we obtain very different intensities at $\pm\mathbf{k}_{\|}$ in excellent agreement with the results for both σ and π polarizations. Specifically, we reproduce the quasi-twofold pattern in σ polarization, stemming from the spatial configuration of $p_{x,y}$ orbitals [Figs. 5.3(a) and (b)]; the quasi-threefold pattern away from the DP [Fig. 5.3(e)], which originates from the hybridization between TSS and bulk states [108][7]; and also the triangular patterns at -0.1 eV [insets of Figs. 5.3(a) and (d)]. Note

[6]Note that the TSS calculations have actually been performed for 0.12 and 0.23 eV, in order to account for the DP–conduction-band gap renormalization observed between experiment (∼260 meV) and DFT (300 meV).

[7]Note that the threefold pattern is associated with the k_z dispersion of valence- and conduction-band bulk states.

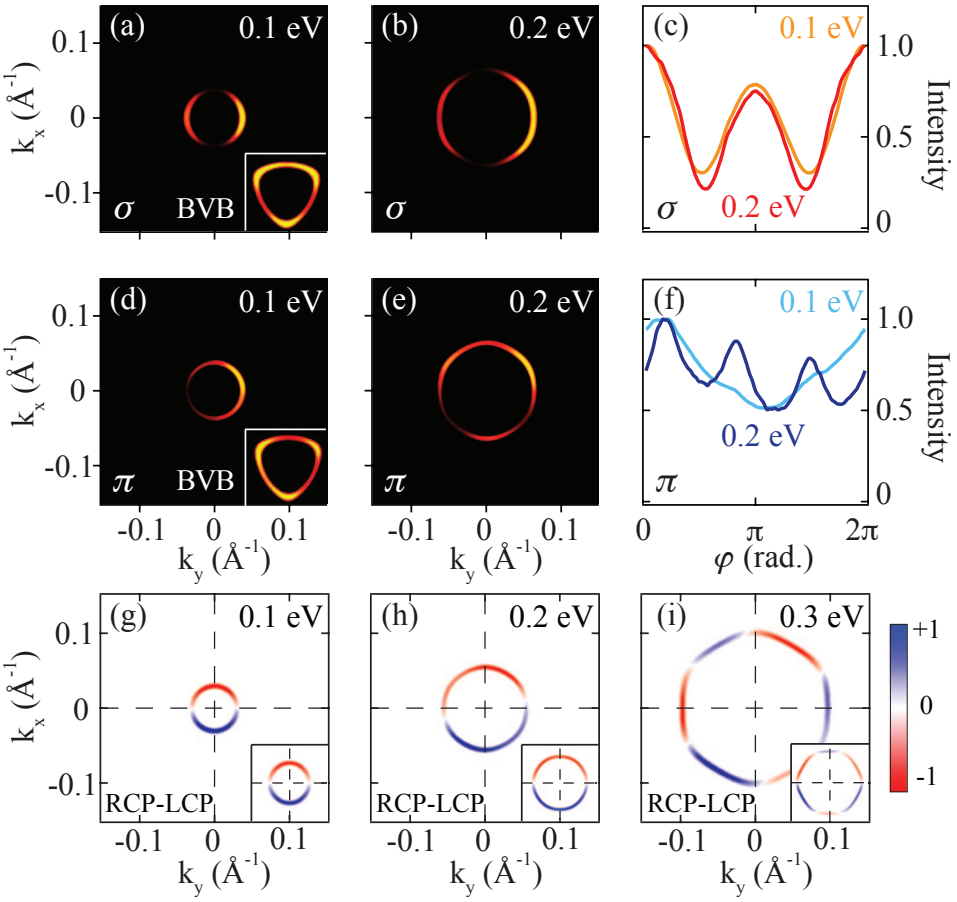

Figure 5.3: Calculated ARPES polarization dependence. (a), (b) Calculated constant-energy σ-polarization ARPES maps for TSS (0.1 and 0.2 eV) and bulk valence band (BVB, -0.1 eV in the inset); (c) corresponding variation of the ARPES intensity versus the in-plane angle φ. (d)–(f) Same data as in (a)–(c), but now for π-polarization. (g)–(i) Calculated constant-energy circular dichroism ARPES patterns at 0.1, 0.2, and 0.3 eV above the DP; insets: patterns obtained by rotating the sample by 90 ° about the normal.

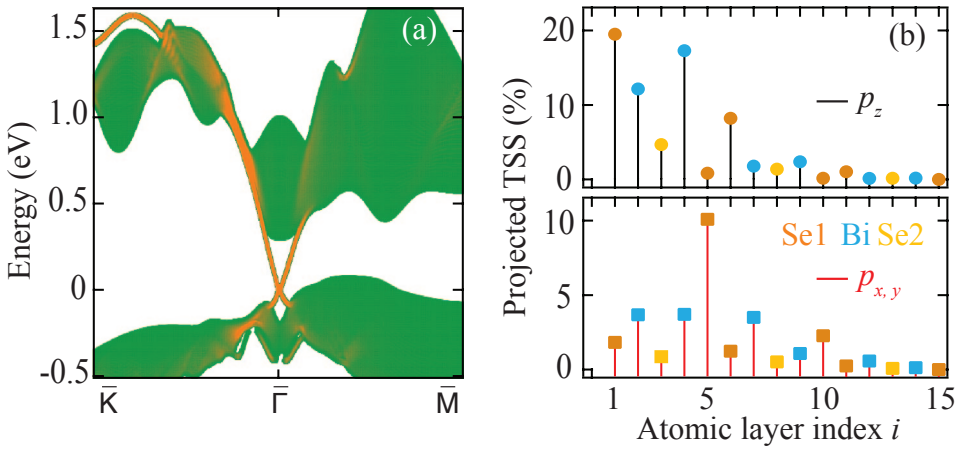

Figure 5.4: Layer-projected topological surface state. (a) Electronic dispersion from our 250-atomic-layer-slab DFT model, with TSS in orange and bulk states in green (Ψ_{TSS} is composed of those states that exceed a 20% projection onto the top five atomic layers in real space). (b) Percentage contribution of p_z and $p_{x,y}$ orbitals to Ψ_{TSS} at 0.15 eV above the DP, resolved layer-by-layer, for the top 15 atomic layers of the slab (Se1 is the natural cleavage plane).

that the ARPES intensity visible at the $\bar{\Gamma}$ point in Fig. 5.2(b) and (e), but not reproduced by our calculations, originates from the scattering-induced broadening of the bulk conduction band[8]. As a final test of the robustness of our DFT analysis of Ψ_{TSS}, we have calculated constant-energy circular dichroism ARPES patterns, which are also in excellent agreement with previous studies [111, 112].

[8] In the experiment, the bulk conduction band is significantly broadened by disorder-induced scattering, which leads to intensity leaking down to lower binding energies inside the gap, an effect not accounted for in our calculations. We also note that while this same disorder affects to some degree the linewidth and electronic filling of the TSS, its main features – such as dispersion and spin-orbital texture close to the Dirac point – are retained, as a manifestation of topological protection [109, 110].

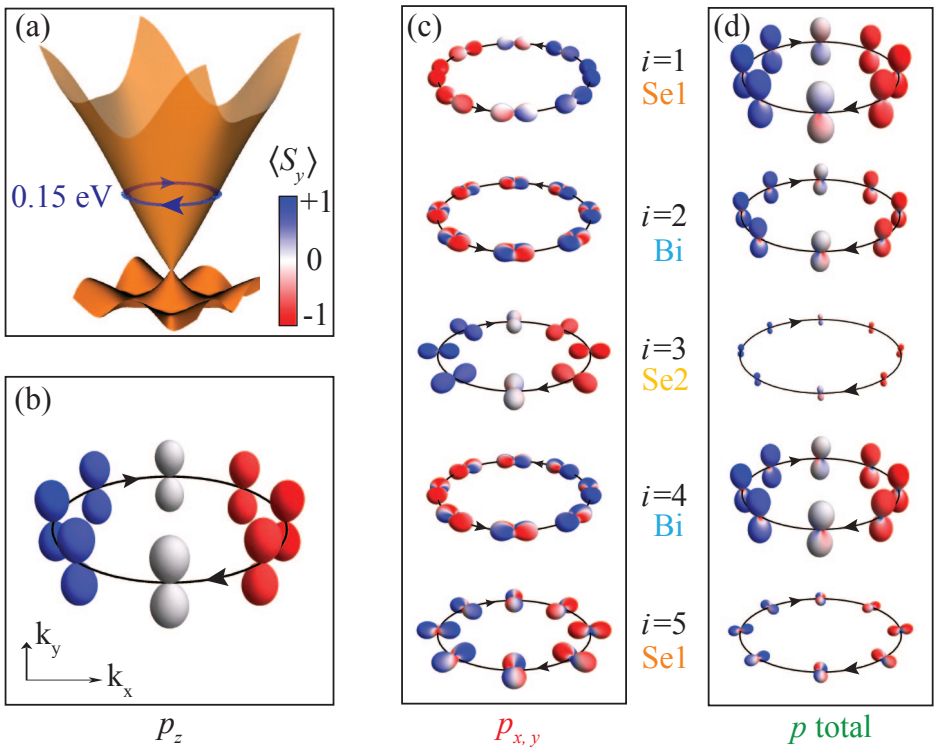

Figure 5.5: Layer-by-layer entangled spin-orbital texture. (b)–(d) Layer- and orbital-projected charge density along the 0.15 eV k-space contour indicated in (a): their surfaces are defined by $r(\theta,\phi) = \sum_{\tau,\tau'} Z_\tau(\theta,\phi) Z_{\tau'}(\theta,\phi) \langle a^\dagger_{i,\tau,k} a_{i,\tau',k} \rangle$, where i and τ are the layer and local orbital basis indexes, and Z the cubic harmonics; their surface color represents the expectation value of the S_y operator. While the p_z channel is layer independent (b), a strong layer-dependent spin-orbital entanglement is observed for $p_{x,y}$ (c). The *total* layer-resolved TSS texture (d) is obtained by adding all p orbital contributions according to their relative, layer-dependent weight from panel [Fig. 5.4(b)].

5.3 Layer-dependent entangled spin-orbital texture

To gain a microscopic understanding of the properties of Ψ_{TSS} we present our DFT results for a 250-atomic-layer slab of Bi_2Se_3[9] in Fig. 5.4(a), with bulk states in green and TSS in orange. The in- and out-of-plane p orbital projections in Fig. 5.4(b) confirm that Ψ_{TSS} indeed has a large p_z (70%) character – although $p_{x,y}$ (30%) is also significant – and most importantly that Ψ_{TSS} extends deep into the solid. Even though the orbital weight decays exponentially with the distance from the surface, as expected for a surface bound-state, Ψ_{TSS} extends approximately 2 quintuple layers (QL) below the surface ($\sim 2\,\mathrm{nm}$), with ∼75% contribution from the 1^{st} QL and ∼25% from the 2^{nd} QL. Note also the interesting layer dependence of the orbital character: while for most layers the main component is the out-of-plane p_z, for the 5^{th} for example the in-plane $p_{x,y}$ is actually dominant.

As a consequence of the relativistic SOC, which directly connects orbital to spin flips via the $l^{\pm}s^{\mp}$ terms of the spin-orbit operator $\mathbf{l}\cdot\mathbf{s} = l_z s_z + (l^+ s^- + l^- s^+)/2$, the strongly layer-dependent orbital occupation becomes entangled with the spin polarization of Ψ_{TSS}. To visualize this entanglement, in Figs.5.5(b)–(d) we present the layer- and orbital-projected charge density along the 0.15 eV Dirac contour indicated in Fig.5.5(a), colored according to the expectation value of the S_y operator. The p_z-projected charge density, being associated with a single orbital, cannot be entangled and has the layer-independent spin helicity shown in Fig. 5.5(b)[10]. In contrast, a strong layer-dependent spin-orbital entanglement is observed for $p_{x,y}$ because the eigenstates can be a linear combination of $p_{x,\uparrow}$, $p_{y,\downarrow}$, and similar states, resulting in a complex set of charge-density isosurfaces. These surfaces show two overall spatial configurations having opposite spin helicity, which are oriented tangentially and radially with respect to the Dirac cone contour[11],

[9] See methods in Section 5.6.1.

[10] Note that in the k_y direction the charge density is white because a state with spin in the x direction is written as a linear combination of states with equal amount of spin *up* and spin *down* along the y direction.

[11] Interestingly the in-plane spin-orbital entanglement is reversed for states below the

as seen in Fig. 5.5(c). In Fig. 5.5(d) we show the total layer-dependent charge density obtained by adding in- and out-of-plane contributions according to their relative weights in Fig. 5.4(b); from this it is clear that while the p_z orbitals dominate, the in-plane $p_{x,y}$ orbitals lead to a substantial spin-orbital entanglement of the combined Ψ_{TSS}.

We will now highlight the interplay between photoelectron interference and the measured ARPES intensity. While a complete derivation – inclusive of selection rules, Bi and Se cross sections, as well as photoelectron escape depth – is given in Section 5.6.1 and 5.6.2, for the purpose of this discussion we approximate the ARPES intensity as $I \propto |\langle e^{i\mathbf{k}\cdot\mathbf{r}}|\mathbf{A}\cdot\mathbf{p}|\Psi_{\mathrm{TSS}}\rangle|^2$, expressed in terms of plane-wave photoelectron final states for simplicity. By writing Ψ_{TSS} as linear combination of the layer-dependent eigenstates, $\Psi_{\mathrm{TSS}} = \sum_{i,\sigma} \alpha_i \psi^{\sigma}_{i,\mathbf{k}_\parallel}$ with i and σ being layer and spin indexes, the ARPES intensity then becomes $I \propto \sum_\sigma |\sum_i e^{-ik_z z_i} \langle e^{i\mathbf{k}_\parallel \mathbf{r}_\parallel} |\mathbf{A}\cdot\mathbf{p}|\alpha_i \psi^{\sigma}_{i,\mathbf{k}_\parallel}\rangle|^2$. Here the $e^{-ik_z z_i}$ phase term accounts for the photoelectron optical path difference stemming from the TSS finite extent into the bulk. Because both $e^{-ik_z z_i}$ and $\psi^{\sigma}_{i,\mathbf{k}_\parallel}$ vary from layer to layer [the latter via the relative orbital content as shown in Fig. 5.7(b)], the photoemission intensity is dominated by interference between the $\psi^{\sigma}_{i,\mathbf{k}_\parallel}$ eigenstates, and can in fact be regarded as the Fourier transform of the layer-dependent Ψ_{TSS}. We also note that, because the phase of photoelectrons is defined by additive k_z and $\mathbf{k}_\parallel$ contributions, reversing the sign of either k_z or $\mathbf{k}_\parallel$ will change the ARPES intensity, i.e., $I(k_z) \neq I(-k_z)$ and especially $I(\mathbf{k}_\parallel) \neq I(-\mathbf{k}_\parallel)$ as observed experimentally.

5.4 TSS spin texture and photoelectron spin polarization

The spin-orbital entanglement also leads to complex in- and out-of-plane spin-texture, as shown in Figs. 5.6(a)–(d) where the layer-integrated spin patterns of individual and total p orbitals are presented. While for p_z we find the in-plane helical spin texture expected for the TSS this is not the case

DP: while the spin helicity remains the same as above the DP, the orbital texture switches between tangential and radial configurations.

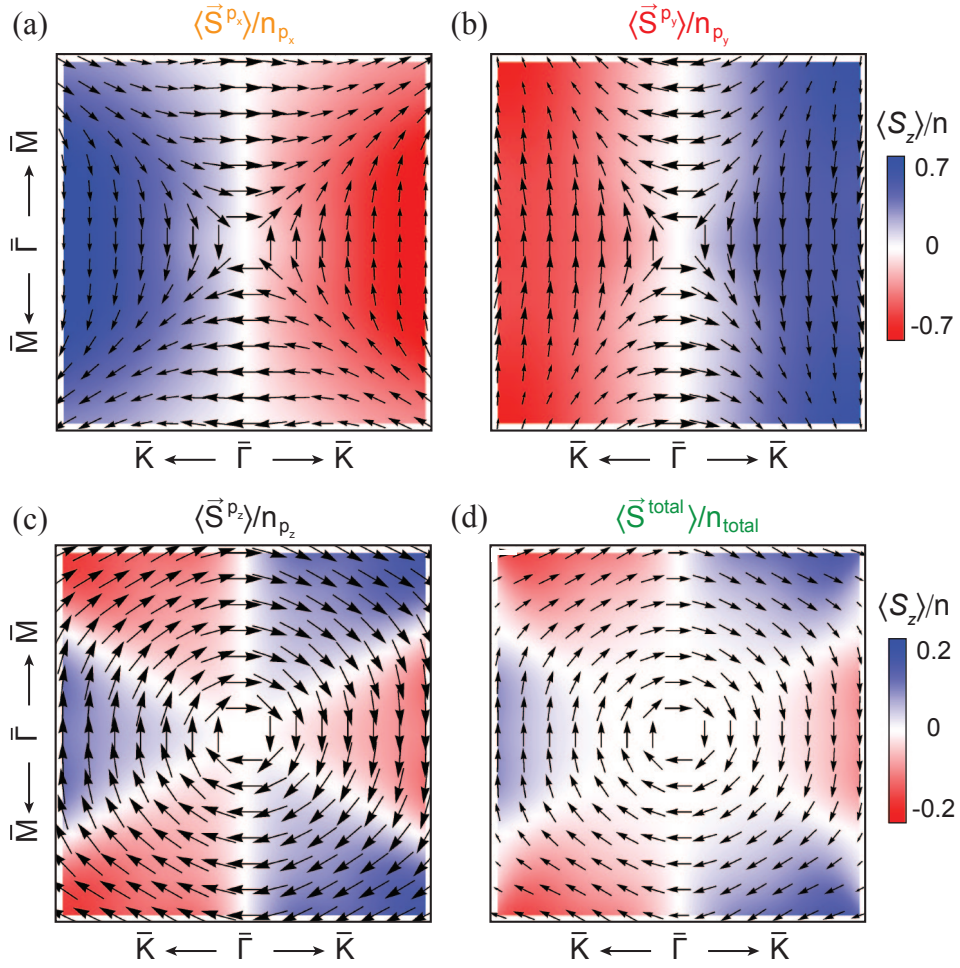

Figure 5.6: Orbital-projected spin texture of TSS. (a)–(d) Spin texture of the Dirac cone upper branch in Bi_2Se_3 obtained from the expectation value of the layer-integrated, orbital-projected spin operators, normalized to the orbital occupation [shown in Fig. 5.8(a)]; in-plane and out-of-plane spin components are represented by arrows and colors, respectively. Note that (a), (b) and (c), (d) have different color scales but that the arrow scaling remains the same, with the largest arrows representing full polarization; also, moving away from $\bar{\Gamma}$ corresponds to moving along the Dirac dispersion away from the DP ($\sim$0.4 eV at the map edge).

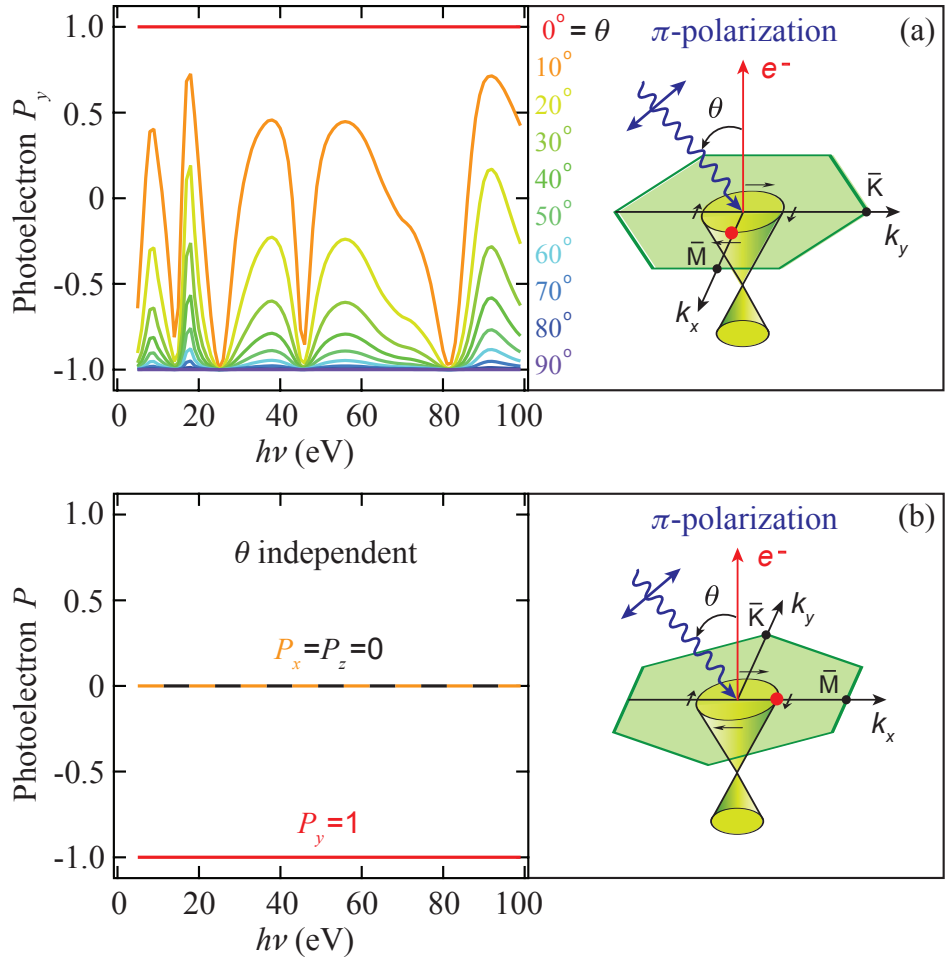

Figure 5.7: Calculated photoelectron spin polarization. (a), (b) Prediction for the photoelectron spin polarization (P) measured in SARPES as a function of photon energy and incidence angle; two experimental geometries are examined in π polarization for the same k point located at 0.15 eV along $\bar{\Gamma}-\bar{\mathrm{M}}$, as indicated in the sketches [in (a) only the P component along y is shown].

for the p_x and p_y orbitals, which exhibit patterns opposite to one another. Combining all contributions [$\langle\vec{S}^{\mathrm{total}}\rangle/n_{\mathrm{total}}$ in Fig. 5.6(d)], the TSS out-of-plane spin texture vanishes in the vicinity of the DP; most important, the in-plane spin polarization is reduced from 100% to 75% at the DP, and to

60% at 0.4 eV above the DP. Note that this is also critically dependent on the relative $p_{x,y}$ orbital content of Ψ_{TSS}, which increases from 25% to 45% over the same energy range[12].

Photoelectron interference also severely affects the photoelectron spin polarization $P_{x,y,z} = (I^{\uparrow x,y,z} - I^{\downarrow x,y,z})/(I^{\uparrow x,y,z} + I^{\downarrow x,y,z})$ measured in SARPES. This exhibits a strong dependence on photon energy, polarization, and angle of incidence, which in general prevents the straightforward experimental determination of the intrinsic spin-texture of Bi_2Se_3. While comprehensive results are presented in Section 5.6.5, in Figs. 5.7(a) and (b) we show as an example the same k point along $\bar{\Gamma}-\bar{\mathrm{M}}$ measured in two different geometries, probing selectively $p_{y,z}$ (a) and $p_{x,z}$ (b) orbitals. In Fig. 5.7(a), because $\langle \vec{S}^{p_y} \rangle$ and $\langle \vec{S}^{p_z} \rangle$ (the spin polarization of the p_y and p_z orbitals) are antiparallel at this specific k point, P_y varies between $\pm 100\%$ upon changing θ, and oscillates wildly as a function of photon energy (with the exception of $0\,^\circ$ and $90\,^\circ$, which probe p_y and p_z separately). However, if the sample is rotated by $90\,^\circ$ as in Fig. 5.7(b) $\langle \vec{S}^{p_x} \rangle$ becomes parallel to $\langle \vec{S}^{p_z} \rangle$ and the measured $P_{x,y,z}$ are all independent of photon energy and incidence angle, allowing the detection of the intrinsic spin polarization. We note that this behavior is consistent with reported SARPES results [102]: for the situation of Fig. 5.7(b), $P_y > 80\%$ was obtained, close to our 100% expectation; along $\bar{\Gamma}-\bar{K}$, P_y was observed to vary from 25% at $h\nu = 36$ eV to -50% at 70 eV, while we obtain $+20\pm10\%$ and $-40\pm15\%$, respectively.

5.5 Conclusion

We have shown that the spatial extent of the TSS into the solid and its strong layer-dependent spin-orbital entanglement are responsible – via photoelectron interference – for the apparent time-reversal symmetry breaking in ARPES and the large discrepancy in the estimated TSS spin-polarization from SARPES. This is of critical importance for many applications and fundamental studies of TIs. For instance we note that the photoelectron interference responsible for $I(\mathbf{k}_\parallel) \neq I(-\mathbf{k}_\parallel)$ in ARPES also provides an

[12] See Fig. 5.8 in Section 5.6.4.

explanation for the so-far puzzling observation of spin-polarized electrical currents photoinduced by linearly-polarized light [113], which also is associated with an imbalance in the number of photoelectrons removed at $\pm\mathbf{k}_{\parallel}$. In addition, exploiting photoelectron interference in SARPES provides a way not only to probe the intrinsic spin texture of TIs, but also – and most importantly – to continuously manipulate the spin polarization of photoelectrons and photocurrents all the way from 0 to $\pm 100\%$ by an appropriate choice of photon energy, polarization, and angle of incidence.

5.6 Supplemental material

5.6.1 Experimental and theoretical methods

Angle-resolved photoemission spectroscopy (ARPES) was performed at UBC using a SPECS Phoibos 150 hemispherical analyzer and a monochromatized and linearly polarized UVS300 gas-discharge lamp. Energy and angular resolutions were set to 10 meV and $\pm 0.1°$. We used 21.2 eV photons, whose close-to-100% linear polarization can be rotated to any angle without changing sample orientation; in this study we focused on experiments for horizontal (π) and vertical (σ) polarizations. Bi_2Se_3 single crystals were grown from the melt at the University of Maryland [with carrier density $n \simeq 1.24\times10^{19}\,\mathrm{cm}^{-3}$ [69]], and by floating zone at the University of Geneva. The samples were prealigned ex situ by conventional Laue diffraction, and cleaved and measured at pressures better than 5×10^{-11} torr and at a constant temperature of 6 K [1].

The bulk electronic structure of Bi_2Se_3 was calculated using the tight-binding order-N muffin-tin orbital (TB-NMTO) [50, 57] and full-potential WIEN2k [44] density functional theory codes; we find excellent agreement between the two methods. The TB-NMTO approach is used to down-fold the ab initio Hamiltonian to a 15-band model involving only the p orbitals of Bi and Se. This allows us to extract on-site energies and hopping parameters which are used to construct a 250-atomic-layer thick slab TB model (i.e., 50 quintuple layers), with atomic spin-orbit coupling (SOC) included

as a local term for Bi and Se orbitals [1.25 eV and 0.22 eV, respectively [59]]. To understand the microscopic origin of the ARPES intensity patterns in Fig. 5.1, we have performed photoemission intensity calculations for both linearly and circularly polarized light. Following an established approach [107], photoelectron final states are treated as spin-degenerate plane waves; however, to account for ARPES matrix elements, these plane waves have been expanded in spherical harmonics and Bessel functions around each atom. Since the initial states have mainly p orbital character, conservation of angular momentum only allows excitations into s and d-like free-electron states. Under these selection rules, photoelectrons from p_x, p_y, and p_z orbitals can be excited by x, y, and z polarized light respectively [37]; all other excitations are forbidden. Finally, the Bi and Se atomic cross sections [e.g., 2.7 for Bi $6p$ and 8.0 for Se $4p$ at photon energy 21.2 eV [114]] also have been taken into account in calculating photoemission intensities, as well as the finite escape depth of the photoelectrons. Also note that throughout the chapter, the coordinate system is consistent with the crystal structure: the k_x axis is along $\bar{\Gamma}-\bar{\mathrm{M}}$, the k_y axis is along $\bar{\Gamma}-\bar{K}$, and the z axis is along the sample normal [001].

5.6.2 ARPES intensity and interference effects

In the following sections we will show how we calculated the data presented in Sections 5.2 and 5.4. We will begin, in this section, by calculating the explicit ARPES intensity based on our ab initio TB model[13]. In the following Section 5.6.3, we will calculate the spin-polarization of photoelectrons, and how that relates to the TSS ground-state spin-polarization; importantly we will note how they can differ due to interference terms, and also depend on the relative orbital occupations. In Section 5.6.4 we will present these relative orbital occupations, while in Section 5.6.5 we resolve the interference terms and explicitly present the spin texture patters of photoelectrons for some example experimental configurations. In Section 5.6.6, we will demonstrate how certain aspects of these results, namely the asymmetry in in-

[13] An introduction about the ab initio TB model is given in Chapter 3.

tensity between $k_\parallel$ and $-k_\parallel$, can be understood through a simple model system.

Based on Fermi's golden rule, the photoemission intensity can be written as [37, 107]:

$$I \propto |\langle \Psi_f | \mathbf{A} \cdot \mathbf{p} | \Psi_i \rangle|^2, \tag{5.1}$$

where $\mathbf{p}$ is the electron momentum operator, $\mathbf{A}$ the electromagnetic vector potential, and Ψ_i and Ψ_f the initial- and final-state wave functions. We use the dipole approximation in the calculations such that $\mathbf{A} \cdot \mathbf{p}$ is approximated by $\mathbf{r}$. Here we focus on the photoemission of the topological surface states (TSS). Therefore, $\Psi_i = \Psi_{\mathrm{TSS}}$ which is the wave function of the TSS and can be written as a linear combination of atomic wave function in our ab initio TB model:

$$\Psi_{\mathrm{TSS}} = \sum_{i,\tau,\sigma} C^{\sigma}_{i,\tau} \psi_{i,\tau}. \tag{5.2}$$

Here i is the atomic layer index along the z axis of the slab with the surface layer at $i = 1$, the orbital basis is given by $\tau \in \{p_x, p_y, p_z\}$, σ is the spin index which is $\uparrow$ or $\downarrow$, and $\psi_{i,\tau}$ are the atomic wave functions of orbital τ centered around the atomic layer i. The photoelectron final states are treated as free-electron-like, whose wave function can be described by a plane wave $\Psi_f = e^{\mathrm{i}\mathbf{k}\cdot\mathbf{r}}$. We can therefore define the matrix element term as:

$$M_{i,\tau} \equiv \langle e^{\mathrm{i}\mathbf{k}\cdot\mathbf{r}} | \mathbf{A} \cdot \mathbf{p} | \psi_{i,\tau} \rangle. \tag{5.3}$$

As discussed in section 5.3, the TSS is not a perfect two-dimensional state with a delta-function-like density in the z direction. Instead, it extends more than 2 nm deep into the bulk along the z direction. We take into account the spatial extent of the wave function along z by assigning an atomic-layer-dependent phase to photoelectrons: $e^{\mathrm{i}k_z z_i}$, with z_i being the position of the atomic layer i along z and $k_z = \sqrt{\frac{2m_e}{\hbar^2}(h\nu - E_B) - k_x^2 - k_y^2}$ is the momentum of photoelectrons along z, which depends on photon energy $h\nu$ and the initial-state binding energy E_B. Note that the phase of the photoelectrons is determined by their kinetic energy inside the material rather than in the vacuum; for this reason we do not consider the work

function here. The finite photoelectron escape depth is also considered in our calculation, by including an exponential attenuation factor dependent on the mean free path (λ) of the photoexcited electrons; we used $\lambda = 7\,\text{Å}$, although no substantial change in our results was observed in the 5–10 Å range. In order to show the effects of photon energy and escape depth, we redefine Eq. 5.3 as:

$$M_{i,\tau} \equiv e^{-\mathrm{i}k_z z_i} e^{-z_i/(2\lambda)} \langle e^{\mathrm{i}\mathbf{k}_\parallel \cdot \mathbf{r}_\parallel} | \mathbf{A} \cdot \mathbf{p} | \psi_{i,\tau} \rangle. \tag{5.4}$$

with $\mathbf{k} = \{k_x, k_y, k_z\}$ and $\mathbf{k}_\parallel = \{k_x, k_y\}$. Finally, Eq. 5.1 can be written as the sum of the intensity from up and down spin channels:

$$I \propto \sum_{\sigma=\uparrow,\downarrow} |\sum_{i,\tau} C^{\sigma}_{i,\tau} M_{i,\tau}|^2. \tag{5.5}$$

The latter we can expanded to obtain the explicit form of the ARPES intensity:

$$\begin{aligned} I = & \sum_{i,\tau} (C^{\uparrow}_{i,\tau}{}^{*} C^{\uparrow}_{i,\tau} + C^{\downarrow}_{i,\tau}{}^{*} C^{\downarrow}_{i,\tau}) |M_{i,\tau}|^2 \\ & + \sum_{i \neq i', \tau \neq \tau'} (C^{\uparrow}_{i,\tau}{}^{*} C^{\uparrow}_{i',\tau'} + C^{\downarrow}_{i,\tau}{}^{*} C^{\downarrow}_{i',\tau'}) M^{*}_{i,\tau} M_{i',\tau'}. \end{aligned} \tag{5.6}$$

Here $\sum_{i,\tau} C^{\uparrow}_{i,\tau}{}^{*} C^{\uparrow}_{i,\tau} + C^{\downarrow}_{i,\tau}{}^{*} C^{\downarrow}_{i,\tau} = 1$ for the normalized TSS wave function and the sum $\sum_{i \neq i', \tau \neq \tau'}$ represents the interference between different terms in the basis set – i.e., orbitals in the same or different atomic layers.

5.6.3 Photoelectron spin polarization

There is a clear analytical relationship between the photoelectron spin polarization measured by SARPES and the TSS ground-state spin polarization obtained from the expectation value of spin operators applied on the TSS wave function. In a simple system with a single orbital and a single atomic layer, the photoelectron spin polarization is given by the TSS ground-state spin polarization. For a system with multiple orbitals and atomic layers,

the interference terms become important and lead to a deviation from the single-orbital and single-atomic-layer system. In the following part of this section, we will derive the relationship in the multi-orbital and -atomic layer system with the interference term included.

SARPES measures the spin polarization along different quantization axes, which here are the x , y and z directions as defined in Fig. 5.1(a), Section 5.2. The photoelectron spin polarization vector (P) is defined as $P = [P_x, P_y, P_z]$ where:

$$P_{x,y,z} = \frac{I^{\uparrow_{x,y,z}} - I^{\downarrow_{x,y,z}}}{I^{\uparrow_{x,y,z}} + I^{\downarrow_{x,y,z}}}. \tag{5.7}$$

Hereafter, we define $\uparrow$ ($\downarrow$) $\equiv\uparrow_z$ ($\downarrow_z$) and use the usual spin relations:

$$\begin{aligned} |\uparrow\rangle &= \frac{1}{\sqrt{2}}(|\uparrow_x\rangle + |\downarrow_x\rangle) = \frac{1}{\sqrt{2}}(|\uparrow_y\rangle + |\downarrow_y\rangle), \\ |\downarrow\rangle &= \frac{1}{\sqrt{2}}(|\uparrow_x\rangle - |\downarrow_x\rangle) = \frac{1}{\sqrt{2}}(-\mathrm{i}|\uparrow_y\rangle + \mathrm{i}|\downarrow_y\rangle). \end{aligned} \tag{5.8}$$

By using Eq. 5.5, 5.7, and 5.8, we can calculate $P_{x,y,z}$:

$$\begin{aligned} P_x =& \frac{\sum_{i,\tau}({C^{\uparrow}_{i,\tau}}^* C^{\downarrow}_{i,\tau} + {C^{\downarrow}_{i,\tau}}^* C^{\uparrow}_{i,\tau})|M_{i,\tau}|^2}{I} \\ &+ \frac{\sum_{i\neq i',\tau\neq\tau'}({C^{\uparrow}_{i,\tau}}^* C^{\downarrow}_{i',\tau'} + {C^{\downarrow}_{i,\tau}}^* C^{\uparrow}_{i',\tau'})M^*_{i,\tau}M_{i',\tau'}}{I}, \\ P_y =& \frac{\sum_{i,\tau}\mathrm{i}(-{C^{\uparrow}_{i,\tau}}^* C^{\downarrow}_{i,\tau} + {C^{\downarrow}_{i,\tau}}^* C^{\uparrow}_{i,\tau})|M_{i,\tau}|^2}{I} \\ &+ \frac{\sum_{i\neq i',\tau\neq\tau'}\mathrm{i}(-{C^{\uparrow}_{i,\tau}}^* C^{\downarrow}_{i',\tau'} + {C^{\downarrow}_{i,\tau}}^* C^{\uparrow}_{i',\tau'})M^*_{i,\tau}M_{i',\tau'}}{I}, \end{aligned} \tag{5.9}$$

$$P_z = \frac{\sum_{i,\tau}(C_{i,\tau}^{\uparrow\ *} C_{i,\tau}^{\uparrow} - C_{i,\tau}^{\downarrow\ *} C_{i,\tau}^{\downarrow})|M_{i,\tau}|^2}{I} + \frac{\sum_{i\neq i',\tau\neq\tau'}(C_{i,\tau}^{\uparrow\ *} C_{i',\tau'}^{\uparrow} - C_{i,\tau}^{\downarrow\ *} C_{i',\tau'}^{\downarrow})M_{i,\tau}^{*} M_{i',\tau'}}{I}.$$

In order to clarify the relationship between the photoelectron spin polarization (Eq. 5.10) and the TSS ground-state spin polarization, we can express the photoelectron spin polarization in terms of expectation value of spin operators, with the spin operator defined as:

$$S_{\eta}^{i,\tau;\,i',\tau'} = |\psi_{i,\tau}\rangle\langle\psi_{i',\tau'}|\sigma_{\eta}, \tag{5.10}$$

where $\eta \in \{x, y, z\}$ and $\sigma_{x,y,z}$ are the Pauli spin matrices. Using Eq. 5.2 and Eq. 5.10, one can write down the expression for the layer- and orbital-projected expectation value of spin operators:

$$\begin{aligned}
\langle S_x^{i,\tau;\,i',\tau'}\rangle &= C_{i,\tau}^{\uparrow\ *} C_{i',\tau'}^{\downarrow} + C_{i,\tau}^{\downarrow\ *} C_{i',\tau'}^{\uparrow},\\
\langle S_y^{i,\tau;\,i',\tau'}\rangle &= \mathrm{i}(-C_{i,\tau}^{\uparrow\ *} C_{i',\tau'}^{\downarrow} + C_{i,\tau}^{\downarrow\ *} C_{i',\tau'}^{\uparrow}),\\
\langle S_z^{i,\tau;\,i',\tau'}\rangle &= C_{i,\tau}^{\uparrow\ *} C_{i',\tau'}^{\uparrow} - C_{i,\tau}^{\downarrow\ *} C_{i',\tau'}^{\downarrow}.
\end{aligned} \tag{5.11}$$

The spin-polarization vector of the TSS ground state, defined as $\langle S^{\mathrm{TSS}}\rangle = [\langle S_x\rangle, \langle S_y\rangle, \langle S_z\rangle]$, is the sum of the expectation value of spin operators shown in Eq. 5.10 with $i = i'$ and $\tau = \tau'$: $\langle S_{\eta}^{\mathrm{TSS}}\rangle = \sum_{i,\tau}\langle S_{\eta}^{i,\tau}\rangle$. When $i \neq i'$ and $\tau \neq \tau'$, the spin operator in Eq. 5.10 represents the interference effect in the photoelectron spin polarization.

Plugging Eq. 5.11 into Eq. 5.10, we can now rewrite the photoelectron spin polarization in terms of the expectation values of spin operators as defined in Eq. 5.10:

$$P_{\eta} = \frac{\sum_{i,\tau}\langle S_{\eta}^{i,\tau}\rangle|M_{i,\tau}|^2 + \sum_{i\neq i',\tau\neq\tau'}\langle S_{\eta}^{i,\tau;\,i',\tau'}\rangle M_{i,\tau}^{*} M_{i',\tau'}}{I}. \tag{5.12}$$

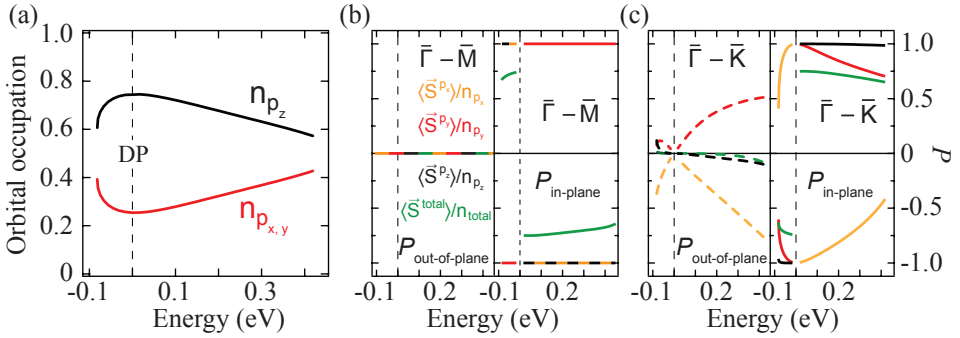

Figure 5.8: Energy dependence of the layer-integrated TSS orbital characters and spin polarization. (a) Energy dependence of the $p_{x,y}$ and p_z relative contributions to the TSS wave function. (b)–(c) cuts through Fig. 5.6 in the Section 5.4 showing the relative out-of-plane (left panel) and in-plane (right panel) spin polarization (P) of individual p orbitals as a function of energy along $\bar{\Gamma} \rightarrow \bar{\mathrm{M}}$ (b) and $\bar{\Gamma} \rightarrow \bar{K}$ (c) [obtained from the expectation value of layer-integrated, orbital-projected spin operators, normalized to the orbital occupation shown in (a)].

This shows the relationship between the photoelectron and the TSS ground-state spin polarization. We can see that the matrix element $M_{i,\tau}$ and the interference term $\sum_{i\neq i',\tau\neq\tau'}$ can make the photoelectron spin polarization deviate from the TSS ground-state spin polarization.

5.6.4 TSS orbital character and spin polarization

As shown in Section 5.4, Fig. 5.6, p_x and p_y orbitals have almost opposite in-plane spin textures. Therefore, the in-plane spin polarization from the $p_{x,y}$ channel is almost zero over a large energy window, which results in a less than 100% TSS in-plane spin polarization. This orbital-dependent spin texture makes the relative occupation of $p_{x,y}$ and p_z critical to determine the value of the TSS in-plane spin polarization. Upon moving away from the Dirac point (DP), the $p_{x,y}$ occupation increases from 25% to 45% and the p_z occupation correspondingly decreases, as shown in Fig. 5.8(a). The in-plane and out-of-plane spin polarization of individual orbitals is shown in Fig. 5.8(b) [along $\bar{\Gamma} \rightarrow \bar{\mathrm{M}}$) and Fig. 5.8(c) ($\bar{\Gamma} \rightarrow \bar{K}$]. We can see that the TSS

spin polarization for the total of p orbitals can never reach 100%; instead it decreases from 75 to $\sim 60\%$ while energy is increasing from 0 to 0.4 eV.

5.6.5 Manipulation of ARPES spin texture

In Section 5.4, Fig. 5.7, we show that the photoelectron spin polarization can strongly depend on photon energy and experimental geometry. Here, in Fig. 5.9, we explicitly present the spin texture patterns of photoelectrons as measured by SARPES using four different light polarizations and five photon energies. The strong deviations between photoelectron and TSS ground-state spin textures can be seen by comparing Figs. 5.9(b)–(d) to Figs. 5.6(a)–(d) in Section 5.4. One can also observe a remarkably strong and nontrivial photon energy dependence for the experimentally determined spin texture of photoelectrons. The only exception is the result obtained with π-polarization at a 90° incidence angle [Fig. 5.9(a)]: in this case one only probes initial states with p_z orbital character, whose spin texture is nearly layer-independent.

In Fig. 5.10, we focus on the photoelectron spin polarization vector at two $\mathbf{k}$ points under two experimental geometries, as a function of photon energy and incidence angle of π-polarized light. The photoelectrons excited under different experimental geometries are composed of electrons with different spin orientations, depending on their orbital source. Even at the same $\mathbf{k}$ point, the photoelectron spin polarization will change if we change the experimental geometry, as it can be seen by comparing Fig. 5.10(a) to Fig. 5.11(a) or Fig. 5.10(b) to Fig. 5.11(b). Moreover, the photoelectron spin polarization can be non-zero along directions which are expected to be zero based on the spin polarization of the TSS ground state. For instance, P_y and P_z in Fig. 5.10(a), P_x and P_z in Fig. 5.10(b), P_y and P_z in Fig. 5.11(a) are expected to be zero from the spin polarization of the TSS ground state; however, the photoelectron spin polarization of these components is not zero and has a very strong photon energy dependence as a result of interference effects between photoelectrons from different orbitals. Only the photoelectron spin polarization shown in Fig. 5.11(b) directly presents the TSS ground-state

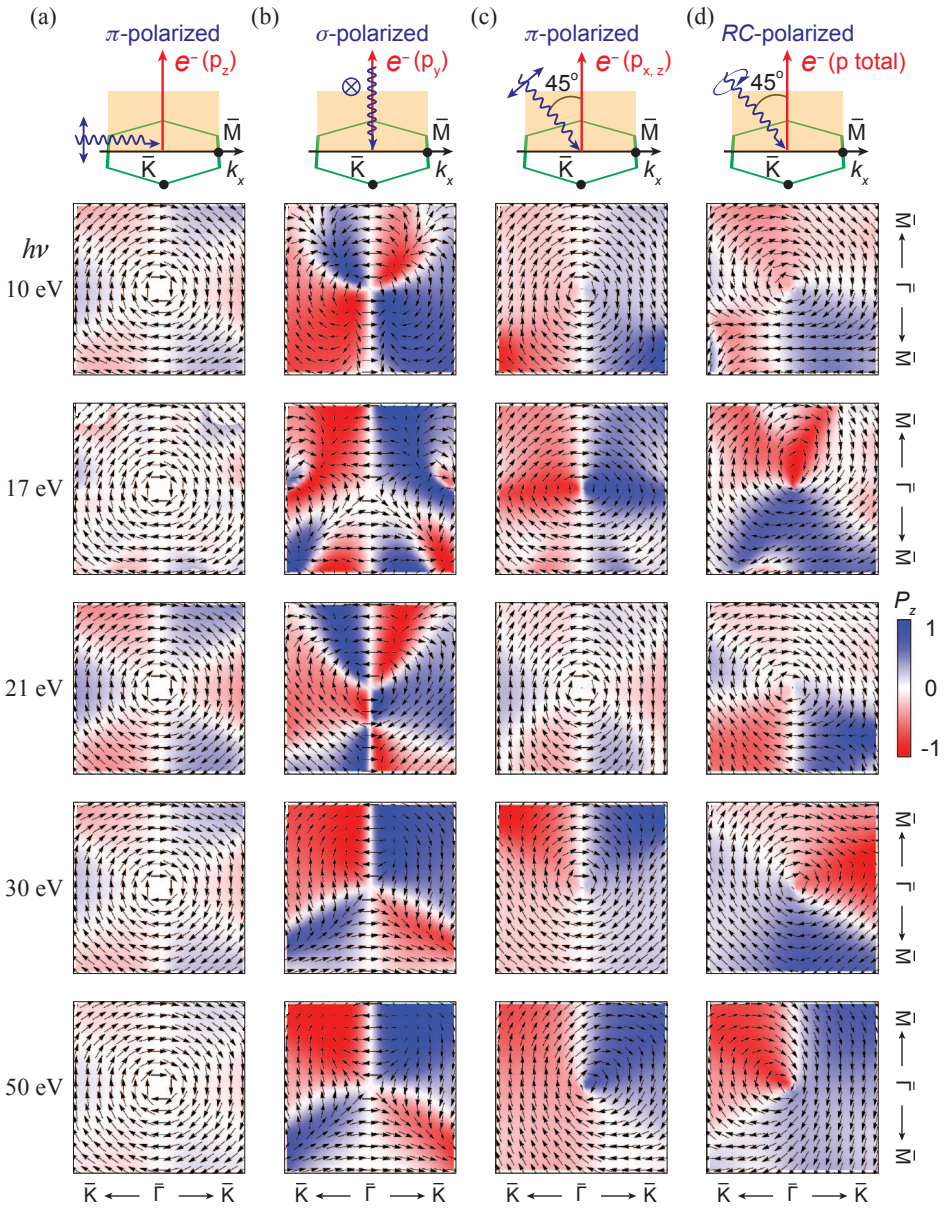

Figure 5.9: Calculated spin textures of photoelectrons excited from the Dirac cone upper branch in Bi_2Se_3, for different photon energies and polarizations. Arrows and colors are used to describe the in-plane and out-of-plane photoelectron spin polarization, respectively; note that moving away from the $\bar{\Gamma}$ point in these maps correspond to moving along the Dirac dispersion away from the DP.

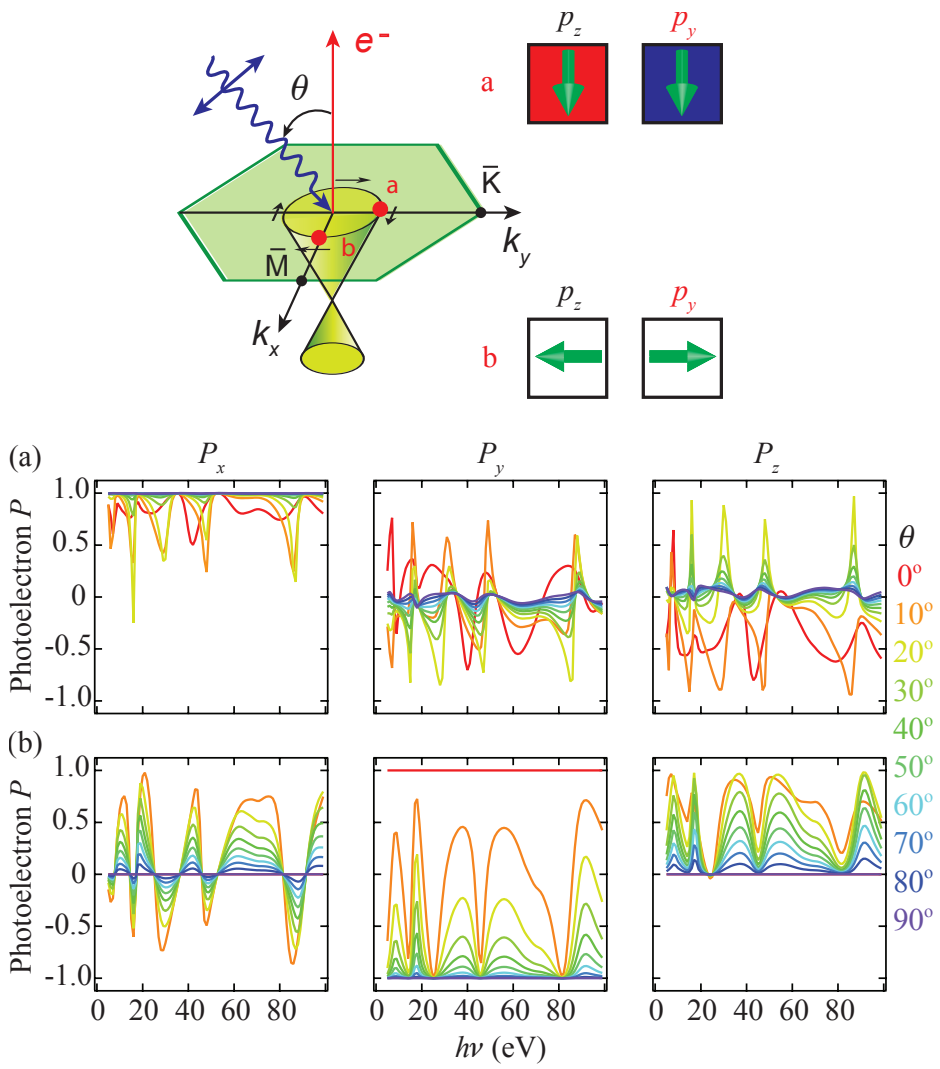

Figure 5.10: Photon-energy dependence of the photoelectron spin polarization at two **k** points. The two measured **k** points are labeled by red dots in the schematics of experimental geometry shown on the top panels. The middle panels with green arrows and blue/red/white squares are used to schematically present the in-plane (green arrows) and out-of-plane (filled color with red: −; white: 0; blue: +) spin polarization of the only two atomic orbitals which emit photoelectrons based on selection rules. The bottom three panels show the three components of the photoelectron spin polarization as a function of photon energy, with different incidence angles (θ) of the π-polarized light shown with color.

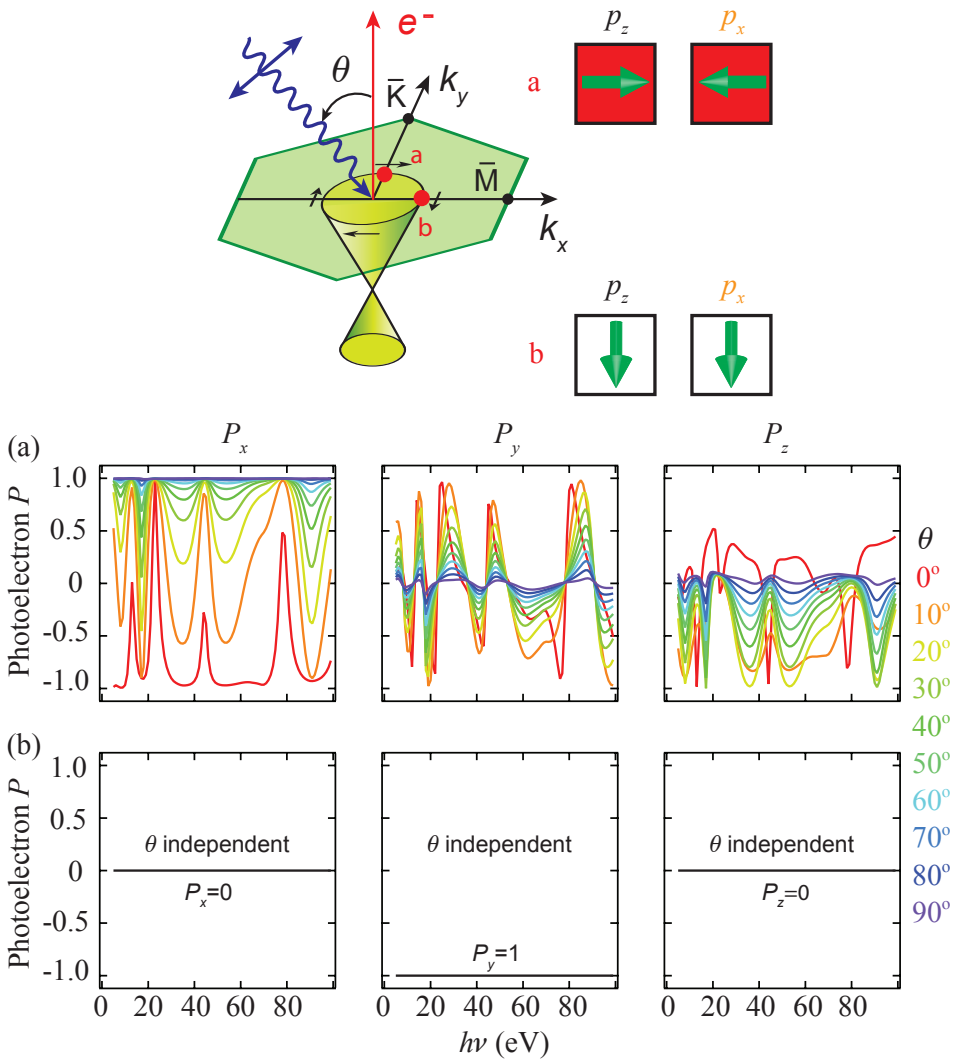

Figure 5.11: Photon-energy dependence of the photoelectron spin polarization at two **k** points. The two measured **k** points are labeled by red dots in the schematics of experimental geometry shown on the top panels. The middle panels with green arrows and blue/red/white squares are used to schematically present the in-plane (green arrows) and out-of-plane (filled color with red: −; white: 0; blue: +) spin polarization of the only two atomic orbitals which emit photoelectrons based on selection rules. The bottom three panels show the three components of the photoelectron spin polarization as a function of photon energy, with different incidence angles (θ) of the π-polarized light shown with color.

spin polarization owing to the fact that – thanks to the choice of geometry and light polarization – all photoelectrons from different layers and selected orbitals have the ground states with the same expectation value of spin operators; this eliminates possible deviations induced by matrix element and interference effects.

Note that our calculated spin polarization of photoelectrons is in quantitative agreement with reported SARPES results [102]. For the situation shown in Figs. 5.11(a) and (b), along $\bar{\Gamma}-\bar{\mathrm{M}}$, $P_y \geq 80\%$ was reported, close to 100% obtained from the calculation; along $\bar{\Gamma}-\bar{K}$, P_y was reported to be 25% at $h\nu = 36\,\mathrm{eV}$ and -50% at $h\nu$=70 eV at $k_y = \pm 0.11\mathrm{\AA}^{-1}$, while our calculation gives $20\% \pm 10\%$ and $-40\% \pm 15\%$, respectively. The uncertainty of our calculated results is estimated based on the uncertain ratio between $p-to-s$ and $p-to-d$ excitations.

5.6.6 Asymmetric ARPES from a simple TSS model

While ab initio density functional theory (DFT) calculations – as presented above – are required in order to describe the complex layer-dependent wave function of the TSS in realistic TI materials, and especially to quantitatively reproduce the experimental data, it is illuminating to explore certain fundamental aspects with as simple a model as possible. Here we will develop a most basic time-reversal-symmetric model to qualitatively capture interference effects on the photoemission intensity patterns, based on the solution of the effective TSS Hamiltonian [33, 64]. First we will express the wave function of the TSS in a basis set of $p_{x,y,z}$ orbitals to account for the *entangled spin-orbital texture*. Then we will generalize it to a model wave function for two atomic layers, to allow for a *layer-dependent* spin-orbital texture. Finally we use it to calculate the asymmetric ARPES using π-polarized light incident in the yz plane, as one of the examples treated in the main content of this Chapter.

The model Hamiltonian for the three-dimensional topological insulators belonging to the Bi_2Se_3 family of materials has been fully derived by Zhang *et al.* [33, 64]. In the basis set $[\Phi_{+\frac{1}{2}}, \Phi_{-\frac{1}{2}}]$ formed by the total angular

momentum with $J_z = \pm\frac{1}{2}$, the effective Hamiltonian for the TSS of Bi_2Se_3 near the $\bar{\Gamma}$ point can be written as [33, 64, 115]:

$$H_{\mathrm{TSS}} = \zeta(\sigma_x k_y - \sigma_y k_x), \tag{5.13}$$

where ζ is the constant coefficient containing the strength of spin-orbit coupling (SOC), $\sigma_{x,y}$ are the spin Pauli matrices, and $k_{x,y}$ represent the electron momentum. The eigenstates of this model Hamiltonian are [33, 64, 115]:

$$\Psi_{\pm} = \frac{1}{\sqrt{2}}[\pm \mathrm{i}e^{-\mathrm{i}\varphi}|\Phi_{\frac{1}{2}}\rangle + |\Phi_{-\frac{1}{2}}\rangle], \tag{5.14}$$

with φ defined by $k_{\parallel}e^{\mathrm{i}\varphi} = k_x + \mathrm{i}k_y$. The exact $\mathbf{k}_{\parallel}$-dependent form of $\Phi_{\pm\frac{1}{2}}$ is determined by the material details. As verified based on the DFT calculations for Bi_2Se_3, near the $\bar{\Gamma}$ point (i.e. away from the bottom of the conduction band) the $\mathbf{k}_{\parallel}$ dependence of $\Phi_{\pm\frac{1}{2}}$ is very weak, and is dominated by the zeroth-order term in $\mathbf{k}_{\parallel}$. Therefore, here we express $\Phi_{\pm\frac{1}{2}}$ in terms of $p_{x,y,z}$ orbitals by only retaining the zeroth-order term, and the basis becomes [115]:

$$\Phi_{\pm\frac{1}{2}} = \alpha|p_z,\uparrow(\downarrow)\rangle \mp \frac{\beta}{\sqrt{2}}[|p_x,\downarrow(\uparrow)\rangle \pm \mathrm{i}|p_y,\downarrow(\uparrow)\rangle], \tag{5.15}$$

where α and β are again material-dependent. Finally, the eigenstates of the model Hamiltonian (Eq. 5.13) in the $[p_x, p_y, p_z]$ basis, with spin up ($\uparrow$) and spin down ($\downarrow$), become [33, 64, 115]:

$$\begin{pmatrix}\Psi_{\pm}^{\uparrow}\\ \Psi_{\pm}^{\downarrow}\end{pmatrix} = \frac{\alpha}{\sqrt{2}}\begin{pmatrix}\pm\mathrm{i}e^{-\mathrm{i}\varphi}\\ 1\end{pmatrix}|p_z\rangle - \frac{\beta}{2}\begin{pmatrix}-1\\ \pm\mathrm{i}e^{-\mathrm{i}\varphi}\end{pmatrix}|p_x\rangle + \frac{\beta}{2}\begin{pmatrix}-\mathrm{i}\\ \pm e^{-\mathrm{i}\varphi}\end{pmatrix}|p_y\rangle. \tag{5.16}$$

The orbital-dependent spin texture for this model wave function – which qualitatively reproduces the behavior obtained through a complete DFT slab calculations [2] – can be obtained by calculating the expectation value

of spin operators for individual p orbitals [33, 64, 115]:

$$\begin{aligned}\langle S_{\pm}^{p_x}\rangle &= \mp\frac{\beta^2}{2}[\sin\varphi, \cos\varphi, 0],\\ \langle S_{\pm}^{p_y}\rangle &= \pm\frac{\beta^2}{2}[\sin\varphi, \cos\varphi, 0],\\ \langle S_{\pm}^{p_z}\rangle &= \pm\alpha^2[\sin\varphi, -\cos\varphi, 0],\end{aligned} \tag{5.17}$$

where $\pm$ refers to the upper- and lower-branch of the Dirac cone, respectively. Here we see that the p_x, p_y and p_z orbitals are associated with different spin textures, which are also similar to the results of the full DFT calculations, as shown in Fig. 5.6 [2].

As for the interpretation of experimental ARPES data in this Chapter, as well as the SARPES data presented in the following Chapter 6, we emphasize that the wave function presented in Eq. 5.16 alone is not sufficient to give rise to interference-induced asymmetric intensity pattern, which has been observed in ARPES experiments. Our ab initio DFT calculations indicate that, in order to describe the unusual ARPES data, we need to account for the interference between photoelectrons with different optical path lengths, i.e. a model with at least two atomic layers is required. We construct this by generalizing the wave function of the single-layer system (as described by Eq. 5.16) to a two-layer system. To ensure that the two-layer model has an entangled spin-orbital texture similar to the one obtained by DFT [2] and also by the effective TSS model (Eq. 5.17), the spin-related phase information of each of the individual orbitals are assumed to be layer-independent; however, we note that the details of the $p_{x,y,z}$ orbital superposition in the TSS wave function can be layer-dependent. This way, the wave function of the two-layer model will have a layer-dependent spin-orbital texture, as reported by DFT calculations in realistic materials [2]. Following this strategy, we rewrite the $J = 1/2$ basis states by introducing a layer-dependent orbital character through the coefficients α_i and β_i:

$$\Phi_{\pm\frac{1}{2}} = \sum_{i=1}^{2}\alpha_i|p_z,\uparrow(\downarrow)\rangle \mp \frac{\beta_i}{\sqrt{2}}[|p_x,\downarrow(\uparrow)\rangle \pm \mathrm{i}|p_y,\downarrow(\uparrow)\rangle]. \tag{5.18}$$

We note once again that α_i and β_i are material-determined coefficients, and their value can be estimated with the aid of ab initio DFT calculations. Combining Eq. 5.14 and Eq. 5.18, the two-layer model wave function with a layer-dependent spin-orbital texture can be obtained:

$$\begin{pmatrix}\Psi^{\uparrow}_{\text{model}}\\ \Psi^{\downarrow}_{\text{model}}\end{pmatrix} = \sum_{i=1}^{2}\frac{\alpha_i}{\sqrt{2}}\begin{pmatrix}\pm\mathrm{i}e^{-\mathrm{i}\varphi}\\ 1\end{pmatrix}|p_z\rangle - \frac{\beta_i}{2}\begin{pmatrix}-1\\ \pm\mathrm{i}e^{-\mathrm{i}\varphi}\end{pmatrix}|p_x\rangle + \frac{\beta_i}{2}\begin{pmatrix}-\mathrm{i}\\ \pm e^{-\mathrm{i}\varphi}\end{pmatrix}|p_y\rangle. \tag{5.19}$$

As an example, we study the ARPES intensity based on the experimental geometry using π-polarization, as shown in Section 5.2, Fig. 5.1(a), for the upper Dirac cone states. Considering the selection rules for π-polarization, the photoelectrons are excited only from p_z and p_y orbitals. Following the strategy in Section 5.6.2, but using Eq. 6.3 as the initial state, we can write the photoemission intensity as:

$$\begin{aligned} I \propto & \left|\sum_{\mathrm{i}=1}^{2}\mathrm{i}e^{-\mathrm{i}\varphi}e^{-\mathrm{i}k_z z_i}\frac{\alpha_i}{\sqrt{2}}\tilde{M}_{p_z} - \mathrm{i}e^{-\mathrm{i}k_z z_i}\frac{\beta_i}{2}\tilde{M}_{p_y}\right|^2 \\ & + \left|\sum_{\mathrm{i}=1}^{2}e^{-\mathrm{i}k_z z_i}\frac{\alpha_i}{\sqrt{2}}\tilde{M}_{p_z} + e^{-\mathrm{i}\varphi}e^{-\mathrm{i}k_z z_i}\frac{\beta_i}{2}\tilde{M}_{p_y}\right|^2. \end{aligned} \tag{5.20}$$

Here, $\tilde{M}_{p_{z,y}}$ are matrix elements defined by $\tilde{M}_{p_{z,y}} \equiv \langle e^{\mathbf{i}\mathbf{k}_\parallel\cdot\mathbf{r}_\parallel}|\mathbf{A}\cdot\mathbf{p}|p_{z,y}\rangle$, which are real numbers here, and the two sums on the left and right are the intensity from the up and down spin channels, respectively. The imbalance in ARPES intensity at $\pm\mathbf{k}_\parallel$ is equivalent to the intensity difference between φ and $\varphi+\pi$, which can be calculated from Eq. 5.20:

$$I_{\mathbf{k}_\parallel} - I_{-\mathbf{k}_\parallel} \;\propto\; (\alpha_1\beta_2 - \alpha_2\beta_1)\;\sin(k_z(z_1-z_2))\;\sin(\varphi)\tilde{M}_{p_z}\tilde{M}_{p_y}. \tag{5.21}$$

From this expression for the asymmetry of ARPES intensity between $\pm\mathbf{k}_\parallel$ in π-polarization along emission plane yz, we find that there are three key requirements to get $I_{\mathbf{k}_\parallel} \neq I_{-\mathbf{k}_\parallel}$:

1. an atomic-layer-dependent orbital character, as shown by $(\alpha_1\beta_2$–$\alpha_2\beta_1)$;
2. an out-of-plane phase difference between different atomic layers, from

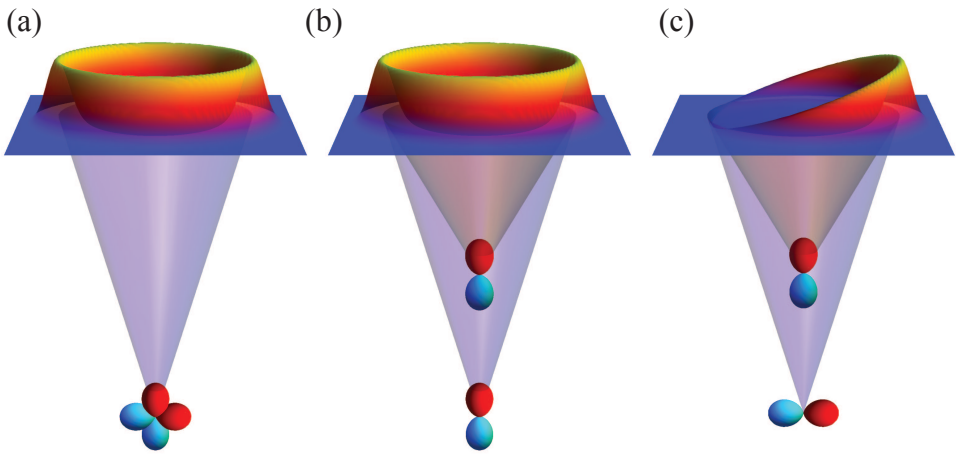

Figure 5.12: Quantum interference effects on ARPES intensity pattern from a simple model described in Eq. 5.21. (a) A monolayer system with multiple orbitals at each atom site. (b) A multiple-layer system with a single type of atom orbital. (c) A multiple-layer system with layer-dependent orbital characters.

$\sin(k_z(z_1-z_2))$; and

3. an in-plane phase difference φ between the p_z and p_y orbitals.

It is by combining these basic aspects with the detailed layer-by-layer description of the spin-orbital texture in Bi_2Se_3 that we can accurately evaluate the photoemission intensity and spin polarization from this real material.

Based on Eq. 5.21, we can simply predict the ARPES intensity pattern for systems with different structures, as shown in Fig. 5.12. For a monolayer system with a single lattice structure, both α_2 and β_2 in Eq. 5.21 are zero. Therefore, we will not expect to observe an asymmetric intensity pattern induced by the quantum interference effect, even if there is one or multiple orbitals at each atom site [Fig. 5.12(a)]. For a system with a minimal two-layered structure, but with only one type of orbital character, the φ in Eq. 5.21 is zero. Again, we will not expect to see any asymmetric intensity pattern that is merely induced by the quantum interference effect [Fig. 5.12(b)]. However, if the system has more than one sub-lattice and

also has multiple orbital characters at each atom site, such as the Bi_2Se_3 system we discuss here, all three requirements listed for Eq. 5.21 are satisfied, and we expect an asymmetric ARPES intensity pattern due to the quantum interference effect [Fig. 5.12(c)]. A similar argument can be extended to understand the ARPES intensity patterns of other systems, such as the surface state of Cu (111) [116] and graphene [117], in which the asymmetric intensity patterns have also been experimentally observed. In particular, the asymmetric ARPES intensity in graphene has attracted a great deal of interest, and the quantum interference effects have also been mentioned, with consideration of graphene's two sub-lattice structures [117–121].

Chapter 6

Photoelectron spin-polarization-control in Bi_2Se_3

We study the manipulation of the photoelectron spin-polarization in Bi_2Se_3 by spin- and angle-resolved photoemission spectroscopy. General rules are established that enable controlling the spin-polarization of photoemitted electrons via light polarization, sample orientation, and photon energy. We demonstrate the $\pm 100\%$ reversal of a single component of the measured spin-polarization vector upon the rotation of light polarization, as well as its full three-dimensional manipulation by varying the experimental configuration and photon energy. While a material-specific DFT analysis is needed for a quantitative description, a minimal phenomenological two-layer model qualitatively accounts for the SARPES response based on the interplay of optical selection rules, photoelectron interference, and the complex internal structure of the topological surface state. It follows that photoelectron spin-polarization control is generic for systems with a layer-dependent, entangled spin-orbital texture.

6.1 Introduction

The central goal in the field of spintronics is to realize highly spin-polarized electron currents and to be able to actively manipulate their spin polarization direction. Topological insulators (TIs), as a new quantum phase of matter with a spin-polarized topologically-protected surface state [7, 24–28],

hold great promise for the development of a controllable 'spin generator' for quantum spintronic applications [122]. A possible avenue is via the spin Hall effect and the spin currents that appear at the boundaries of TI systems, and the electric-field-induced magnetization switching that can be achieved at the interface between a TI and a ferromagnet [30]. In addition, it has been experimentally demonstrated that a spin-polarized photocurrent can be generated from the topological surface state (TSS) of Bi_2Se_3 by using polarized light, suggesting the possibility of exploiting TIs as a material-platform for novel optospintronic devices [113, 123, 124].

All these exciting developments fundamentally rely on the spin properties of the TSS, which have been extensively studied by density functional theory (DFT) [33, 103, 104] and spin- and angle-resolved photoemission spectroscopy (SARPES) [73, 88, 100–102, 125–127]. On the theoretical side, we have shown that the TSS in real materials is not a simple two-dimensional state. Rather, it has a layer-dependent spin-orbital entangled structure – extending over 10 atomic layers ($\sim 2\,\mathrm{nm}$) – challenging the hypothesis of 100% spin-polarization for the TSS Dirac fermions [2]. Our DFT work also suggested a new pathway to control the spin polarization of photoelectrons via photon energy and linear polarization [2]; although this is consistent with some experimental observations by SARPES [125–127], no conclusive understanding of the phenomenon and its governing principles has yet been achieved. This is of critical importance for future applications, and will require a full examination of the photoelectron spin-polarization response in specifically designed SARPES experiments.

In this chapter – guided by a detailed DFT analysis of the TSS entangled spin-orbital texture – we present a systematic SARPES study to elucidate the dependence of the photoelectron spin on light polarization, experimental geometry, and photon energy. We demonstrate a reversal of the spin polarization from -100% to $+100\%$ upon switching from π to σ polarized light. By changing the sample geometry and tuning photon energy we can manipulate the photoelectron spin polarization in three dimensions. While a material-specific DFT analysis is needed for the complete quantitative description, here we introduce a minimal and fully-general phenomenological

two-layer model that qualitatively captures the unusual SARPES response, based on the combined effect of TSS spin-orbital texture, optical selection rules, and photoelectron interference. This paves the way to generating fully controllable spin-polarized photocurrents in TI-based optospintronic devices.

6.2 Experimental methods

SARPES experiments were performed at the Hiroshima Synchrotron Radiation Center (HSRC) on the Efficient SPin REsolved Spectroscopy (ESPRESSO) endstation [128, 129], with 50 meV and $\leq 0.04\,\text{Å}^{-1}$ energy and momentum resolution, respectively. This spectrometer can resolve both in-plane ($P_{x,y}$) and out-of-plane (P_z) photoelectron spin-polarization components. These are obtained from the relative difference between the number of spin-up and spin-down photoelectrons, according to the relation $P_{x,y,z} = (I^{\uparrow x,y,z} - I^{\downarrow x,y,z})/(I^{\uparrow x,y,z} + I^{\downarrow x,y,z})$. Samples were oriented by Laue diffraction and cleaved in-situ at $\sim 7 \times 10^{-11}$ torr; all measurements were performed at 30 K once the surface evolution had mostly stabilized [1], using 21 eV photons unless otherwise specified.

6.3 SARPES results and discussion

In Bi_2Se_3, the TSS wavefunction is composed of both in-plane ($p_{x,y}$) and out-of-plane (p_z) orbitals. As a consequence of spin-orbit coupling, the spin texture associated with each orbital is remarkably different, and has been referred to as *entangled spin-orbital texture* [2, 115]. In Fig. 6.1, we sketch the orbital-dependent in-plane spin polarization of the upper-branch Dirac fermions (with the out-of-plane spin component neglected). We see that the well-known TSS chiral spin texture is actually derived only from the out-of-plane p_z orbitals [Fig. 6.1(c)]; instead, the individual p_x and p_y spin configurations are not chiral[14], and are also opposite to one another [Figs. 6.1(a)

[14]The *total* in-plane orbital states do instead possess a chiral spin texture, with helicity dependent on the details of the linear combination of p_x and p_y orbitals [2].

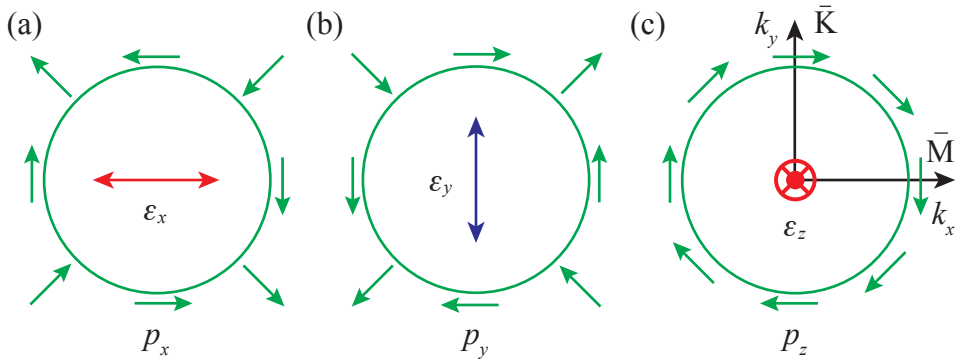

Figure 6.1: Spin orientation of the TSS in Bi_2Se_3. (a)–(c) In-plane spin texture as obtained separately for the p_x (a), p_y (b), and p_z (c) orbital contributions to the topological surface state (TSS). Red/blue arrows indicate the light electric field (π/σ polarization) that must be used to excite photoelectrons from each of the individual orbitals, according to the electric dipole selection rules.

and 6.1(b)]. By comparing the spin orientation of in-plane and out-of-plane orbitals, we learn that they can be parallel, anti-parallel, or even perpendicular to each other, in dependence of the specific momentum-space location. For example, p_x and p_z spin polarizations are parallel along the $\bar{\Gamma}-\bar{M}$ direction (i.e., the k_x axis), but antiparallel along $\bar{\Gamma}-\bar{K}$ (i.e., the k_y axis). As for probing these different orbital-dependent configurations, we note that – based on the ARPES optical selection rules – photoelectrons are emitted from a given $p_{x,y,z}$ orbital if the photon electric field has a non-zero component $\varepsilon_{x,y,z}$ along the corresponding direction [130]. Thus, using linearly polarized photons with electric field parallel to the $k_x/k_y/k_z$ directions, we can probe the $p_x/p_y/p_z$ spin textures individually in SARPES (Fig. 6.1).

Fig. 6.2 demonstrates the $\pm 100\%$ manipulation of photoelectron spin-polarization upon switching the light polarization from π to σ in SARPES. When we measure the energy distribution curve (EDC) at $k_x = 0.07\,\text{Å}^{-1}$ with π polarization [photon electric field in the xz plane, as in Figs. 6.2(a,b)], we observe a peak only in the spin-down y-channel at the TSS upper-branch binding energy at $\sim 0.1\,\text{eV}$ [green curve in the top panel of Fig. 6.2(c)]. Thus

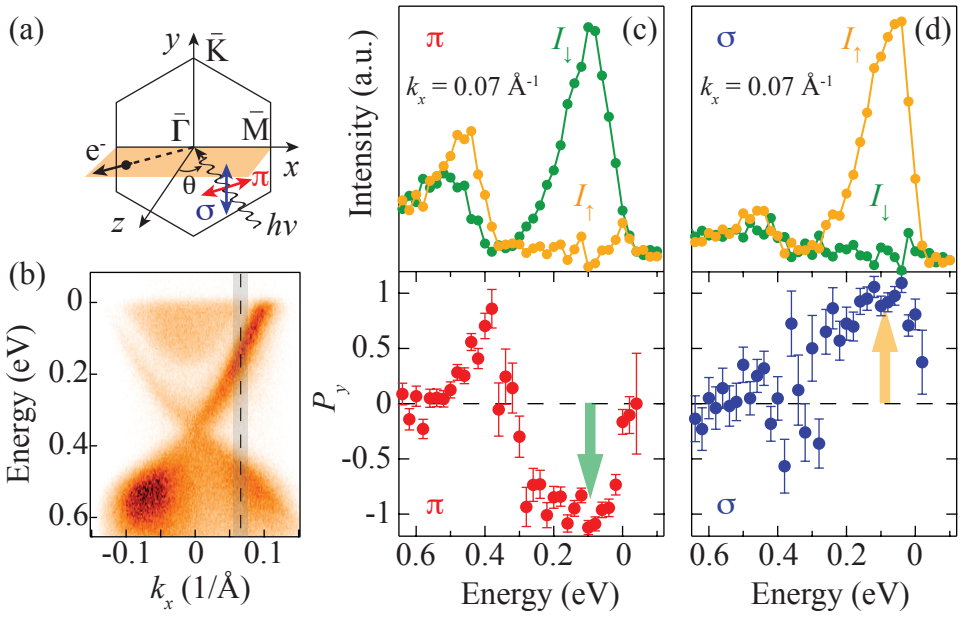

Figure 6.2: Light-polarization-controlled photoelectron spin polarization. (a) Schematics of the experimental geometry, with π (horizontal) and σ (vertical) linear polarization also indicated. (b) ARPES dispersion of TSS Dirac fermions measured along the $\bar{M}-\bar{\Gamma}-\bar{M}$ direction with π polarization. (c) The top panel shows SARPES EDCs, with spin quantization axis along the y direction, measured with π polarization along the gray-bar highlighted in (b); the corresponding spin polarization curve P_y is shown in the lower panel (the TSS is located at 0.1 eV in this data taken at $k_x = 0.07\,\text{Å}^{-1}$). (d) SARPES data analogous to those in (c), now measured with σ polarization.

we obtain $P_{x,z} \simeq 0$ and remarkably $P_y \simeq -100\%$ for the spin-polarization vector components, as highlighted in the bottom panel of Fig. 6.2(c) by the green arrow at 0.1 eV (note that the positive P_y value at $\sim$0.4 eV originates from the TSS bottom branch and its reversed spin helicity [2, 115]). Most importantly, when light polarization is switched from π to σ, while $P_{x,z}$ remain zero P_y suddenly becomes $+100\%$ at 0.1 eV, as shown in Fig. 6.2(d).

We note that a spin polarization as high as $\pm 100\%$ is rarely reported in previous SARPES studies of Bi_2Se_3 [73, 88, 100–102, 125]; this is achieved in this study owing to the high efficiency of the spin polarimeter and the perfect alignment within the photoelectron emission plane of both the light polarization and sample $\bar{\Gamma}-\bar{M}$ direction, which eliminates the interference-induced deviations to be discussed below. In Fig. 6.2 we outline how the experimental configuration and the entangled spin-orbital texture (Fig. 6.1) lead to spin-polarization switching: π polarization excites photoelectrons from p_x and p_z orbitals only, both of which are -100% spin polarized along y for all positive '$+k_x$' locations [Figs. 6.1(a,c)]; this gives $P_y \equiv -100\%$ in SARPES, consistent with the experiment in Fig. 6.2(c). On the contrary, in σ polarization photoelectrons originate only from the p_y orbitals, which at $+k_x$ locations are $+100\%$ spin-polarized along the y direction, i.e. $P_y \equiv +100\%$ as detected in Fig. 6.2(d).

By rotating light polarization between σ and π, we would observe a continuous change of P_y between $\pm 100\%$, as experimentally verified by Jozwiak et al. [125]. However, here we argue that the manipulation of the photoelectron spin polarization by light stems from the TSS orbital-dependent spin texture combined with optical selection rules, rather than being due to the relativistic photon-electron interaction [105, 125] which is generally a weak perturbation compared to the non-relativistic electric-dipole term. The SARPES response is indeed most unusual for configurations different from the one in Fig. 6.2(a) – which is unique in that electrons photoemitted by either π or σ light all have the same spin polarization even if originating from multiple orbitals. This is shown in Figs. 6.3(c–e) where we examine the photoelectron spin polarization at the same $+k_x$ point[15], for the two

[15] In this experiment, performed along the $\bar{\Gamma}-\bar{M}$ direction at $|k_x| = 0.04\,\text{Å}^{-1}$, the TSS

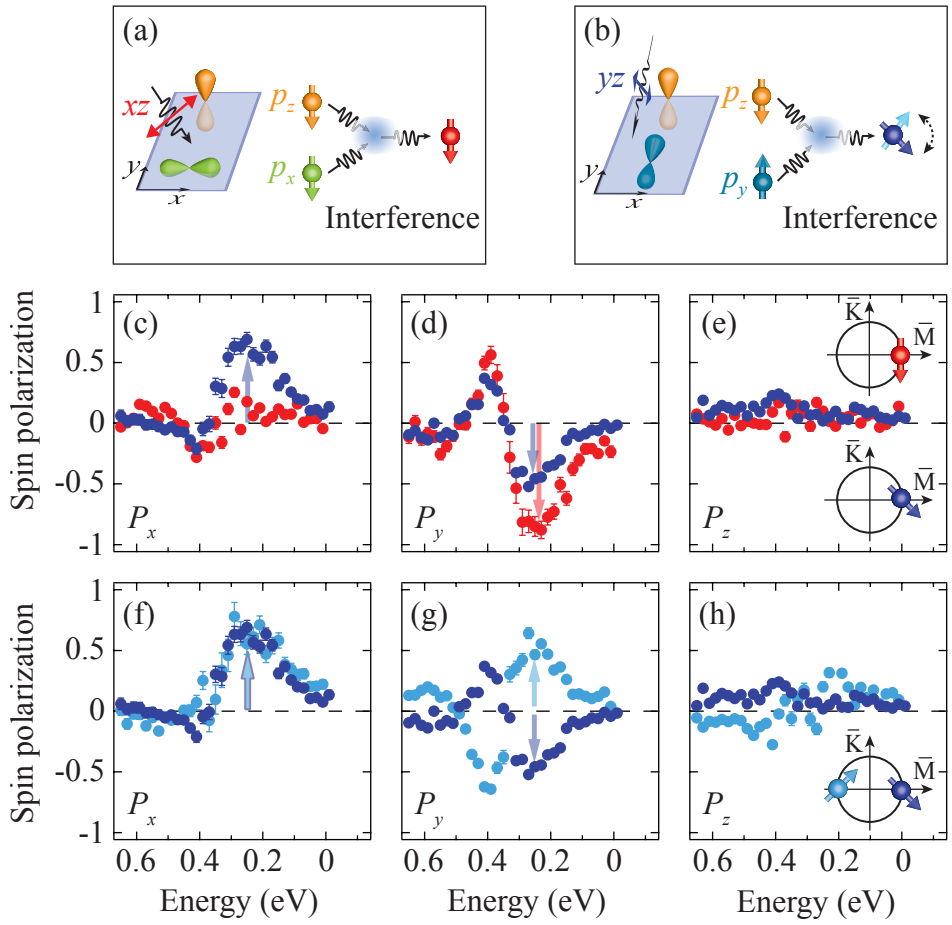

Figure 6.3: Quantum interference effects on spin polarization of photoelectrons. (a),(b) Schematics of photoelectron interference effects for two experimental configurations: (a) π-polarization incident in the xz plane probes p_x and p_z orbitals with the same spin state (see also Fig. 6.1); (b) when incident in the yz plane, π-polarization probes p_y and p_z orbitals with opposite spin states (Fig. 6.1). (c)–(e) Spin polarization curves at the $+k_x$ point as sketched in (e), measured for (a)/(b) configurations (red/blue curves). (f)–(h) Spin polarization curves at $\pm k_x$ as sketched in (h) for the (b) configuration. Note that the TSS is located at 0.25 eV in this data measured at $|k_x| = 0.04\,\text{Å}^{-1}$.

configurations of Figs. 6.3(a,b). *Case I* – $\boldsymbol{\varepsilon} \parallel xz$: photoelectrons are emitted from $p_{x,z}$ orbitals in the same spin state [Fig. 6.3(a)], and as before we observe a close to -100% P_y[16] and zero $P_{x,z}$ [red symbols in Figs. 6.3(c–e)]. *Case II* – $\boldsymbol{\varepsilon} \parallel yz$: photoelectrons are emitted from $p_{y,z}$ orbitals with mixed spin states [Fig. 6.3(b)], and are no longer fully polarized along P_y. Instead P_y decreases and an unexpected $P_x \simeq 74\%$ appears [blue symbols in Figs. 6.3(c-e) and sketch in 6.3(e)]. Another interesting aspect is that while both P_y and P_z[17] switch sign at opposite momenta $\pm k_x$, as expected from time-reversal symmetry [Figs. 6.3(g,h)], the P_x retains the same value [Figs. 6.3(f) and sketch in 6.3(h)].

To understand the unexpected results of Fig. 6.3 – seemingly inconsistent with the TSS time-reversal invariance – we need to consider photoelectron-interference effects specific for SARPES. To this end, we express the measured spin polarization vector $\vec{P}$ in terms of the expectation value of generalized spin operators[18]:

$$P_\eta = \frac{\sum_{i,\tau} \langle S_\eta^{i,\tau;\, i,\tau} \rangle |M_{i,\tau}|^2}{I_{total}} + \frac{\sum_{i \neq i',\, \tau \neq \tau'} \langle S_\eta^{i,\tau;\, i',\tau'} \rangle \, e^{\mathrm{i}k_z(z_i - z_{i'})} M_{i,\tau}^* M_{i',\tau'}}{I_{total}}, \tag{6.1}$$

where $\eta \in \{x, y, z\}$, $\tau \in \{p_x, p_y, p_z\}$, i is the atomic-layer index (the TSS layer-dependent structure is a key factor here [2]); $M_{i,\tau} \propto \langle e^{\mathrm{i}\mathbf{k}_\parallel \cdot \mathbf{r}_\parallel} | \mathbf{A} \cdot \mathbf{p} | \psi_{i,\tau} \rangle$ is the matrix element of the optical transition between an atomic wavefunction of orbital τ centered around the atomic layer i and a free-electron final state; the k_z part of the latter has been factorized in the phase term $e^{\mathrm{i}k_z(z_i - z_{i'})}$, which accounts for the optical path difference for photoelectrons from different layers; and I_{total} is the sum of intensity from spin-up and spin-down channels. The generalized spin operator in the expectation value $\langle S_\eta^{i,\tau;\, i',\tau'} \rangle$ is defined as:

$$S_\eta^{i,\tau;\, i',\tau'} = |\psi_{i,\tau}\rangle\langle\psi_{i',\tau'}| \sigma_\eta, \tag{6.2}$$

is located at 0.25 eV below E_F (or, equivalently, at 0.1 eV above the Dirac point).

[16] The slight reduction from $P_y = -100\%$ measured initially is due to the sample surface degradation during the three continuous days of experiments after cleaving.

[17] Although $P_z = 0$ for the TSS upper branch, the sign change of P_z can be observed for the TSS lower branch.

[18] See Section 5.6.3 for the derivation of Eq. 6.1.

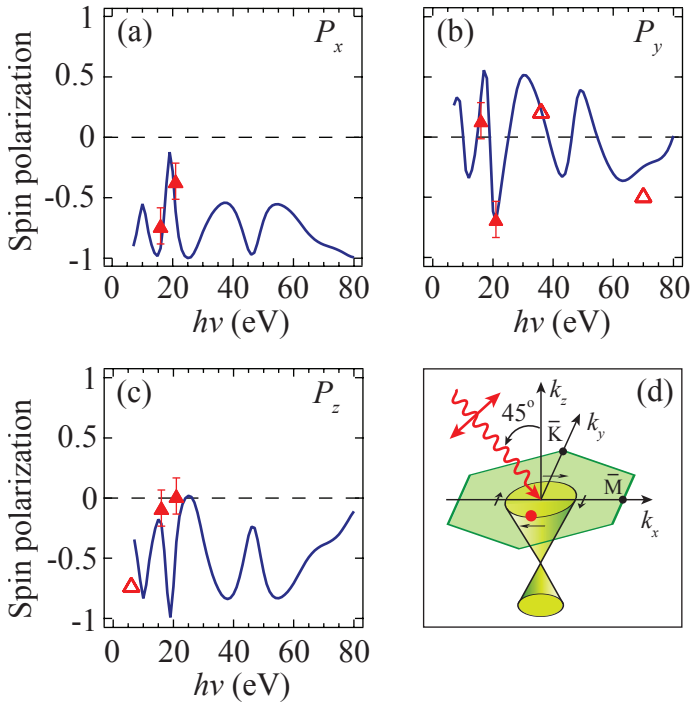

Figure 6.4: Photon-energy-dependent spin polarization of photoelectrons. (a)–(c) Solid blue lines: calculated photon-energy-dependence of the photoelectron spin-polarization-vector components, as obtained at the $-k_y$ point for π-polarized light incident in the xz plane as shown in the sketch in (d). The solid red triangular symbols are SARPES data from this work; the open red triangles are from Ref.[102, 125].

where $\sigma_{x,y,z}$ are the Pauli spin matrices. The crucial point is that in Eq. 6.1 the $i \neq i'$, $\tau \neq \tau'$ *off-diagonal terms account for the interference effects.* If the initial states $\psi_{i,\tau}$ and $\psi_{i',\tau'}$ being probed all have the same spin expectation value, then $\langle S_\eta^{i,\tau;i,\tau}\rangle = \langle S_\eta^{i,\tau;i',\tau'}\rangle$ and $P_\eta = 100\%$ for the η component corresponding to the spin quantization axis, as in *Case I* of Fig. 6.3(a). However, when the initial states being simultaneously probed have different spin states, as in *Case II* of Fig. 6.3(b), non-trivial effects should be expected for the measured spin polarization due to the contribution of the $S_\eta^{i,\tau;i',\tau'}$ interference term.

To qualitatively demonstrate that Eq. 6.1 describes the SARPES results

in Fig. 6.3, in Section 6.4 we generalize the effective single-layer TSS wave function derived by Zhang *et al.* [33, 64, 115] into a two-layer one for $p_{x,y,z}$ orbitals, as the minimal model-wave function needed to capture interference effects[19]. For the upper branch of the Dirac-cone this becomes:

$$\Psi = \sum_{i=1}^{2} \frac{\alpha_i}{\sqrt{2}} \begin{pmatrix} \mathrm{i}e^{-\mathrm{i}\varphi} \\ 1 \end{pmatrix} |p_z\rangle - \frac{\beta_i}{2} \begin{pmatrix} -1 \\ \mathrm{i}e^{-\mathrm{i}\varphi} \end{pmatrix} |p_x\rangle + \frac{\beta_i}{2} \begin{pmatrix} -\mathrm{i} \\ e^{-\mathrm{i}\varphi} \end{pmatrix} |p_y\rangle, \tag{6.3}$$

where α_i and β_i are layer-dependent coefficients, and the in-plane phase φ (defined as the angle between $\mathbf{k}$ and the $+k_x$ direction) reproduces the orbital-dependent spin texture shown in Fig. 6.1. To further simplify the problem we assume – without loss of generality – that $\alpha_1 = \beta_2 = 0$, $\alpha_2 = \sqrt{3/2}$, and $\beta_1 = 1/\sqrt{2}$; this choice matches the 1:3 overall in-plane/out-of-plane orbital weight ratio calculated by DFT for Bi_3Se_2 [2]. Then, for $\boldsymbol{\varepsilon} \| yz$ (*Case II*), the initial-state components being probed reduce to:

$$\Psi_{p_z} = \frac{\sqrt{3}}{2} \begin{pmatrix} \mathrm{i}e^{-\mathrm{i}\varphi} \\ 1 \end{pmatrix} \text{ and } \Psi_{p_y} = \frac{\sqrt{2}}{4} \begin{pmatrix} -\mathrm{i} \\ e^{-\mathrm{i}\varphi} \end{pmatrix}. \tag{6.4}$$

At $\pm k_x$ ($\phi = 0$ and π, respectively), the intrinsic spin polarization is $\mp 100\%$ ($\pm 100\%$) along the k_y direction for the p_z (p_y) orbital, as in Fig. 6.1. By means of Eq. 6.1, we can now calculate the photoelectron spin-polarization vector $\vec{P}$ as seen at $\pm k_x$ in SARPES, obtaining:

$$\vec{P}(\pm k_x) \propto (\sin\theta_{k_z}, \mp 0.6, \mp\cos\theta_{k_z}), \tag{6.5}$$

where $\theta_{k_z} = k_z(z_1 - z_2)$. We see that, although the spin polarization of each individual initial state is purely along y, the photoelectron spin polarization can have non-zero components along x and/or z, if $z_1 - z_2 \neq 0$. This highlights the need for a minimal two-atomic-layer model. Also note that the explicit presence of k_z leads to photon-energy-dependence (more below), and all $P_{x,y,z}$ components oscillate sinusoidally with different phases, upon varying k_z ; this is responsible for the maximal P_x and minimal P_z in Figs. 6.3(f)–(h).

[19] Details are shown in Section 6.4.

Finally, Eq. 6.5 confirms the fact that only P_y and P_z components reverse their signs, while P_x retains the same value at $\pm k_x$, again as observed in our SARPES data in Figs. 6.3(f)–(h).

While our two-layer model reproduces the SARPES results qualitatively, we stress that the quantitative description must be based on the complete ∼10-layer TSS wave function obtained for Bi_2Se_3 by DFT [2]. To this end, in Fig. 6.4 we present the photon-energy-dependence of the photoelectron spin polarization at $-k_y$, for $\boldsymbol{\varepsilon} \| xz$. We find good agreement between our DFT-based results and SARPES data from this and published work [102, 125], conclusively demonstrating that the photon-energy-controlled photoelectron spin polarization stems from interference effects acting in concert with the TSS layer-dependent spin-orbital texture.

6.4 A two-layer model to describe interference effects in SARPES

In Section 5.6.6, we constructed a two-layer model based on the effective Hamiltonian of the TSS to demonstrate the asymmetric ARPES intensity. Here we use the same two-layer-model wave function (Eq. 6.3) to qualitatively show that quantum interference effects can allow a manipulation of photoelectron spin polarization in SARPES experiments. We take the experiment in Figs. 6.3(f)–(h) as an example, where the spin polarization was measured at both $\pm k_x$ positions with π-polarized light incident in the yz plane. Since π polarization incident in the yz plane would only excite photoelectrons from the p_y and p_z orbitals, the initial state wave function of the TSS upper-branch can be reduced to the p_y and p_z terms in Eq. 6.3, and can thus be rewritten as:

$$\begin{pmatrix} \Psi^{\uparrow}_{\text{initial}} \\ \Psi^{\downarrow}_{\text{initial}} \end{pmatrix} = \sum_{i=1}^{2} \frac{\alpha_i}{\sqrt{2}} \begin{pmatrix} \mathrm{i}e^{-\mathrm{i}\varphi} \\ 1 \end{pmatrix} |p_z\rangle + \frac{\beta_i}{2} \begin{pmatrix} -\mathrm{i} \\ e^{-\mathrm{i}\varphi} \end{pmatrix} |p_y\rangle, \tag{6.6}$$

where α_i and β_i represent the layer-dependent orbital characters. At the $+k_x$ point, $\varphi = 0$, we calculate the measured spin polarization of photoelectrons

by using Eq. 6.1 and Eq. 6.6:

$$\begin{aligned} P_x &= \frac{2(\alpha_2\beta_1 - \alpha_1\beta_2)\sin(k_z z_1 - k_z z_2) M_{p_y} M_{p_z}}{I_{total}}, \\ P_y &= \frac{(\beta_1^2 + \beta_2^2) M_{p_y}^2 - (\alpha_1^2 + \alpha_2^2) M_{p_z}^2}{I_{total}} \\ &\quad + \frac{2(\beta_1\beta_2 - \alpha_1\alpha_2)\cos(k_z z_1 - k_z z_2) M_{p_y} M_{p_z}}{I_{total}}, \\ P_z &= -\frac{2(\alpha_1\beta_1 + \alpha_2\beta_2) + 2(\alpha_2\beta_1 - \alpha_1\beta_2)\cos(k_z z_1 - k_z z_2)}{I_{total}} M_{p_y} M_{p_z}. \end{aligned} \tag{6.7}$$

We can see that although the initial state is fully spin polarized along the y direction, with a value of 100% for the p_y orbital and -100% for the p_z orbital (Eq. 5.17), the photoelectron spin polarization measured by SARPES can have non-zero components along the x and/or z direction, as long as $\alpha_1 \neq \alpha_2$, $\beta_1 \neq \beta_2$, and $z_1 \neq z_2$. Also, all the components of the photoelectron spin polarization can be controlled by tuning the photon energy ($h\nu$) because we have $k_z = \sqrt{\frac{2m_e}{\hbar^2}(h\nu - E_B) - k_x^2 - k_y^2}$, with E_B being the binding energy.

Similarly, for the $-k_x$ point, $\varphi = \pi$, we obtain the photoelectron spin polarization:

$$\begin{aligned} P_x &= \frac{2(\alpha_2\beta_1 - \alpha_1\beta_2)\sin(k_z z_1 - k_z z_2) M_{p_y} M_{p_z}}{I_{total}}, \\ P_y &= -\frac{(\beta_1^2 + \beta_2^2) M_{p_y}^2 - (\alpha_1^2 + \alpha_2^2) M_{p_z}^2}{I_{total}} \\ &\quad - \frac{2(\beta_1\beta_2 - \alpha_1\alpha_2)\cos(k_z z_1 - k_z z_2) M_{p_y} M_{p_z}}{I_{total}}, \\ P_z &= \frac{2(\alpha_1\beta_1 + \alpha_2\beta_2) + 2(\alpha_2\beta_1 - \alpha_1\beta_2)\cos(k_z z_1 - k_z z_2)}{I_{total}} M_{p_y} M_{p_z}. \end{aligned} \tag{6.8}$$

Comparing Eq. 6.7 to Eq. 6.8, we find that both P_y and P_z change their signs when moving from $+k_x$ to $-k_x$; on the contrary, P_x maintains the same value, consistent with our SARPES data shown in Figs. 6.3(f)–(h).

These model results demonstrate that a layer-dependent entangled spin-orbital texture is key to observe and manipulate the photoelectron spin polarization in SARPES experiments (as shown in Fig. 6.3 and Fig. 6.4).

At variance with the observed behavior – for single atomic-layer model – all the results would be photon-energy independent because the k_z term in Eq. 6.7 and Eq. 6.8 vanishes when $z_1 - z_2 = 0$; in addition – for systems with layer-independent orbital character – also the value of the $(\alpha_2\beta_1 - \alpha_1\beta_2)$ term becomes zero leading to a constant photoelectron spin polarization in Eq. 6.7 and Eq. 6.8.

In Section 6.3, we chose a simpler situation to illustrate the effects of interference on the photoelectron spin polarization. This simplified situation is obtained by using these parameters: $\alpha_1 = 0$, $\beta_1 = 1/\sqrt{2}$, $\alpha_2 = \sqrt{3/2}$, and $\beta_2 = 0$, and also by assuming $M_{p_y} = M_{p_z}$.

6.5 Conclusion

In this chapter, we have explained the underlying mechanism of the manipulation of photoelectron spin polarization in TIs, as a consequence of the TSS entangled spin-orbital texture, optical selection rules, and quantum interference. This is responsible also for the significantly different ARPES intensities observed at $\pm k_x$ in Fig. 6.2(b), which implies that a net spin-polarized current can be photoinduced by linearly polarized light [113]. Thus, our SARPES study demonstrates how to generate a spin-polarized photocurrent in Bi_2Se_3 and manipulate its absolute spin polarization by linearly polarized light, a key step in TI-based optospintronics. We argue that all these phenomena could be valid in other spin-orbit coupled systems, as long as the initial states are characterized by a layer-dependent entangled spin-orbital texture.

Chapter 7

Conclusion

This thesis presented systematic work on Bi_2Se_3 and Bi_2Te_3, materials that have been referred to as the hydrogen atom of three-dimensional topological insulators (TIs). Using angle-resolved photoemission spectroscopy (ARPES), spin-resolved ARPES (SARPES), and density functional theory (DFT) calculations, various topics have been studied, ranging from TI material problems and engineering surface electronic structures, to the fundamental physics of realistic surface states and their possible applications in spintronics. In regards to the technical aspect, this thesis presented an example of a tight combination of experimental and theoretical work. The power of this combination allowed us to gain significant insights into the fundamental principles of the systems we were studying. Here we will recapitulate the main conclusions and their context.

Rashba spin-splitting control at the surface of Bi_2Se_3

The material problem is an obstacle to further advance topological-insulator-based devices. Bi_2Se_3, known as a prototypical TI candidate, does not have a truly insulated bulk – due to the unintentional and uncontrolled doping that leads to a Fermi level crossing the bulk conduction band rather than staying inside the bulk gap. Another critical material problem is the unstable surface of the crystal, even in ultra-high vacuums. One approach to reset the chemical potential of materials is via doping, which is also related to another important question about surface or bulk impurity effects on the surface electronic structure. Because of the polarized spin texture of the topological surface state (TSS), no back-scattering is allowed, and the surface state is expected to be immune to localized weak disorders, as long

as the time-reversal symmetry (TRS) of the system is preserved.

Our first experiment was to investigate the effect of surface impurities on TSS by in situ potassium deposition on the surface of Bi_2Se_3. We have systematically studied the ARPES evolution of the surface electronic structure as a function of potassium evaporation. The deposition of submonolayers of potassium allows us to stabilize the otherwise continuously evolving surface carrier concentration. Thus, our approach provides a technique to overcome the problem of general instability and self-doping at the surface of TIs.

On the other hand, the potassium deposition leads to a more uniform surface electronic structure, in which well-defined Rashba-like states emerge from the continuum of parabolic-like states that characterizes the as-cleaved, disordered surfaces. The spin splitting of Rashba-like states can be controlled by the amount of potassium deposition, and the entire process is reversible by tuning the temperatures. These results suggest that TIs can be a platform to host and manipulate the coexistence of non-trivial spin splitting states (TSS) and conventional spin splitting states (Rashba type), both of which are substantially important for spintronic applications. Our DFT slab calculations reveal that the new spin-split states originate from the bulk-like quantum well states of a five-quintuple-layer slab, as a consequence of the K-enhanced inversion symmetry breaking already present for the pristine surface.

This work is one of the earliest studies on engineering the surface electronic structures of TIs. The demonstration of generating and precisely controlling a large energy-scale spin splitting shows a promising avenue for the future development of TI-based spintronic devices.

Tailoring spin-orbit coupling in Mn-doped $\mathbf{Bi_{2-x}Mn_xTe_3}$

The beauty of TIs is in its spin-polarized TSS and its topological protection. The latter is valid under the condition that the system has TRS. Breaking TRS therefore becomes a way to switch on and off the topological protections, and can be achieved by applying an external magnetic field or by the magnetic moment of impurities. Doping TIs with magnetic impurities has

been viewed as an efficient way to break the TRS by forming long-range magnetic orders. ARPES can be one of the most direct methods to monitor the TRS breaking effects, such as by looking for an opening gap at the Dirac point of the TSS spectra.

We investigated magnetically doped $Bi_{2-x}Mn_xTe_3$ to observe a response in the TSS spectra to the development of ferromagnetic order at low temperatures. Instead of focusing on the gap opening at the Dirac point, we raised another fundamental question about how impurities affect the spin-orbit coupling (SOC) of the systems, a critical parameter to sustain the appearance of TSS. The size of the bulk gap shows a strong dependence of Mn doping levels, even below 5%. Our ab initio tight-binding (TB) model calculations show that the bulk energy gap size is directly linked to the strength of the SOC in the system. Therefore, our observation indicates that although the Mn concentration is low (only 2-5%), the effective content of impurities can be ∼4 times higher. More importantly, through diluting the SOC of the system, impurities can turn a topological insulator into a trivial insulator even at a low concentration.

A temperature-dependent study crossing the ferromagnetic transition $T_c = 12\,\mathrm{K}$ suggests a surprising result that the ferromagnetic order might be of a short range. This raises a question regarding TRS behaviour in a TI system where the magnetic order is of short range. Further theoretical investigations are required to address this question.

Layer-by-layer entangled spin-orbital texture in Bi_2Se_3

In this work, we address one of the most fundamental outstanding questions in the field of TIs: What is the degree of spin polarization of Dirac fermions in real TI materials? In phenomenological models, a 100% spin polarization is assumed for TSS. DFT calculations indicate that the TSS spin polarization of the Bi_2X_3 material family ($X = \mathrm{Se}$, Te) can be substantially reduced from 100%. Extensive SARPES studies also have attempted to answer this question. However, the large discrepancy in the degree of spin polarization determined from the TSS by SARPES - ranging from 20 to 85% - challenges

all the theoretical predictions. Thus, this question has become a puzzle and undermines the applicability of real TIs in spintronic devices.

By a combination of polarization-dependent ARPES and DFT slab calculations, we are the first to explicitly solve this puzzle. We have found that the surface state Dirac fermions in Bi_2Se_3 are characterized by a layer-dependent entangled spin-orbital texture, which becomes apparent through quantum interference effects. Quantum interference between photoelectrons not only affects the measured ARPES intensity but also, and more importantly, causes disagreement between the measured spin polarization and the intrinsic spin texture of TSS. We have theoretically demonstrated how the light polarization, photon energy, and experimental setup can affect the spin polarization of photoelectrons. We also proposed how to probe the intrinsic spin texture of TSS and suggested a way to continuously manipulate the spin polarization of photoelectrons all the way from 0 to $\pm 100\%$ by an appropriate choice of photon energy, linear polarization, and angle of incidence. These discoveries are key to the understanding and exploitation of TIs.

To accomplish this work, we developed an ab initio slab TB model and implemented spin-resolved photoemission intensity calculations. These calculations involve very technical details and are not typically performed in the ARPES community; however, we think the generic value of the method can benefit future ARPES studies in other spin-orbit coupled systems. For this reason, we devote Chapter 2, Chapter 3, and Section 5.6 in Chapter 5 to all the details about how to construct ab initio TB models and use them to calculate ARPES and SARPES data.

Photoelectron spin-polarization-control in Bi_2Se_3

The goal of this SARPES work is to experimentally unveil the layer-by-layer entangled spin-orbital texture of the TSS in Bi_2Se_3. As predicted by our theoretical calculations, the entangled spin-orbital texture results in a strong photoelectron interference effect, which deviates the measured spin polarization of photoelectrons from the intrinsic spin polarization of the TSS, and therefore provides us with a unique opportunity to manipulate the

spin polarization of photoelectrons. The manipulation of photoelectron spin polarization challenges the basic assumption of spin conservation commonly used in SARPES, but at the same time opens a new possibility to advance TI applications in opto-spintronics.

Our SARPES data has successfully demonstrated a generic rule for manipulating photoelectron spin polarization. We have shown that the spin polarization of photoelectrons can be flipped between $\pm 100\%$ and also rotated in three dimensions with an appropriate choice of linear light polarization and photon energy. The underlying principle of manipulating spin polarization is to selectively excite photoelectrons from orbitals that have different spin orientations, which can be provided by an initial state with an entangled spin-orbital texture. Quantum interference between photoelectrons is a key mechanism to achieve three-dimensional manipulation and also generate spin-polarized photocurrents or even pure spin currents. From the application point of view, this work paves a new way towards the long-term goal of utilizing topological insulators for spintronics by using light control.

Bibliography

[1] Z.-H. Zhu, G. Levy, B. Ludbrook, C. N. Veenstra, J. A. Rosen, R. Comin, D. Wong, P. Dosanjh, A. Ubaldini, P. Syers, N. P. Butch, J. Paglione, I. S. Elfimov, and A. Damascelli, "Rashba spin-splitting control at the surface of the topological insulator Bi_2Se_3," *Phys. Rev. Lett.*, vol. 107, p. 186405, 2011.

[2] Z.-H. Zhu, C. N. Veenstra, G. Levy, A. Ubaldini, P. Syers, N. P. Butch, J. Paglione, M. W. Haverkort, I. S. Elfimov, and A. Damascelli, "Layer-by-layer entangled spin-orbital texture of the topological surface state in Bi_2Se_3," *Phys. Rev. Lett.*, vol. 110, p. 216401, 2013.

[3] J. Jackson in *Classical electrodynamics*, John Wiley & Sons, 1999.

[4] J. Sakurai in *Advanced quantum mechanics*, Reading, MA: Addison-Wesley, 1967.

[5] G. Dresselhaus, "Spin-orbit coupling effects in zinc blende structures," *Phys. Rev.*, vol. 100, pp. 580–586, 1955.

[6] R. H. Parmenter, "Symmetry properties of the energy bands of the zinc blende structure," *Phys. Rev.*, vol. 100, pp. 573–579, 1955.

[7] M. Hasan and C. Kane, "Colloquium: topological insulators," *Rev. Mod. Phys.*, vol. 82, pp. 3045–3067, 2010.

[8] X.-L. Qi and S.-C. Zhang, "Topological insulators and superconductors," *Rev. Mod. Phys.*, vol. 83, pp. 1057–1110, 2011.

[9] B. J. Kim, H. Jin, S. J. Moon, J.-Y. Kim, B.-G. Park, C. S. Leem, J. Yu, T. W. Noh, C. Kim, S.-J. Oh, J.-H. Park, V. Durairaj, G. Cao,

and E. Rotenberg, "Novel $J_{\text{eff}} = 1/2$ mott state induced by relativistic spin-orbit coupling in Sr_2IrO_4," *Phys. Rev. Lett.*, vol. 101, p. 076402, 2008.

[10] B. J. Kim, H. Ohsumi, T. Komesu, S. Sakai, T. Morita, H. Takagi, and T. Arima, "Phase-sensitive observation of a spin-orbital mott state in Sr_2IrO_4," *Science*, vol. 323, pp. 1329–1332, 2009.

[11] M. W. Haverkort, I. S. Elfimov, L. H. Tjeng, G. A. Sawatzky, and A. Damascelli, "Strong spin-orbit coupling effects on the fermi surface of Sr_2RuO_4 and Sr_2RhO_4," *Phys. Rev. Lett.*, vol. 101, p. 026406, 2008.

[12] G.-Q. Liu, V. N. Antonov, O. Jepsen, and O. K. Andersen., "Coulomb-enhanced spin-orbit splitting: The missing piece in the Sr_2RhO_4 puzzle," *Phys. Rev. Lett.*, vol. 101, p. 026408, 2008.

[13] C.N.Veenstra, Z.-H.Zhu, M.Raichle, B.M.Ludbrook, A.Nicolaou, B.Slomski, G.Landolt, S.Kittaka, Y.Maeno, J.H.Dil, I.S.Elfimov, M.W.Haverkort, and A.Damascelli, "Observation of strong spin-orbital entanglement in Sr_2RuO_4 by spin-resolved ARPES," *arXiv e-prints, 1303.5444*, 2013.

[14] C. N. Veenstra, Z.-H. Zhu, B. Ludbrook, M. Capsoni, G. Levy, A. Nicolaou, J. A. Rosen, R. Comin, S. Kittaka, Y. Maeno, I. S. Elfimov, and A. Damascelli, "Determining the Surface-To-Bulk Progression in the Normal-State Electronic Structure of Sr_2RuO_4 by Angle-Resolved Photoemission and Density Functional Theory," *Phys. Rev. Lett.*, vol. 110, p. 097004, 2013.

[15] Y. A. Bychkov and E. I. Rashba, "Oscillatory effects and the magnetic susceptibility of carriers in inversion layers," *J. Phys. C*, vol. 17, p. 6039, 1984.

[16] L. Meier, G. Salis, I. Shorubalko, E. Gini, S. Schön, and K. Ensslin, "Measurement of Rashba and Dresselhaus spin-orbit magnetic fields," *Nature Phys.*, vol. 3, no. 9, pp. 650–654, 2007.

[17] S. LaShell, B. McDougall, and E. Jensen, "Spin splitting of an Au(111) surface state band observed with angle resolved photoelectron spectroscopy," *Phys. Rev. Lett.*, vol. 77, p. 3419, 1996.

[18] C. R. Ast, J. Henk, A. Ernst, L. Moreschini, M. C. Falub, D. Pacilé, P. Bruno, K. Kern, and M. Grioni, "Giant spin splitting through surface alloying," *Phys. Rev. Lett.*, vol. 98, p. 186807, 2007.

[19] J. Nitta, T. Akazaki, H. Takayanagi, and T. Enoki, "Gate control of spin-orbit interaction in an inverted $In_{0.53}Ga_{0.47}As/In_{0.52}Al_{0.48}As$ heterostructure," *Phys. Rev. Lett.*, vol. 78, pp. 1335–1338, 1997.

[20] Y. M. Koroteev, G. Bihlmayer, J. E. Gayone, E. V. Chulkov, S. Blügel, P. M. Echenique, and P. Hofmann, "Strong spin-orbit splitting on Bi surfaces," *Phys. Rev. Lett.*, vol. 93, p. 046403, 2004.

[21] K. Ishizaka, M. Bahramy, H. Murakawa, M. Sakano, T. Shimojima, T. Sonobe, K. Koizumi, S. Shin, H. Miyahara, A. Kimura, K. Miyamoto, T. Okuda, H. Namatame, M. Taniguchi, R. Arita, N. Nagaosa, K. Kobayashi, Y. Murakami, R. Kumai, Y. Kaneko, Y. Onose, and Y. Tokura, "Giant Rashba-type spin splitting in bulk BiTeI," *Nature Mater.*, vol. 10, pp. 521–526, 2011.

[22] G. Landolt, S. V. Eremeev, Y. M. Koroteev, B. Slomski, S. Muff, T. Neupert, M. Kobayashi, V. N. Strocov, T. Schmitt, Z. S. Aliev, M. B. Babanly, I. R. Amiraslanov, E. V. Chulkov, J. Osterwalder, and J. H. Dil, "Disentanglement of surface and bulk rashba spin splittings in noncentrosymmetric BiTeI," *Phys. Rev. Lett.*, vol. 109, p. 116403, 2012.

[23] M. S. Bahramy, R. Arita, and N. Nagaosa, "Origin of giant bulk rashba splitting: Application to bitei," *Phys. Rev. B*, vol. 84, p. 041202, 2011.

[24] C. L. Kane and E. J. Mele, "Z_2 Topological Order and the Quantum Spin Hall Effect," *Phys. Rev. Lett.*, vol. 95, p. 146802, 2005.

[25] B. A. Bernevig and S.-C. Zhang, "Quantum spin Hall effect," *Phys. Rev. Lett.*, vol. 96, p. 106802, 2006.

[26] L. Fu, C. L. Kane, and E. J. Mele, "Topological insulators in three dimensions," *Phys. Rev. Lett.*, vol. 98, p. 106803, 2007.

[27] J. E. Moore and L. Balents, "Topological invariants of time-reversal-invariant band structures," *Phys. Rev. B*, vol. 75, p. 121306, 2007.

[28] X.-L. Qi, T. L. Hughes, and S.-C. Zhang, "Topological field theory of time-reversal invariant insulators," *Phys. Rev. B*, vol. 78, p. 195424, 2008.

[29] X.-L. Qi, R. Li, J. Zang, and S.-C. Zhang, "Inducing a magnetic monopole with topological surface states," *Science*, vol. 323, no. 5918, pp. 1184–1187, 2009.

[30] I. Garate and M. Franz, "Inverse spin-galvanic effect in the interface between a topological insulator and a ferromagnet," *Phys. Rev. Lett.*, vol. 104, p. 146802, 2010.

[31] L. Fu and C. L. Kane, "Superconducting proximity effect and majorana fermions at the surface of a topological insulator," *Phys. Rev. Lett.*, vol. 100, p. 096407, 2008.

[32] L. Fu and C. L. Kane, "Topological insulators with inversion symmetry," *Phys. Rev. B*, vol. 76, p. 045302, Jul 2007.

[33] H. Zhang, C.-X. Liu, X.-L. Qi, X. Dai, Z. Fang, and S.-C. Zhang, "Topological insulators in Bi_2Se_3, Bi_2Te_3 and Sb_2Te_3 with a single Dirac cone on the surface," *Nature Phys.*, vol. 5, pp. 438–442, 2009.

[34] Y. Xia, D. Qian, D. Hsieh, L. Wray, A. Pal, H. Lin, A. Bansil, D. Grauer, Y. S. Hor, R. J. Cava, and M. Z. Hasan, "Observation of a large-gap topological-insulator class with a single Dirac cone on the surface," *Nature Phys.*, vol. 5, pp. 398–402, 2009.

[35] Y. L. Chen, J.-H. Chu, J. G. Analytis, Z. K. Liu, K. Igarashi, H.-H. Kuo, X. L. Qi, S. K. Mo, R. G. Moore, D. H. Lu, M. Hashimoto, T. Sasagawa, S. C. Zhang, I. R. Fisher, Z. Hussain, and Z. X. Shen, "Massive Dirac fermion on the surface of a magnetically doped topological insulator," *Science*, vol. 329, pp. 659–662, 2010.

[36] A. Damascelli, Z. Hussain, and Z. X. Shen, "Angle-resolved photoemission studies of the cuprate superconductors," *Rev. Mod. Phys.*, vol. 75, p. 473, 2003.

[37] A. Damascelli, "Probing the electronic structure of complex systems by ARPES," *Physica Scripta. Vol*, vol. T109, p. 61, 2004.

[38] S. Hüfner, *Photoelectron Spectroscopy*, vol. 82 of *Solid-State Sciences*. Berlin: Springer-Verlag, 1995.

[39] V. N. Strocov, H. I. Starnberg, P. O. Nilsson, H. E. Brauer, , and L. J. Holleboom, "New method for absolute band structure determination by combining photoemission with very-low energy electron diffractions: application to layered VSe_2," *Phys. Rev. Lett.*, vol. 79, p. 467, 1997.

[40] V. N. Strocov, R. Claessen, G. Nicolay, S. Hüfner, A. Kimura, A. Harasawa, S. Shin, A. Kakizaki, P. O. Nilsson, H. I. Starnberg, and P. Blaha, "Absolute band mapping by combined angle-dependent very-low-energy electron diffraction and photoemission: application to Cu," *Phys. Rev. Lett.*, vol. 81, p. 4943, 1998.

[41] J. Mottershead, *Angle-resolved photoemission spectroscopy studies of $Tl_2Ba_2CuO_{6+\delta}$ and $YBa_2Cu_3O_{7-\delta}$: analysis of recent results and the construction of a new system.* PhD thesis, University of British Columbia, January 2012.

[42] C. Veenstra, *Spin- and angle-resolved photoemission spectroscopy on unconventional superconductor strontium ruthenate.* PhD thesis, University of British Columbia, April 2013.

[43] R. Martin in *Electronic structure: basic theory and practical methods*, New York: Cambridge Univ. Press, 2004.

[44] P. Blaha, K. Schwarz, G. Madsen, D. Kvasnicka, and J. Luitz in *An augmented plane wave plus local orbitals program for calculating crystal roperties*, Vienna: Technical University of Wien, 2001.

[45] K. Schwarz and P. Blaha, "Solid state calculations using wien2k," *Computational Materials Science*, vol. 28, no. 2, pp. 259 – 273, 2003.

[46] G. Kresse and J. Furthmüller, "Efficient iterative schemes for *ab initio* total-energy calculations using a plane-wave basis set," *Phys. Rev. B*, vol. 54, pp. 11169–11186, 1996.

[47] G. Kresse and J. Hafner, "*Ab initio* molecular-dynamics simulation of the liquid-metal amorphous-semiconductor transition in germanium," *Phys. Rev. B*, vol. 49, pp. 14251–14269, May 1994.

[48] G. Kresse and J. Furthmüller, "Efficiency of ab-initio total energy calculations for metals and semiconductors using a plane-wave basis set," *Computational Materials Science*, vol. 6, no. 1, pp. 15 – 50, 1996.

[49] G. Kresse and J. Hafner, "*Ab initio* molecular dynamics for liquid metals," *Phys. Rev. B*, vol. 47, pp. 558–561, Jan 1993.

[50] O. K. Andersen, "Linear methods in band theory," *Phys. Rev. B*, vol. 12, p. 3060, 1975.

[51] D. Snchez-Portal, P. Ordejn, E. Artacho, and J. M. Soler, "Density-functional method for very large systems with LCAO basis sets," *Int. J. Quantum Chem.*, vol. 65, p. 453461, 1997.

[52] X. Gonze, J.-M. Beuken, R. Caracas, F. Detraux, M. Fuchs, G.-M. Rignanese, L. Sindic, M. Verstraete, and G., "First-principles computation of material properties: the abinit software project," *Computational Materials Science*, vol. 25, no. 3, pp. 478 – 492, 2002.

[53] P. Giannozzi, S. Baroni, N. Bonini, M. Calandra, R. Car, C. Cavazzoni, D. Ceresoli, G. L. Chiarotti, M. Cococcioni, I. Dabo, A. D. Corso, S. de Gironcoli, S. Fabris, G. Fratesi, R. Gebauer, U. Gerstmann, C. Gougoussis, A. Kokalj, M. Lazzeri, L. Martin-Samos, N. Marzari, F. Mauri, R. Mazzarello, S. Paolini, A. Pasquarello, L. Paulatto, C. Sbraccia, S. Scandolo, G. Sclauzero, A. P. Seitsonen, A. Smogunov, P. Umari, and R. M. Wentzcovitch, "QUANTUM ESPRESSO: a modular and open-source software project for quantum simulations of materials," *Journal of Physics: Condensed Matter*, vol. 21, no. 39, p. 395502, 2009.

[54] R. Dovesi, V. R. Saunders, C. Roetti, R. Orlando, C. M. Zicovich-Wilson, F. Pascale, B. Civalleri, K. Doll, N. M. Harrison, I. J. Bush, P. DArco, and M. Llunell in *CRYSTAL09 User's Manual*, Torino: University of Torino, 2009.

[55] G. Kotliar, S. Y. Savrasov, K. Haule, V. S. Oudovenko, O. Parcollet, and C. A. Marianetti, "Electronic structure calculations with dynamical mean-field theory," *Rev. Mod. Phys.*, vol. 78, pp. 865–951, Aug 2006.

[56] W. M. C. Foulkes, L. Mitas, R. J. Needs, and G. Rajagopal, "Quantum monte carlo simulations of solids," *Rev. Mod. Phys.*, vol. 73, pp. 33–83, Jan 2001.

[57] O. K. Andersen and T. Saha-Dasgupta, "Muffin-tin orbitals of arbitrary order," *Phys. Rev. B*, vol. 62, p. 16219, 2000.

[58] N. Marzari, A. A. Mostofi, J. R. Yates, I. Souza, and D. Vanderbilt, "Maximally localized wannier functions: Theory and applications," *Rev. Mod. Phys.*, vol. 84, pp. 1419–1475, 2012.

[59] K. Wittel and R. Manne, "Atomic spin-orbit interaction parameters from spectral data for 19 elements," *Theor. Chim. Acta.*, vol. 33, pp. 347–349, 1974.

[60] H.-J. Zhang, S. Chadov, L. Müchler, B. Yan, X.-L. Qi, J. Kübler, S.-C. Zhang, and C. Felser, "Topological insulators in ternary compounds with a honeycomb lattice," *Phys. Rev. Lett.*, vol. 106, p. 156402, 2011.

[61] Y.-S. Lee, M. B. Nardelli, and N. Marzari, "Band structure and quantum conductance of nanostructures from maximally localized wannier functions: The case of functionalized carbon nanotubes," *Phys. Rev. Lett.*, vol. 95, p. 076804, 2005.

[62] M. P. L. Sancho, J. M. L. Sancho, and J. Rubio, "Quick iterative scheme for the calculation of transfer matrices: application to Mo (100)," *J. Phys. F: Met. Phys.*, vol. 14, p. 1205, 1984.

[63] M. P. L. Sancho, J. M. L. Sancho, and J. Rubio, "Highly convergent schemes for the calculation of bulk and surface Green functions," *J. Phys. F: Met. Phys.*, vol. 15, p. 851, 1985.

[64] C.-X. Liu, X.-L. Qi, H. Zhang, X. Dai, Z. Fang, and S.-C. Zhang, "Model hamiltonian for topological insulators," *Phys. Rev. B*, vol. 82, p. 045122, 2010.

[65] J. E. Moore, "The birth of topological insulators," *Nature*, vol. 464, pp. 194–198, 2010.

[66] B. A. Bernevig, T. L. Hughes, and S.-C. Zhang, "Quantum spin Hall effect and topological phase transition in HgTe quantum wells," *Science*, vol. 314, pp. 1757–1761, 2006.

[67] P. Roushan, J. Seo, C. V. Parker, Y. S. Hor, D. Hsieh, D. Qian, A. Richardella, M. Z. Hasan, R. J. Cava, and A. Yazdani, "Topological surface states protected from backscattering by chiral spin texture," *Nature*, vol. 460, pp. 1106–1109, 2009.

[68] P. Cheng, C. Song, T. Zhang, Y. Zhang, Y. Wang, J.-F. Jia, J. Wang, Y. Wang, B.-F. Zhu, X. Chen, X. Ma, K. He, L. Wang, X. Dai, Z. Fang, X. Xie, X.-L. Qi, C.-X. Liu, S.-C. Zhang, and Q.-K. Xue, "Landau

quantization of topological surface states in Bi_2Se_3," *Phys. Rev. Lett.*, vol. 105, p. 076801, 2010.

[69] N. P. Butch, K. Kirshenbaum, P. Syers, A. B. Sushkov, G. S. Jenkins, H. D. Drew, and J. Paglione, "Strong surface scattering in ultrahigh-mobility Bi_2Se_3 topological insulator crystals," *Phys. Rev. B*, vol. 81, p. 241301, 2010.

[70] T. Hirahara, Y. Sakamoto, Y. Takeichi, H. Miyazaki, S. ichi Kimura, I. Matsuda, A. Kakizaki, and S. Hasegawa, "Anomalous transport in an n-type topological insulator ultrathin Bi_2Se_3 film," *Phys. Rev. B*, vol. 82, p. 155309, 2010.

[71] S. R. Park, W. S. Jung, C. Kim, D. J. Song, C. Kim, S. Kimura, K. D. Lee, and N. Hur, "Quasiparticle scattering and the protected nature of the topological states in a parent topological insulator Bi_2Se_3," *Phys. Rev. B*, vol. 81, p. 041405, 2010.

[72] D. Hsieh, Y. Xia, D. Qian, L. Wray, F. Meier, J. H. Dil, J. Osterwalder, L. Patthey, A. V. Fedorov, H. Lin, A. Bansil, D. Grauer, Y. S. Hor, R. J. Cava, and M. Z. Hasan, "Observation of time-reversal-protected single-Dirac-cone topological-insulator states in Bi_2Te_3 and Sb_2Te_3," *Phys. Rev. Lett.*, vol. 103, p. 146401, 2009.

[73] D. Hsieh, Y. Xia, D. Qian, L. Wray, J. H. Dil, F. Meier, J. Osterwalder, L. Patthey, J. G. Checkelsky, N. P. Ong, A. V. Fedorov, H. Lin, A. Bansil, D. Grauer, Y. S. Hor, R. J. Cava, and M. Z. Hasan, "A tunable topological insulator in the spin helical Dirac transport regime," *Nature*, vol. 460, pp. 1101–1106, 2009.

[74] S.-Y. Xu, L. Wray, Y. Xia, F. von Rohr, Y. Hor, J. Dil, F. Meier, B. Slomski, J. Osterwalder, M. Neupane, H. Lin, A. Bansil, A. Fedorov, R. J. Cava, and M. Z. Hasan, "Realization of an isolated dirac node and strongly modulated spin texture in the topological insulator Bi_2Te_3," *arXiv e-prints, 1101.3985*, 2011.

[75] D. Kong, J. C. Randel, H. Peng, J. J. Cha, S. Meister, K. Lai, Y. Chen, Z.-X. Shen, H. C. Manoharan, and Y. Cui, "Topological insulator nanowires and nanoribbons," *Nano Lett.*, vol. 10, pp. 329–333, 2010.

[76] L. Fu and C. L. Kane, "Superconducting proximity effect and majorana fermions at the surface of a topological insulator," *Phys. Rev. Lett.*, vol. 100, p. 096407, 2008.

[77] M. A. Hossain, J. D. F. Mottershead, D. Fournier, A. Bostwick, J. L. Mcchesney, E. Rotenberg, R. Liang, W. N. Hardy, G. A. Sawatzky, I. S. Elfimov, D. A. Bonn, and A. Damascelli, "*In situ* doping control of the surface of high-temperature superconductors," *Nature Phys.*, vol. 4, pp. 527–531, 2008.

[78] D. Fournier, G. Levy, Y. Pennec, J. L. Mcchesney, A. Bostwick, E. Rotenberg, R. Liang, W. N. Hardy, D. A. Bonn, I. S. Elfimov, and A. Damascelli, "Loss of nodal quasiparticle integrity in underdoped $YBa_2Cu_3O_{6+x}$," *Nature Phys.*, vol. 6, pp. 905–911, 2010.

[79] J. P. Perdew, K. Burke, and M. Ernzerhof, "Generalized gradient approximation made simple," *Phys. Rev. Lett.*, vol. 77, p. 3865, 1996.

[80] M. Bianchi, D. Guan, S. Bao, J. Mi, B. Iversen, P. King, and P. Hofmann, "Coexistence of the topological state and a two-dimensional electron gas on the surface of Bi_2Se_3," *Nature Commun.*, vol. 1, p. 128, 2010.

[81] K. Kuroda, M. Arita, K. Miyamoto, M. Ye, J. Jiang, A. Kimura, E. E. Krasovskii, E. V. Chulkov, H. Iwasawa, T. Okuda, K. Shimada, Y. Ueda, H. Namatame, and M. Taniguchi, "Hexagonally deformed fermi surface of the 3d topological insulator Bi_2Se_3," *Phys. Rev. Lett.*, vol. 105, p. 076802, 2010.

[82] M. Nagano, A. Kodama, T. Shishidou, and T. Oguchi, "A first-principles study on the rashba effect in surface systems," *J. Phys.: Condens. Matter*, vol. 21, p. 064239, 2009.

[83] M. König, S. Wiedmann, C. Brone, A. Roth, H. Buhmann, L. W. Molenkamp, X.-L. Qi, and S.-C. Zhang, "Quantum spin hall insulator state in HgTe quantum wells," *Science*, vol. 318, pp. 766–770, 2007.

[84] L. A. Wray, S.-Y. Xu, Y. Xia, D. Hsieh, A. V. Fedorov, Y. S. Hor, R. J. Cava, A. Bansil, H. Lin, and M. Z. Hasan, "A topological insulator surface under strong coulomb, magnetic and disorder perturbations," *Nature Phys.*, vol. 7, pp. 32–37, 2010.

[85] T. Valla, Z.-H. Pan, D. Gardner, Y. S. Lee, and S. Chu, "Photoemission spectroscopy of magnetic and nonmagnetic impurities on the surface of the Bi_2Se_3 topological insulator," *Phys. Rev. Lett.*, vol. 108, p. 117601, 2012.

[86] M. R. Scholz, J. Sánchez-Barriga, D. Marchenko, A. Varykhalov, A. Volykhov, L. V. Yashina, and O. Rader, "Tolerance of topological surface states towards magnetic moments: Fe on Bi_2Se_3," *Phys. Rev. Lett.*, vol. 108, p. 256810, Jun 2012.

[87] T. Schlenk, M. Bianchi, M. Koleini, A. Eich, O. Pietzsch, T. O. Wehling, T. Frauenheim, A. Balatsky, J.-L. Mi, B. B. Iversen, J. Wiebe, A. A. Khajetoorians, P. Hofmann, and R. Wiesendanger, "Controllable magnetic doping of the surface state of a topological insulator," *Phys. Rev. Lett.*, vol. 110, p. 126804, Mar 2013.

[88] S.-Y. Xu, Y. Xia, L. A. Wray, S. Jia, F. Meier, J. H. Dil, J. Osterwalder, B. Slomski, A. Bansil, H. Lin, R. J. Cava, and M. Z. Hasan, "Topological phase transition and texture inversion in a tunable topological insulator," *Science*, vol. 332, pp. 560–564, 2011.

[89] T. Sato, K. Segawa, K. Kosaka, S. Souma, K. Nakayama, K. Eto, T. Minami, Y. Ando, and T. Takahashi, "Unexpected mass acquisition of Dirac fermions at the quantum phase transition of a topological insulator," *Nature Phys.*, vol. 7, pp. 840–844, 2011.

[90] Y. S. Hor, P. Roushan, H. Beidenkopf, J. Seo, D. Qu, J. G. Checkelsky, L. A. Wray, D. Hsieh, Y. Xia, S.-Y. Xu, D. Qian, M. Z. Hasan, N. P.

Ong, A. Yazdani, and R. J. Cava, "Development of ferromagnetism in the doped topological insulator $Bi_{2-x}Mn_xTe_3$," *Phys. Rev. B*, vol. 81, p. 195203, 2010.

[91] I. Vobornik, U. Manju, J. Fujii, F. Borgatti, P. Torelli, D. Krizmancic, Y. S. Hor, R. J. Cava, and G. Panaccione, "Magnetic proximity effect as a pathway to spintronic applications of topological insulators," *Nano Letters*, vol. 11, pp. 4079–4082, 2011.

[92] J. Henk, M. Flieger, I. V. Maznichenko, I. Mertig, A. Ernst, S. V. Eremeev, and E. V. Chulkov, "Topological character and magnetism of the dirac state in mn-doped Bi_2Te_3," *Phys. Rev. Lett.*, vol. 109, p. 076801, 2012.

[93] L. Fu, "Hexagonal warping effects in the surface states of the topological insulator Bi_2Te_3," *Phys. Rev. Lett.*, vol. 103, p. 266801, 2009.

[94] B. Fluegel, S. Francoeur, A. Mascarenhas, S. Tixier, E. C. Young, and T. Tiedje, "Giant spin-orbit bowing in $GaAs_{1-x}Bi_x$," *Phys. Rev. Lett.*, vol. 97, p. 067205, 2006.

[95] M. Liu, J. Zhang, C.-Z. Chang, Z. Zhang, X. Feng, K. Li, K. He, L.-l. Wang, X. Chen, X. Dai, Z. Fang, Q.-K. Xue, X. Ma, and Y. Wang, "Crossover between weak antilocalization and weak localization in a magnetically doped topological insulator," *Phys. Rev. Lett.*, vol. 108, p. 036805, 2012.

[96] S.-Y. Xu, M. Neupane, C. Liu, D. Zhang, A. Richardella, L. A. Wray, N. Alidoust, M. Leandersson, T. Balasubramanian, J. Sánchez-Barriga, O. Rader, G. Landolt, B. Slomski, J. H. Dil, J. Osterwalder, T.-R. Chang, H.-T. Jeng, H. Lin, A. Bansil, N. Samarth, and M. Z. Hasan, "Hedgehog spin texture and berry's phase tuning in a magnetic topological insulator," *Nature Phys.*, vol. 8, pp. 616–622, 2012.

[97] M. A. Hossain, B. Bohnenbuck, Y. D. Chuang, M. W. Haverkort, I. S. Elfimov, A. Tanaka, A. G. Cruz Gonzalez, Z. Hu, H.-J. Lin, C. T.

Chen, R. Mathieu, Y. Tokura, Y. Yoshida, L. H. Tjeng, Z. Hussain, B. Keimer, G. A. Sawatzky, and A. Damascelli, "Mott versus Slater-type metal-insulator transition in Mn-substituted $Sr_3Ru_2O_7$," *Phys. Rev. B*, vol. 86, p. 041102, 2012.

[98] Y. L. Chen, J. G. Analytis, J. H. Chu, Z. K. Liu, S. K. Mo, X. L. Qi, H. J. Zhang, D. H. Lu, X. Dai, Z. Fang, S. C. Zhang, I. R. Fisher, Z. Hussain, and Z. X. Shen, "Experimental realization of a three-dimensional topological insulator Bi_2Te_3," *Science*, vol. 325, no. 5937, pp. 178–181, 2009.

[99] M. Brahlek, N. Bansal, N. Koirala, S.-Y. Xu, M. Neupane, C. Liu, M. Z. Hasan, and S. Oh, "Topological-metal to band-insulator transition in $(Bi_{1-x}In_x)_2Se_3$ thin films," *Phys. Rev. Lett.*, vol. 109, p. 186403, 2012.

[100] S. Souma, K. Kosaka, T. Sato, M. Komatsu, A. Takayama, T. Takahashi, M. Kriener, K. Segawa, and Y. Ando, "Direct measurement of the out-of-plane spin texture in the Dirac-cone surface state of a topological insulator," *Phys. Rev. Lett.*, vol. 106, p. 216803, 2011.

[101] Z.-H. Pan, E. Vescovo, A. V. Fedorov, D. Gardner, Y. S. Lee, S. Chu, G. D. Gu, and T. Valla, "Electronic structure of the topological insulator Bi_2Se_3 using angle-resolved photoemission spectroscopy: evidence for a nearly full surface spin polarization," *Phys. Rev. Lett.*, vol. 106, p. 257004, 2011.

[102] C. Jozwiak, Y. L. Chen, A. V. Fedorov, J. G. Analytis, C. R. Rotundu, A. K. Schmid, J. D. Denlinger, Y.-D. Chuang, D.-H. Lee, I. R. Fisher, R. J. Birgeneau, Z.-X. Shen, Z. Hussain, and A. Lanzara, "Widespread spin polarization effects in photoemission from topological insulators," *Phys. Rev. B*, vol. 84, p. 165113, 2011.

[103] O. V. Yazyev, J. E. Moore, and S. G. Louie, "Spin polarization and transport of surface states in the topological insulators Bi_2Se_3 and

Bi_2Te_3 from first principles," *Phys. Rev. Lett.*, vol. 105, p. 266806, 2010.

[104] Y. Zhao, Y. Hu, L. Liu, Y. Zhu, and H. Guo, "Helical States of Topological Insulator Bi_2Se_3," *Nano Letters*, vol. 11, pp. 2088–2091, 2011.

[105] C.-H. Park and S. G. Louie, "Spin polarization of photoelectrons from topological insulators," *Phys. Rev. Lett.*, vol. 109, p. 097601, 2012.

[106] Y. Cao, J. A. Waugh, X.-W. Zhang, J.-W. Luo, Q. Wang, T. J. Reber, S. K. Mo, Z. Xu, A. Yang, J. Schneeloch, G. Gu, M. Brahlek, N. Bansal, S. Oh, A. Zunger, and D. S. Dessau, "In-plane orbital texture switch at the Dirac point in the topological insulator Bi_2Se_3," *arXiv e-prints, 1209.1016*, 2012.

[107] M. Lindroos, S. Sahrakorpi, and A. Bansil, "Matrix element effects in angle-resolved photoemission from $Bi_2Sr_2CaCu_2O_8$: Energy and polarization dependencies, final state spectrum, spectral signatures of specific transitions, and related issues," *Phys. Rev. B*, vol. 65, p. 054514, 2002.

[108] J. G. Checkelsky, Y. S. Hor, M.-H. Liu, D.-X. Qu, R. J. Cava, and N. P. Ong, "Quantum interference in macroscopic crystals of nonmetallic Bi_2Se_3," *Phys. Rev. Lett.*, vol. 103, p. 246601, 2009.

[109] P. Roushan, J. Seo, C. V. Parker, Y. S. Hor, D. Hsieh, D. Qian, A. Richardella, M. Z. Hasan, R. J. Cava, and A. Yazdani, "Topological surface states protected from backscattering by chiral spin texture," *Nature*, vol. 460, pp. 1106–1110, 2009.

[110] Z. Alpichshev, J. G. Analytis, J.-H. Chu, I. R. Fisher, Y. L. Chen, Z. X. Shen, A. Fang, and A. Kapitulnik, "STM imaging of electronic waves on the surface of Bi_2Te_3: Topologically protected surface states and hexagonal warping effects," *Phys. Rev. Lett.*, vol. 104, p. 016401, Jan 2010.

[111] Y. H. Wang, D. Hsieh, D. Pilon, L. Fu, D. R. Gardner, Y. S. Lee, and N. Gedik, "Observation of a warped helical spin texture in Bi_2Se_3 from circular dichroism angle-resolved photoemission spectroscopy," *Phys. Rev. Lett.*, vol. 107, p. 207602, 2011.

[112] S. R. Park, J. Han, C. Kim, Y. Y. Koh, C. Kim, H. Lee, H. J. Choi, J. H. Han, K. D. Lee, N. J. Hur, M. Arita, K. Shimada, H. Namatame, and M. Taniguchi, "Chiral orbital-angular momentum in the surface states of Bi_2Se_3," *Phys. Rev. Lett.*, vol. 108, p. 046805, 2012.

[113] J. W. Mciver, D. Hsieh, H. Steinberg, P. Jarillo-Herrero, and N. Gedik, "Control over topological insulator photocurrents with light polarization," *Nature Nanotech.*, vol. 7, p. 96, 2011.

[114] J. J. Yeh and I. Lindau, "Atomic subshell photoionization cross sections and asymmetry parameters: $1 \leq Z \leq 103$," *Atomic Data and Nuclear Data Tables*, vol. 32, pp. 1–155, 1985.

[115] H. Zhang, C.-X. Liu, and S.-C. Zhang, "Spin-orbital texture in topological insulators," *arXiv e-prints, 1211.0762*, 2012.

[116] M. Mulazzi, G. Rossi, J. Braun, J. Minár, H. Ebert, G. Panaccione, I. Vobornik, and J. Fujii, "Understanding intensities of angle-resolved photoemission with circularly polarized radiation from a Cu(111) surface state," *Phys. Rev. B*, vol. 79, p. 165421, 2009.

[117] Y. Liu, G. Bian, T. Miller, and T.-C. Chiang, "Visualizing electronic chirality and berry phases in graphene systems using photoemission with circularly polarized light," *Phys. Rev. Lett.*, vol. 107, p. 166803, 2011.

[118] M. Mucha-Kruczyński, O. Tsyplyatyev, A. Grishin, E. McCann, V. I. Fal'ko, A. Bostwick, and E. Rotenberg, "Characterization of graphene through anisotropy of constant-energy maps in angle-resolved photoemission," *Phys. Rev. B*, vol. 77, p. 195403, 2008.

[119] A. Grüneis, C. Attaccalite, A. Rubio, D. V. Vyalikh, S. L. Molodtsov, J. Fink, R. Follath, W. Eberhardt, B. Büchner, and T. Pichler, "Angle-resolved photoemission study of the graphite intercalation compound KC_8: A key to graphene," *Phys. Rev. B*, vol. 80, p. 075431, 2009.

[120] I. Gierz, J. Henk, H. Höchst, C. R. Ast, and K. Kern, "Illuminating the dark corridor in graphene: Polarization dependence of angle-resolved photoemission spectroscopy on graphene," *Phys. Rev. B*, vol. 83, p. 121408, 2011.

[121] C. Hwang, C.-H. Park, D. A. Siegel, A. V. Fedorov, S. G. Louie, and A. Lanzara, "Direct measurement of quantum phases in graphene via photoemission spectroscopy," *Phys. Rev. B*, vol. 84, p. 125422, 2011.

[122] D. Pesin and A. H. Macdonald, "Spintronics and pseudospintronics in graphene and topological insulators," *Nature Mater.*, vol. 11, pp. 409–416, 2012.

[123] P. Hosur, "Circular photogalvanic effect on topological insulator surfaces: Berry-curvature-dependent response," *Phys. Rev. B*, vol. 83, p. 035309, Jan 2011.

[124] A. Junck, G. Refael, and F. von Oppen, "Photocurrent response of topological insulator surface states," *arXiv e-prints, 1301.4392*, 2013.

[125] C. Jozwiak, C.-H. Park, K. Gotlieb, C. Hwang, D.-H. Lee, S. G. Louie, J. D. Denlinger, C. R. Rotundu, R. J. Birgeneau, Z. Hussain, and A. Lanzara, "Photoelectron spin-flipping and texture manipulation in a topological insulator," *Nature Phys.*, vol. 9, pp. 293–298, 2013.

[126] Y. Cao, J. A. Waugh, N. C. Plumb, T. J. Reber, S. Parham, G. Landolt, Z. Xu, A. Yang, J. Schneeloch, G. Gu, J. H. Dil, and D. S. Dessau, "Coupled spin-orbital texture in a prototypical topological insulator," *arXiv e-prints, 1211.5998*, 2012.

[127] Z. Xie, S. He, C. Chen, Y. Feng, H. Yi, A. Liang, L. Zhao, D. Mou, J. He, Y. Peng, X. Liu, Y. Liu, G. Liu, X. Dong, J. Zhang, X. Wang,

Q. Peng, Z. Wang, S. Zhang, F. Yang, C. Chen, Z. Xu, and X. J. Zhou, "Orbital-selective spin texture and its manipulation in a topological insulator," *arXiv e-prints, 1303.0698*, 2013.

[128] T. Okuda, K. Miyamaoto, H. Miyahara, K. Kuroda, A. Kimura, H. Namatame, and M. Taniguchi, "Efficient spin resolved spectroscopy observation machine at hiroshima synchrotron radiation center," *Review of Scientific Instruments*, vol. 82, no. 10, p. 103302, 2011.

[129] K. Miyamoto, A. Kimura, T. Okuda, H. Miyahara, K. Kuroda, H. Namatame, M. Taniguchi, S. V. Eremeev, T. V. Menshchikova, E. V. Chulkov, K. A. Kokh, and O. E. Tereshchenko, "Topological surface states with persistent high spin polarization across the Dirac point in Bi_2Te_2Se and Bi_2Se_2Te," *Phys. Rev. Lett.*, vol. 109, p. 166802, 2012.

[130] A. Damascelli, "Probing the electronic structure of complex systems by ARPES," *Physica Scripta*, vol. T109, pp. 61–74, 2004.

Appendix

List of publications

1. **Z.-H. Zhu**, C.N. Veenstra, G. Levy, A. Ubaldini, P. Syers, N.P. Butch, J. Paglione, M.W. Harverkort, I.S. Elfimov and A. Damascelli,"Layer-by-layer entangled spin-orbital texture of the topological surface state in Bi_2Se_3", *Phys. Rev. Lett.* **110**, 216401 (2013).

2. C.N. Veenstra, **Z.-H. Zhu**, B. Ludbrook, M. Capsoni, G. Levy, A. Nicolaou, J. A. Rosen, R. Comin, S. Kittaka, Y. Maeno, I. S. Elfimov, and A. Damascelli, "Determining the surface-to-bulk progression in the normal-state electronic structure of Sr_2RuO_4 by angle-resolved photoemission and density functional theory", *Phys. Rev. Lett.* **110**, 097004 (2013).

3. J.A. Rosen, R. Comin, G. Levy, D. Fournier, **Z.-H. Zhu**, B. Ludbrook, C.N. Veenstra, D.Wong, P. Dosanjh, Y. Yoshida, H. Eisaki, G.R. Blake, F. White, T.T.M. Palstra, R. Sutarto, F. He, A. Frano Pereira, Y. Lu, B. Keimer, G. Sawatzky, L. Petaccia, and A. Damascelli, "Surface-enhanced charge-density-wave instability in underdoped Bi2201", *Nature Communications*. In press.

4. R. Comin, G. Levy, B. Ludbrook, **Z.-H. Zhu**, C.N. Veenstra, J.A. Rosen, Yogesh Singh, P. Gegenwart, D. Stricker, J.N. Hancock, D. van der Marel, I.S. Elfimov, and A. Damascelli, "Na_2IrO_3 as a novel relativistic Mott insulator with a 340meV gap", *Phys. Rev. Lett.* **109**, 266406 (2012).

5. **Z.-H. Zhu**, G. Levy, B. Ludbrook, C.N. Veenstra, J.A. Rosen, R. Comin, D.Wong, P. Dosanjh, A. Ubaldini, P. Syers, N.P. Butch, J.

Paglione, I.S. Elfimov and A. Damascelli, "Rashba spin-splitting control at the surface of the topological insulator Bi_2Se_3", *Phys. Rev. Lett.* **107**, 186405 (2011).

6. G. Panaccione, U. Manju, F. Offi, E. Annese, I. Vobornik, P. Torelli, **Z.H. Zhu**, M.A. Hossain, L. Simonelli, A. Fondacaro, P. Lacovig, A. Guarino, Y. Yoshida, G. A. Sawatzky, and A. Damascelli, "Depth dependence of itinerant character in Mn-substituted $Sr_3Ru_2O_7$", *New J. Phys.* **13**, 053059 (2011).

Papers in preprint

7. **Z.-H. Zhu**, G. Levy, A. Nicolaou, X.-H. Zhang, N.P. Butch, P. Syers, J. Paglione, I.S. Elfimov and A. Damascelli,"Polarity-driven surface metalicity in SmB_6", submitted (2013).

8. **Z.-H. Zhu**, C.N. Veenstra, S. Zhdanovich, M. P. Schneider, T. Okuda, K. Miyamoto, S.-Y. Zhu, H. Namatame, M. Taniguchi, M.W. Harverkort, I.S. Elfimov and A. Damascelli,"Photoelectron spin-polarization-control in the topological insulator Bi_2Se_3", submitted (2013).

9. C.N. Veenstra, **Z.-H. Zhu**, B. Ludbrook, A. Nicolaou, M. Raichle, B. Slomksi, G. Landolt, S. Kittaka, Y. Maeno, J.H. Dil, I.S. Elfimov, M.W. Harverkort and A. Damascelli,"Observation of strong spin-charge entanglement in Sr_2RuO_4", submitted, *arXiv e-prints*, 1303.5444 (2013).